CHALMERS

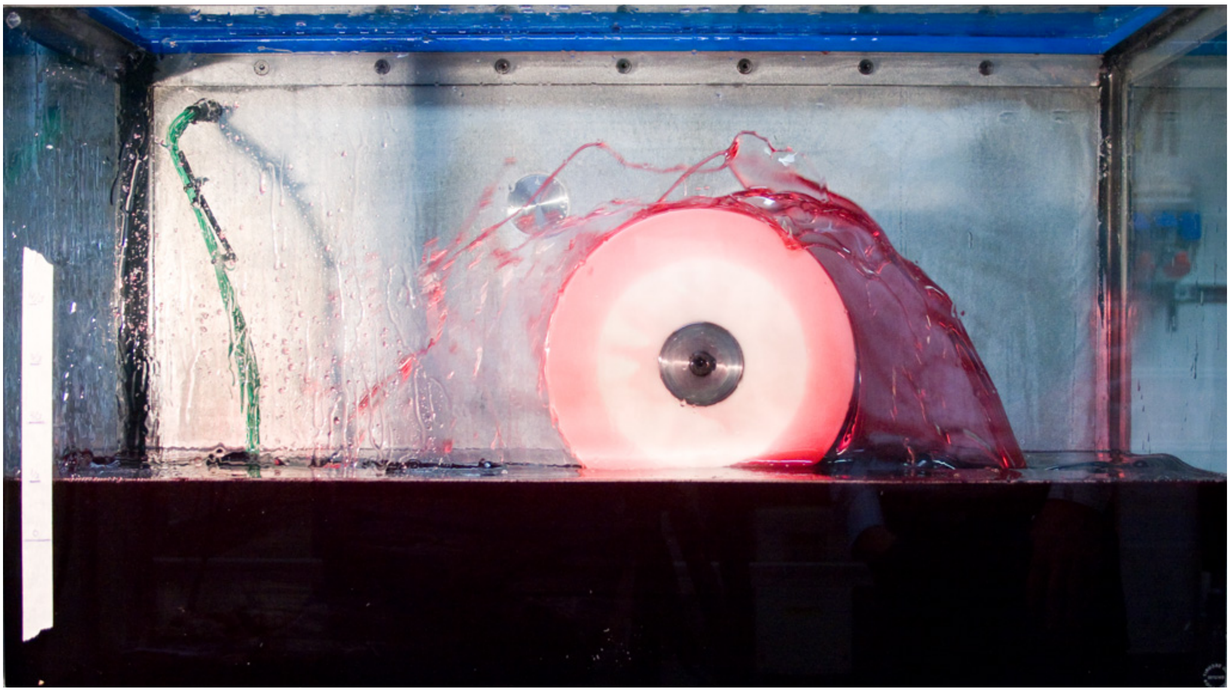

PIV Measurements Around A Rotating Single Gear Partially Submerged In Oil Within Modelled SAAB Gearbox

Master's Thesis in Solid and Fluid Mechanics

EHSAN SISTANI

Department of Applied Mechanics
Division of Dynamics and Division of Fluid Mechanics
CHALMERS UNIVERSITY OF TECHNOLOGY
Göteborg, Sweden 2010

Master's Thesis 2010:49

MASTER'S THESIS 2010:49

PIV Measurements Around A Rotating Single Gear Partially Submerged In Oil Within Modelled SAAB Gearbox

Master's Thesis in Solid and Fluid Mechanics

EHSAN SISTANI

Department of Applied Mechanics
Division of Dynamics and Division of Fluid Mechanics
CHALMERS UNIVERSITY OF TECHNOLOGY

Göteborg, Sweden 2010

PIV Measurements Around A Rotating
Single Gear Partially Submerged In Oil
Within Modelled SAAB Gearbox
EHSAN SISTANI

Master's Thesis 2010:49
ISSN 1652-8557
Department of Applied Mechanics
Division of Dynamics and Division of Fluid Mechanics
Chalmers University of Technology
SE-412 96 Göteborg
Sweden
Telephone: + 46 (0)31-772 1000

Cover:

Chalmers Reproservice
Göteborg, Sweden 2010

PIV Measurements Around A Rotating
Single Gear Partially Submerged In Oil
Within Modelled SAAB Gearbox
Master's Thesis in Solid and Fluid Mechanics
EHSAN SISTANI
Department of Applied Mechanics
Division of Dynamics and Division of Fluid Mechanics
Chalmers University of Technology

Abstract

This study concerns fluid dynamics of the flow around a rotating single gear wheel which is partially submerged in oil within a modelled SAAB gearbox. A literature survey shows a very limited amount of studies on this topic which are publicly available at the moment. The experimental measurements were carried out by means of Particle Image Velocimetry (PIV) on this very highly complex flow. For the purpose of experimental study a test rig representing a simplified model of a gearbox was built. The rig is specially designed for using PIV which means the optical access to the flow is maximized. The flow similarity with respect to a real gearbox is maintained and the working fluid is a transparent mineral oil. The wheel model is made interchangeable and the wheel rotation speed can be varied to investigate different operation conditions. Two different wheel models with a diameter of 220mm were considered in the measurement, one of them is smooth and the other one has spur teeth.

At a very low rotational speed, (50rpm), the flow is mostly in one-phase below the oil level. As the rotational speed increases (400rpm), the flow pattern around the wheel become chaotic and two different two-phase flows with rotation, free-surface effects, and liquid splashing effects are involved. As the wheel rotates and splashing lead to the creation of oil droplets in the top part of the box and air bubbles are generated in the bottom part within the oil. At this stage the optical access become limited by partly from bubbles and oil splashing on the window. These bubbles cause problems due to optical refraction and distortion when laser light is illuminated on them. This issue was partly resolved by performing the experimental measurement in a "transient" mode. The transient mode was applied in such a way that a trigger signal was provided from the wheel to the PIV processor in order to allow immediate measurements suddenly after the rotation was started.

Keywords: Particle Image Velocimetry, Digital Image Velocimetry, Laser Induced Fluorescence, Double-pulsed Velocimetry, Experimental Fluid Dynamics, PIV In Multiphase Flow.

Contents

List of Tables

List of Figures

Preface

In this study the flow field behavior around a rotating wheel have been measured with particle velocimetry technique. The measurement data is then provided to SAAB Automobile fluid mechanic group to be compared with numerical CFD modells. The work has been carried out from September 2009 to April 2010 at the Department of Applied Mechanics, Division of Dynamics and Division of Fluid Mechanics, Chalmers University of Technology, Sweden, with Ehsan Sistani as the student and Sten Sieber as the supervisor at the Department of Fluid Dynamics, SAAB Automobile Powertrain and the Associate Prof. Valery Chernoray at the Department of Applied Mechanics, Division of Dynamics and Division of Fluid Mechanics, Chalmers University of Technology, Sweden.

Aknowledgements

First and foremost, I would like to thank my supervisor, Associate Prof. Valery Chernoray, for his great support and encouragement, for his guidance and stimulating discussion during the work with the project. Without his help this project would not have been possible. I wish to thank my co-supervisor and teacher in fluid mechanics and turbulence, Prof. Lars Davidson for all the help and guidance. I would like to thank Nynas oil for providing and helping us to find the appropriate oil for our study. Special thanks to Sten Sieber for his support and discussion through the work, and all the people at the Department for their help and support. Last but not least, I would like to thank my family and friends for all their support.

Göteborg April 2010
Ehsan Sistani

Nomenclature

Upper-case Roman

C_D	Drag coefficient
F_A	Added mass force
F_D	Drag foce
F_g	Gravity force
F_H	History force
F_p	Pressure force
Re_p	Particle Reynolds number
St_c	Collisions Stokes number

Lower-case Greek

τ	Shear stess
τ_v	Momentum response time
τ_c	Characteristic time of the flow
$\tau_{collision}$	time scale of inter-particle interactions
μ	Dynamic viscosity
α	Volume fraction
e	Normal restitutions coefficient
ζ	Tangential restitutions coefficient
ρ	Density

Abbreviations

IA	Interrogation Area
CC	Cross-Correlation
CFD	Computational Fluid Dynamics
DNS	Direct Numerical Simulation
DPM	Discrete Particle Modeling
FFT	Fast Fourier Transform
ETR	External Trigger Rate
FOV	Field Of View
LES	Large Eddy simulation
LIF	Laser-Induced Fluorescence
Nd:YAG	Neodymium-doped Yttrium Aluminium Garnet
PFBI	Planar Fluorescence for Bubble Imaging
PIV	Particle Image Velocimetry
PTV	Particle Tracking Velocimetry
RMS	Root Mean Square
RPM	Revelations Per Minute
RR	Rotation Rate
ST	Shadow Photography
TR	Trigger Rate

subscripts

f	fluid phase or continuous phase

p	particle
ij	tensor indices
z	upward direction
d	disperse phase

1 Introduction

Particle image velocimetry (PIV) is a non-intrusive technique of instantaneously obtaining a large number of velocity vectors within a plane of a flow. Contrary to the more commonly utilized single-point measurements, PIV allows the spatial structure of the velocity field to be visualized as well as quantified.

In the past decade the technique has matured from only being a novel laboratory tool into being applied in a continuously growing range of applications for example in multiphase flows.

Multiphase flows are present in numerous industrial processes. Knowledge of multiphase flow phenomena eases the control and optimization of the processes. However, it is difficult to obtain knowledge of complex multiphase flows occurring in industrial processes [15]. The flow phenomena cannot be predicted by numerical simulations, and experimental investigations have several physical limitations.

Gear lubrication is a significant concern in a wide range of engineering applications and for industries using power transmission. GM Powertrain Sweden in Trollhättan is developing computational fluid dynamics (CFD) models for predicting the oil flow around rotating components, and the related drag torque.

The main object is to reduce losses in the gearbox and thereby reducing fuel consumption and carbon dioxide (CO_2) emissions. The oil should reduce friction between the gearwheels and also act as a cooling fluid. The problem is that too much oil increases the losses in the gearbox. Increasing the efficiency of the gearboxes has a great market potential not only in the vehicle industry but in any industry where transmission is important such as the pulp industry, the mining industry, wind and hydro power industry, etc. However since GM Powertrain are still under development, reliable measurements for CFD model validation are required.

The flow structure around one single rotating wheel becomes complicated as the wheel rotation increases. In a gearbox with several gears, the flow dynamic would be very complex. However at a very low rotational speed (50rpm), the flow is mostly in one-phase below the oil level. As the rotational speed increases (400rpm), the flow pattern around the wheel will be chaotic and two different two-phase flow with rotation, free-surface effects, and liquid splashing effects will be involved, see figure 1.1. As the wheel rotates, splashing results in the creation of oil droplets in the top part of the box and air bubbles are generated at the bottom part within the oil. At this stage the optical access will be limited by partly from bubbles and oil splashing on window. These bubbles cause problems due to optical reflection and distortion, when laser light is illuminated. This issue was partly resolved by performing the experimental measurement in a "transient" mode.

Today are the behaviors of flow pattern and heat transfer in gearboxes are quite unknown. At the moment, a literature survey shows only a limited amount of studies of this topic which are publicly available, see [20, 17].

Figure 1.1: Flow around wheel at different velocities of rotation: 200, 400, 1200 rpm (from left to right).

1.1 Purpose

The purpose of this project is to provide measurement results by means of velocity fields around rotating gears and cylinders in oil, within an modeled gearbox. The measurements will be used in order to validate multiphase CFD models. The problem statement is outlined in figure 1.2, as the wheel is rotating, air/bubbles and droplets will be created below the oil level as well as above the oil level. The measurements are performed with the use of a one-camera and an non-intrusive optical measurement technique by means of laser-induced fluorescence, Particle Image velocimetry (LIF-PIV). If the conventional PIV technique is applied to multiphase flow, a velocity map may be determined. It is impossible to identify which velocity vector corresponds to which phase of the flow and Advanced PIV technique has to be implemented. In 1991 Sridhar et al. presented an application of PIV to multiphase flow. Thereafter many articles have been published on different multiphase PIV techniques.

The goal of this project is to implement the best possible methods in order to utilize PIV technique for measuring two different two-phase flow, for two different kinds of gearwheel within the modeled gear box. The measurements will occur for

- single smooth wheel,
- single wheel with teeth, (spur, 67 teeth).

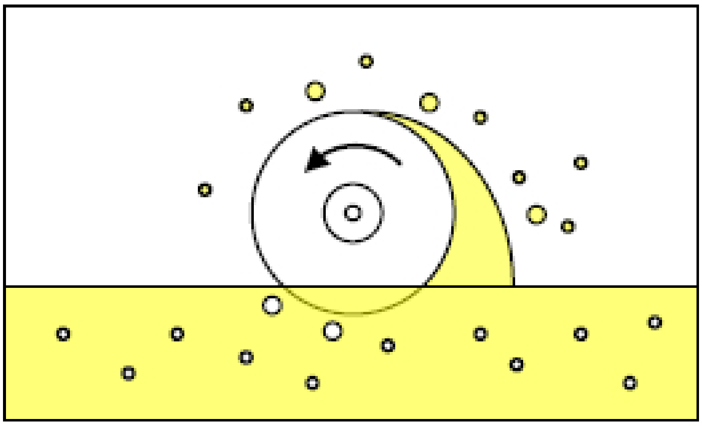

Figure 1.2: Problem formulation.

1.2 Limitations

Two different gearwheels were studied. The measurements occur only as a single wheel, due to the fact that it is too complicated to understand the flow phenomena with several wheels (which exists in a real gearbox) at this very early stage.

This study is an initial step, it is crucial to understand the fundamental flow dynamics around the wheel and between the teeth. The fact that we need to understand how to model the simulation, what kind of fluid model one can use in each wheel and between the teeth and general in CFD.

One of the limitations is the rotational speed we use in our measurement. In fact the facility is build only for maximum rotational speed up to 1200 rpm, which corresponds to 85 km/h, to be compared to a maximum car driving in road of 110 km/h. As we will see due to accumulation and the creation of bubbles, the optical access is quite limited and optical measurement techniques like PIV are not suitable for a rotational speed above 400rpm.

One of the main limitations are, we can't measure the entire flow field and simultaneously provide good spatial resolution due to obvious limitations of the camera. In order to avoid this limitation we perform our measurements for two field of views (FOVs), one is twenty-five times smaller and measured below the interface, $50 \times 50\,mm^2$, and the other one is measured in both interfaces, i.e. air and oil $250 \times 250\,mm^2$, see figure 1.3.

The measurements performed at the center of the wheel, at the symmetry plane. We could run the wheel in two different directional modes, i.e., forward and reverse, one could perform the measurements for both rotation directions and build these two measurements together in order to obtain a full PIV measurement plane around the wheel.

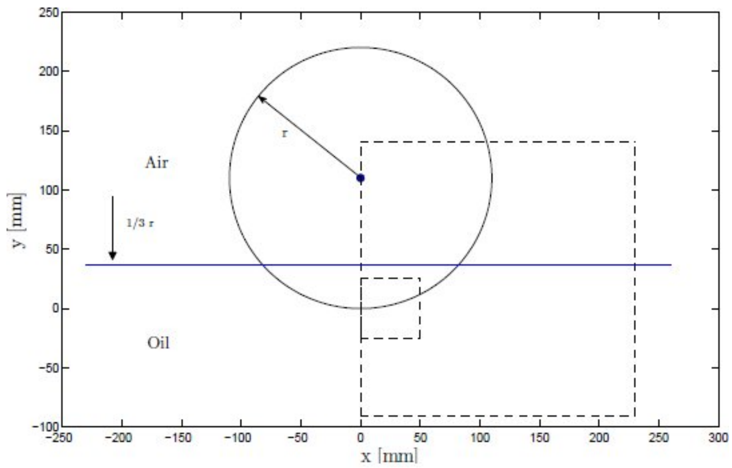

Figure 1.3: Field of view of camera: $50 \times 50\,mm^2$, and $\sim 250 \times 250\,mm^2$.

2 Multiphase flow

As described in the pervious section, the flow around a rotating single gear inside the gearbox is dominated by bubbly flow, oil droplets and three phase flow, specially when the rotational speed is above $200rpm$. Therefore in this section a brief theory behind multiphase flow will be described. The concentration of this theory is pointed to forces that can act on a single particle/bubble or droplet.

Multiphase flow can be subdivided into four categories; gas-liquid, gas-solid, liquid-solid and three phase flows. A important classification of multiphase flow is made in terms of how the different phases are present in the flow, i.e. separated, or dispersed.

In a dispersed flow, one phase is typically present in form of particles or droplets and there are many individual interfaces. In a separated flow, the phases present are relatively separated, with only a few interfaces.

Commonly, dispersed two-phase flows are separated in two types of flow regimes, the dilute regime and the dense regime. In the dilute regime, the spacing (inter-particle spacing) between the particles or droplets are quite large, so their behaviors are governed by the continuous phase (fluid phase) forces. In dense phase systems, the inter-particle spacing are higher, so the inter-particle interaction are typically very important. In section 2.2, we will discuss more about inter-particle spacing.

One way to study the dynamics of a continuous phase and dispersed phase flow is with governing conservation (continuity, momentum and energy) equations that includes the boundary conditions imposed by each and every dispersed particle in the flow. In fact, different averaging procedures are made in order to study their equations.

2.1 Averaging

These commonly used averaging approaches in multiphase flow applied to an instantaneous field $\phi(\vec{x}, t)$ are defined as; time, space, over an ensemble or in some combinations of these. As an example time-averaging, also used in turbulent flow, defines as

$$< \bar{\phi} >= \lim_{T\to\infty} \frac{1}{T} \int_{-T}^{T} \phi(\vec{x}, t)\, dt \qquad \bar{\phi} \;=\; \bar{\phi}(\vec{x})$$

where T is an averaging timescale based on an averaging length scale.

The main assumption is the separation of scales exist and a time scale τ in the filtering is chosen so the instantaneous quantity are averaged over time period which is large compared to turbulent time scales but small compared to the time scale of mean components:

$$\tau_{\text{turbulent fluctuation}} \;<<\; T \;<<\; \tau_{\text{mean flow}}.$$

Also it is possible to describe the flow without time-averaging. By using space averaging, defined by

$$< \phi >_V = \lim_{V\to\infty} \frac{1}{V} \int_V \phi(\vec{x}, t)\, dV \qquad < \phi >_V = < \phi >_V (t)$$

where V is the volume based on an averaging length scale and one can assume that separation of scales must exists and the characteristics dimension of averaging volume are much larger than characteristics dimension of the phases but much smaller than characteristics dimension of physical systems.

We can also take the mean (ensemble) average. This ensemble average is based upon the existence of independent events. The averaging are not limited by volume or time constraints.

The ensemble average of $\phi(\vec{x},t)$ is given by

$$< \phi >_E = \lim_{N\to\infty} \frac{1}{N} \sum_{n=1}^{N} \phi_n(\vec{x},t) \qquad < \phi >_E = < \phi >_E (\vec{x},t)$$

where N is the total number of realizations. Under certain condition i.e. steady flow, the ensemble and time averaging are equivalent. For example in homogenous flow where the statistics are independent of origin the ensemble and volume average are equivalent.

While averaging allows the mathematical solution of the problem to be tractable, there is an apparent need to recover the loss of information regarding the local gradients between the phases, which have to be re-supplied in the form of semiempirical closure relationships, also known as constitutive equations.

2.2 Characterization of multiphase flows

Dependent of the problem characteristics there are a large number of important parameters in multiphase flow (fluid mechanics). For example particle Reynolds number, Re_p, Stokes number for turbulent and collision St, Knudsen Kn, Peclet Pe, Nusselt Nn, Prandtl Pr, Schmidt Sc, Sherwood Sh, etc. And for example in order to describe the bubble shape and the feature of the bubble, the Weber We, Eotvos Eo, Morton M etc are used.

The Knudsen number is the ratio of the mean free path of the molecules to the particle diameter λ/d_p. Where λ is the mean free path length. The Knudsen number Kn can also be related to the particle relative Reynolds number and Mach number as M_r/Re_r. The Knudsen number is important for the compressibility and rarefaction effects. Example free molecule flow occurs when $Kn > 10$. In this regime, the flow is treated as the motion of an individual and in transitional flow where $0.25 < Kn < 10$ occurs. When approaching-rebounding molecular collisions becomes significant to the flow filed. In particular when $10^{-3} < Kn < 0.25$ corresponds to slip flow and finally when $Kn < 10^{-3}$ corresponds to continuum flow.

But one of the most important parameter in multiphase flows is the volume fraction (void fraction), which define how much of the local volume is occupied by the particles in a unit volume. The volume fraction of dispersed phase is defined as

$$\alpha_d = \lim_{\delta V\to\delta V^0} \frac{\delta V_d}{\delta V} \tag{2.1}$$

where δV_d is the volume of the dispersed phase in the volume. The volume fraction of the continuous phase is given by

$$\alpha_f = 1 - \alpha_d. \tag{2.2}$$

Note that the volume fraction in two dimensions are not equivalent to three dimensions. The reason is the diameter of the particles in two-dimensions have not the same size as in three-dimensions of the same volume.

The characteristic size of the dispersed phase is also important and given is by

$$d_p = \sqrt[3]{\frac{6V}{\pi}} \tag{2.3}$$

Which assumes the volume occupied by one particle has a spherical shape.

Also particle spacing (inter-particle spacing) between the particles are important to determine particle-particle interactions. If a particle or droplet can be treated as an isolated element, and assuming they are homogeneously arranged, the equation of inter-particle spacing is given by

$$\frac{L}{d_p} = \sqrt[3]{\frac{\pi}{6\alpha_d}}, \qquad \alpha_d = \frac{d_p^3\pi/6}{L^3} \tag{2.4}$$

where L is the distance between the element (particle or droplet) centers. For a dispersed volume fraction of 10 %, the inter-particle spacing is $\sim$ 1.7, which suggests that the dispersed phase elements are to close to each other in order to be treated as isolated. Hence, mass, momentum and heat transfer for each element are influenced by the neighboring elements.

For example for most gas-particle and gas-droplet flows, the ratio of the material densities are of order of 10^{-3} and the inter-particle spacing L/d_p, for flows with a mass ratio of unity is $\sim$ 10. In this case, individual particles or droplets could be treated as isolated droplets with little influence of the neighboring elements on the drag or heat transfer rate. But in fluidized beds, the mass ratio is large and the particles may be located less than 3 diameter apart so the particle cannot be treated as isolated droplets. For slurry flow, the material density ratio can be in order of unity and the particle is insufficient to treat the particles as isolated elements [10].

The Reynolds number (particle Reynolds number) is also an important dimensionless number, which is the ratio of inertia force divided by viscous force. At low Reynolds number i.e $Re << 1$ (Stokes flow or creeping flow) the inertia is unimportant which means that the flow is dominated by viscous forces and this would lead to large drag forces. But the opposite is i.e., $Re_p >> 1$ and thus the viscous effect is unimportant which reduce the drag force sufficiently. But in special case i.e., $Re_p \sim 1$ the drag coefficient is $24/Re_p$ (Stokes law).

Another important dimensionless number in multiphase flow is the turbulent Stokes number, which will be better discussed in section 3.5. Other important Stokes number is the collision Stokes number:

$$St_c = \frac{\tau_v}{\tau_{\text{collision}}} \tag{2.5}$$

Where τ_v represents the momentum response time, and $\tau_{\text{collision}}$ represents the time scale of inter-particle interactions. If $St_c < 1$ a flow may be considered as dilute, and if $St_c > 1$ a flow may be considered as dense. This is can be used as an additional measurement in order to determine the importance of particle-particle interactions, next to that inter-particle spacing.

2.3 Forces on dispersed particles

Newton's second law can be applied to the dispersed particles. The main controversy has described the forces acting on the particle considering a few small particles in a flow with

$Re << 1$. Uniform flow is described by the pioneering work of Basset (1888), Boussinesq (1885) and Oseen (1927), therefore abbreviated as the BBO-Eq. A more rigorous derivation of BBO-Eq can be founded in Maxey and Riley (1983). Also, the complete form of the equation as derived by Maxey and Riley must be used if flow curvature effects are important.

However, in Lagrangian framework the motion of single particle with a mass of m_p is given by

$$m_p \frac{d\vec{u}_p}{dt} = \sum \vec{F}_p \tag{2.6}$$

The right-hand-side of Eq (2.6), represent the forces acting on the single particle, i.e., drag, gravity, virtual added mass, history or Basset force, force due to pressure and shear stress from the fluid, Magnus and Saffman lift forces, Faxen correction forces, thermophoretic forces, and the last force represents the forces due to fluid turbulent dispersion and Brownian motion, given as:

$$\sum \vec{F}_p = \vec{F}_D + \vec{F}_g + \vec{F}_A + \vec{F}_P + \vec{F}_H + \vec{F}_{\text{Lift}} + \vec{F}_{\text{Faxen}} + \vec{F}_{\text{Therm}} + \vec{F}_{\text{Turb}} \tag{2.7}$$

2.3.1 Drag force

The "steady state" drag is the drag force which acts on the particle or droplet in a uniform pressure field when there is no acceleration of the relative velocity $(\vec{u}_f - \vec{u}_p)$ between the particle and the conveying fluid (continuous phase). If the conveying have a density denoted by ρ_f, then drag force can be determined by

$$\vec{F}_D = \frac{1}{2} C_D A_p \rho_f (\vec{u}_f - \vec{u}_p)|\vec{u}_f - \vec{u}_p| \tag{2.8}$$

where A_p is the projected area normal to the flow i.e., $\pi d_p^2/4$ for a sphere, C_D is the drag coefficient, and $\vec{u}_f$ and $\vec{u}_p$ are the velocities of the continuous phase and the droplet or particle, respectively.

The drag force $\vec{F}_D$ is based on an empirical formula. In the stokes regime ($Re < 1$), the flow is regarded as a creeping flow. In that regime, the drag force (viscous drag force) can be described by Stokes law:

$$\vec{F}_D = 3\pi\mu_f d_p (\vec{u}_f - \vec{u}_p) \tag{2.9}$$

by combining this forces and Eq (2.8) the drag coefficient results in

$$C_D = \frac{24}{Re_p} \tag{2.10}$$

where Re_p is the Reynolds number based on relative velocity

$$Re_p = \frac{\rho_f |\vec{u}_f - \vec{u}_p| d_p}{\mu_f}. \tag{2.11}$$

Figure 2.1 illustrate the variation of the drag coefficient with Reynolds number for a non-rotating sphere. In general C_D will depend on the particle shape and orientation with respect to the flow as well as on the flow parameters such as the Reynolds number, Mach number, turbulence level, etc.

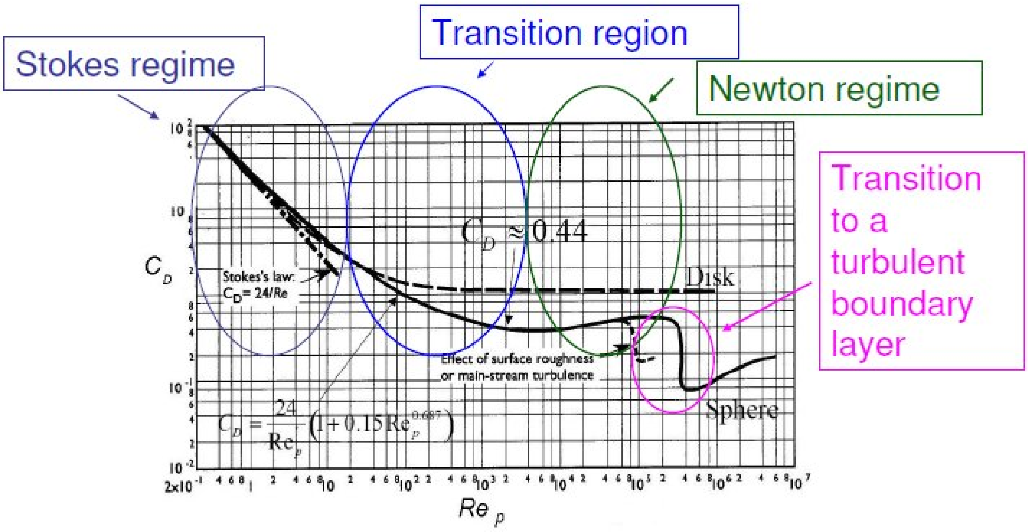

Figure 2.1: Drag coefficient of no-rotating sphere [24].

The Stokes drag force is based on a uniform free stream velocity. The Stokes drag has to be extended to account for the effect of a nonuniform flow field by an additional term in Eq (2.7) which denoted by $\vec{F}_{\text{Faxen}}$, represent the Faxen correction force. This correction is employed for linear gradients in fluid velocity over the surface of the particle given by

$$\vec{F}_{\text{Faxen}} = \mu_f \pi \frac{d_p^3}{8} \nabla^2 \vec{u}_f \tag{2.12}$$

where $\nabla^2 \vec{u}_f$ is evaluated at the position of the surface.

2.3.2 Added mass force

In the dynamics of the bubble motion, the virtual mass force is very important. Added mass force is due acceleration of a certain fraction of the surrounding fluid. The force is defined by:

$$\vec{F}_A = \frac{1}{2} m_p \frac{\rho_f}{\rho_p} \frac{d}{dt} (\vec{u}_f - \vec{u}_p) \tag{2.13}$$

The equation is derived from change in the total kinetic energy of the fluid surrounding a sphere. It is assumed that the fluid is inviscid and incompressible. It should also exist a potential field $(-\frac{Ua^3}{2r^3} \cos \theta)$ that satisfy the incompressible continuity equation.

The virtual mass effect relates to the force required to accelerate the surrounding fluid. The last part of Eq (2.13) represents the relative acceleration of the particle compared to the fluid along the path of particle.

The added mass force is important in liquid-solid flows where the densities are comparable ($\frac{\rho_f}{\rho_p} > 1$). For example the dynamic of a bubble motion. But for gas-particle flows where the ratio of continuous phase density to the droplet material density is very small, ($\frac{\rho_f}{\rho_p} << 1$) the added mass could be neglect.

2.3.3 Lift forces

Saffman lift force is given as

$$\vec{F}_{\text{saff}} = 1.61 d_p^2 \sqrt{\rho_f \mu_f} \frac{(\vec{u}_f - \vec{u}_p) \otimes \vec{\omega}_f}{\sqrt{| \vec{\omega}_f |}} \qquad \vec{\omega}_f \; = \; \nabla \otimes \vec{u}_f \tag{2.14}$$

This force is due to the pressure distribution developed on a particle due to rotational induced by a velocity gradient. The higher velocity on the top of the particle gives rise to low pressure and the high pressure on the velocity side gives rise to a lift force.

Saffman lift force is based on the conditions that the Reynolds number based on the velocity difference is much less than the shear Reynolds number i.e. $Re_r << \sqrt{Re_G}$ and both Reynolds number are much less than unity.

Magnus lift force for Reynolds numbers in the order of unity is given by

$$\vec{F}_{\text{Mag}} = \frac{\pi}{8} d_p^3 \rho_f \left(\frac{1}{2} \nabla \otimes \vec{u}_f - \vec{\omega}_p \right) \otimes (\vec{u}_f - \vec{u}_p) \tag{2.15}$$

This force is the lift developed due to rotation of the particle. The lift is caused by a pressure differential between both sides of the particle resulting from the velocity differential due to rotation. The rotation may be caused by a source other than the velocity gradient.

2.3.4 Basset force

Forces due to acceleration of the relative velocity can be divided into two parts: The virtual mass effect and the Basset force (history force). The virtual is explained in section 2.3.2.

The Basset force term account for the viscous effect. This term addresses the temporal delay in boundary layer development as the relative change in time. For example if one consider an impulsively accelerated infinite flat plate, the local shear stress is determined as

$$\tau = \mu_c \frac{\partial u}{\partial y}_{y=0}. \tag{2.16}$$

where u is the solution to the unsteady diffusion equation: $u = u_0 \text{erf}\eta$. However if the approach is the same as to impulsive flow over a sphere at low Reynolds number, then the Basset force will be given as

$$\vec{F}_{\text{Basset}} = \sqrt{\pi \rho_f \mu_f} \frac{m_p}{\rho_p d_p} \int_0^t \frac{1}{\sqrt{1 - t'}} \frac{d}{dt} (\vec{u}_f - \vec{u}_p) dt' \tag{2.17}$$

The value of Basset force depends on the acceleration history up to the present time. The Basset term like virtual mass term become insignificant for $\rho_f / \rho_p \sim 10^{-3}$ if $(\mu_f / \rho_f \omega d_p^2)^{1/2} > 6$ where ω is the frequency of the oscillating flow. Thus the Basset term could be neglected for small particle like $10 - \mu m$ at $\omega < 700$.

2.3.5 Pressure force

The effect of local pressure gradient gives rise to an force in the direction of the pressure gradient. The net pressure force acting on a particle is given by

$$\vec{F}_p = \int_S -p\vec{n}dS \tag{2.18}$$

Applying divergence theorem gives

$$\vec{F}_p = \int_V -\nabla p dV. \tag{2.19}$$

By assuming the pressure gradient is constant over the volume of the particle one has

$$\vec{F}_p = -\nabla p V_p. \tag{2.20}$$

The pressure gradient produced by hydrostatic pressure is

$$\nabla p = -\rho_f g \vec{e}_z \tag{2.21}$$

where the z is in the direction opposed to the gravity (upward). The corresponding pressure force is

$$\vec{F}_p = \rho_f g V_p \vec{e}_z \tag{2.22}$$

Which state that the force is equal to the wight of the fluid displaced. This is known as Archimedes principle.

In similar fashion, there is a force on the particle due to the shear stress (τ_{ij}) in the conveying fluid. This force can be written as

$$\vec{F}_P = \nabla \cdot \tau_{ij} V_p \tag{2.23}$$

Thus the total force due to pressure can be written as

$$\vec{F}_P = \frac{m_p}{\rho_p}\left(-\nabla p + \nabla \cdot \tau_{ij}\right) \tag{2.24}$$

The pressure gradient and shear stress can be related to the fluid acceleration from the Navier-Stokes Eq for the conveying fluid

$$-\nabla p + \nabla \cdot \tau_{ij} = \rho_f \left(\frac{D\vec{u}_f}{Dt} - \vec{g}\right) \tag{2.25}$$

Combining Eq (2.24) and Eq (2.25) gives

$$\vec{F}_{\mathrm{P}} = m_p \frac{\rho_f}{\rho_p}\left(\frac{D\vec{u}_f}{Dt} - \vec{g}\right) \tag{2.26}$$

with $\frac{D}{Dt}$ as material derivative. For flows, such as gas-particle flows, where the ratio of the continuous phase density to the droplet material density is very small ($\rho_f/\rho_p << 1$), the force acting on the body due to pressure could be neglected[1]. In fact, the pressure force is an important parameter in liquid-solid flows where the densities are comparable ($\rho_f/\rho_p > 1$).

2.3.6 Other forces

The term $\vec{F}_g$ in Eq (2.7) represents the gravity force, the mass of the particle multiplied with the gravitational acceleration constant.

The thermophoretic force represents the force due to a temperature gradient in the fluid. Hot molecules moves faster than cold molecules and a large temperature gradient will give a net force in the direction opposite to the temperature gradient gradient. This thermophoretic force is only important for very small particles and will lead to separation of particles depending on their size.

The origin of the Brownian force is random force collisions of individual molecules. This force is usually modeled as Gaussian white noise and is only important for submicron particles.

The forces due to turbulence are often modeled as a random addition to the fluid velocity that sustain during a time corresponding to the minimum of the lifetime of the turbulent eddies and the time for a particle to pass through a turbulent eddy [7].

2.4 Phase Coupling

An important concept in analysis of multiphase flows is coupling. Coupling can take place through mass, momentum and energy transfer between phases. Mass coupling is the addition of mass through evaporation of the removal mass from the carrier stream by condensation. Momentum coupling is the result of the drag force on the dispersed and continuous phases. Momentum coupling can also occur with momentum addition or depletion due to mass transfer. Energy coupling occurs through heat transfer between phases. Thermal and kinetic energy can also be transferred between phases owing to mass transfer.

There are three possible ways of coupling. If the flow of one phase affects the other while there is no reverse effect, the flow is said to be one-way coupled, which means that only the effect of the fluid on particles is important.

If there is a mutual effect between the flows of both phases, and it means that the effect of particles on the flow has to be incorporated in the continuous phase governing equations. If the flow is sufficiently dilute, particle interactions may be safely neglected. This is defined as two-way coupling.

If the volume faction is sufficiently large (above 10^{-3}), particle interactions becomes important. Particles interacts by means of collisions but also as more indirect phenomena, such as two particle approaching each other in viscous fluid. Although they will most probably not collide, their interactions may be still important. This is defined as four-way coupling.

[1] This not true for slurry flow

2.5 Multi-scale Modeling

CFD can be employed to reveal details of peculiar flow physics that otherwise could not be visualized by experiments, or clarify particular accentuating mechanisms that are consistently being manifested in complex multiphase flows. A range of pertinent multiphase studies based upon the judicious use of direct numerical simulation (DNS) or large eddy simulation (LES). Such an approach usually contains very detailed information, producing an accurate realization about the flow encapsulating a broad range of length and time scales. Because of the wealth of information that can be attained, DNS or LES is normally adopted as a research tool to effectively provide a qualitative understanding of the flow physics and to possibly construct a quantitative model, allowing other, similar, flows to be computed [30].

One multiphase model that is used in industrial purposes is discrete particle model (DPM) or point-particle approach.

2.6 Discrete Particle Model

In the DPM model the particles are tracked individually, and the gas phase is treated in a continuous framework. This can be done by resolving the flow around the particles, or by representing the particles as a source terms in the flow. In DPM technique, the single-phase Navier-Stokes Eqs are solved in conjunction with tracking the individual particles.

The Continuum-phase governing Equations can be written as

$$\frac{\partial(\alpha_f\rho_f)}{\partial t} + \nabla\cdot(\alpha_f\rho_f\vec{u}_f) = S_{mass} \tag{2.27}$$

$$\frac{\partial(\alpha_f\rho_f\vec{u}_f)}{\partial t} + \nabla\cdot(\alpha_f\rho_f\vec{u}_f\vec{u}_f) = -\alpha_f\nabla p_f - \nabla\cdot(\alpha_f\vec{\tau}_f) - S_p + \alpha_f\rho_f\vec{g} \tag{2.28}$$

where S_{mass} is the source term describing mass transfer between phases, and the source term S_p is given as

$$S_p = \frac{1}{V_{cell}}\int_{V_{cell}}\sum_{i=0}^{N_p}\frac{V_i\beta}{\alpha_p}(\vec{u_f} - \vec{u_p})\delta(x - x_p)dV \tag{2.29}$$

where β is the drag force coefficients. As one can see from Eq (2.29), the source term is only active at the center of the particle. From the S_p term, coupling of the phase, and each particle is through porosity α_p and inter-phase momentum exchange through Eq (2.28).

To account for high particle volume fraction, a volume fraction is introduced in the equations as well. To successfully employ this approach, the particles have to be much smaller that the fluid phase grid cells. This restriction arises because the velocity filed, $\vec{u}_f$ required to calculate the source term needed to be the undisturbed velocity field. It is also assumed that the force acting as a particle can be described exclusively from its interactions with the surrounding liquid and gas, the motion of a single particle without collisions with other particles can be governed by Newtons second law, Eq (2.6) and Eq (2.7) with given initial position for all particles. To solve the flow of the continuous fluid, traditional models such as RANS or LES, can be implemented into Eq (2.27) and Eq (2.28).

The presence of particles can also taken account in for example particle-particle interaction when the local volume fraction exceed 1% (we can't neglect the particle-particle effects). There are several kinds collisions approaches i.e., hard and soft sphere modeling. Both of them required a spherical shape (stochastic models for non-spherical particles) on the particles and the interaction between particles are typically treated as a particle-particle pair basis. Dependent of the particle volume fraction in the flow regime, different models can be used. For example if the flow regime is sufficiently dilute ($St_c < 1$), which means that the collision time scale $\tau_{\text{collision}}$ is important and the particle motion is governed by the continuous phase forces (one-way coupling is recommended i.e., particles do not effect the continuous phase and particles do not see each other). A suitable model approach is the hard-sphere collision model, which is based on impulsive forces. Three relevant parameter has to be determined in the hard-sphere model, the normal and tangential restitution coefficients e, ζ and the sliding resisted by coulomb friction μ.

If the flow regime is dense (two-way or four-way modeling is recommended) ($St_c > 1$) then the collisions time scale is an unimportant parameter. For contact dominated flows the soft model should be considered. In this model the deformation is considered and a maximum overlap δ has to be defined. Compare to hard sphere model a very small time step is needed.

3 Theory of Particle Image Velocimetry

This section describes a brief theory behind; principle of PIV, LIF-PIV, optical system and optical access, image evaluation by means of cross-correlation and seeding traces. The theory behind particle image velocimetry is enormously extensive. The state of the art of PIV was presented by J. Westerweel in his thesis Digital Particle Image Velocimetry Theory and Application published in 1993 [28]. However, the PIV technique is still being continuously developed. For interested reader se also M. Raffel et al. in [21]

3.1 Principle of PIV

Many technical and scientific developments requires a measuring technique that can measure the velocity distribution across an extended area of a flow field. This can be achieved by scanning a point velocity probe across the flow but then the instantaneous structure is lost and only the average flow field is obtained.

Flow visualization techniques can often reveal instantaneous flow structures but they are only qualitative or semi-quantitative at the best. An optical, non-intrusive method which is related to both the flow visualization and the optical point techniques have been developed over the last 20 years called PIV [21].

This technique can provide an accurate quantitative measurement of the instantaneous flow velocity field across a planar area of a flow field. Figure 3.1 briefly sketches a typical setup for PIV recording in a wind tunnel. The flow is seeded with tiny, neutrally buoyant particles - so called "tracers" e.g. oil or water aerosols in air and solid particles in fluids or flames.

Tracer particles are in-directly added to the fluid flow by using a light sheet, formed by passing a double pulsed laser beam through an optical arrangement including cylindrical lenses. The particles in the flow will be illuminated twice with a small time separation, Δt between the pulses.

The displacement of particles in the time between the laser pulses is recorded as either a single image exposed twice or as a pair of two single exposure images. The recorded particle displacement field is measured locally across the whole FOV of the images, scaled by the image magnification and then divided by the known pulse separation to obtain flow velocity at each point.

A camera positioned typically perpendicular to the plane of the light sheet is shuttered to capture the light scattered from the particles. Depending of the mean flow velocity and the factor of magnification of the camera lens, the delay of the two pulses have to be chosen such that adequate displacements of the particle images on the charge coupled device (CCD) are obtained.

From the time delay between the two illuminations and the displacement of the tracers velocity vectors can be calculated. For evaluation of the particle images it is assumed that the tracers follow the flow into the local flow velocity between the two illuminations. The illumination should be in such way that the particles do not produce steaks in the images.

The (digital) PIV recording is divided into small subareas - so called "interrogation Areas" (IAs), see figure 3.1. Using statistical correlation techniques one local displacement vector is determined for each Interrogation Area (IA). For this reason the size of the IA is selected such that all particles within this area have moved homogeneously in the same direction and at the same distance. For good results the number of particles within one IA should be at least ten.

The evaluation of the particle images depends on the way the images have been recorded by the used camera. One possibility is to record the scattered light of both illuminations in one frame which is called “single frame or double exposure”. These images can be evaluated by auto-correlation. The other possibility is to record the scattered light from the first illumination in one frame and the scattered light from the second illumination in another frame which is called “double frame/double exposure”. These double frame images can be evaluated by cross-correlation (CC) [4].

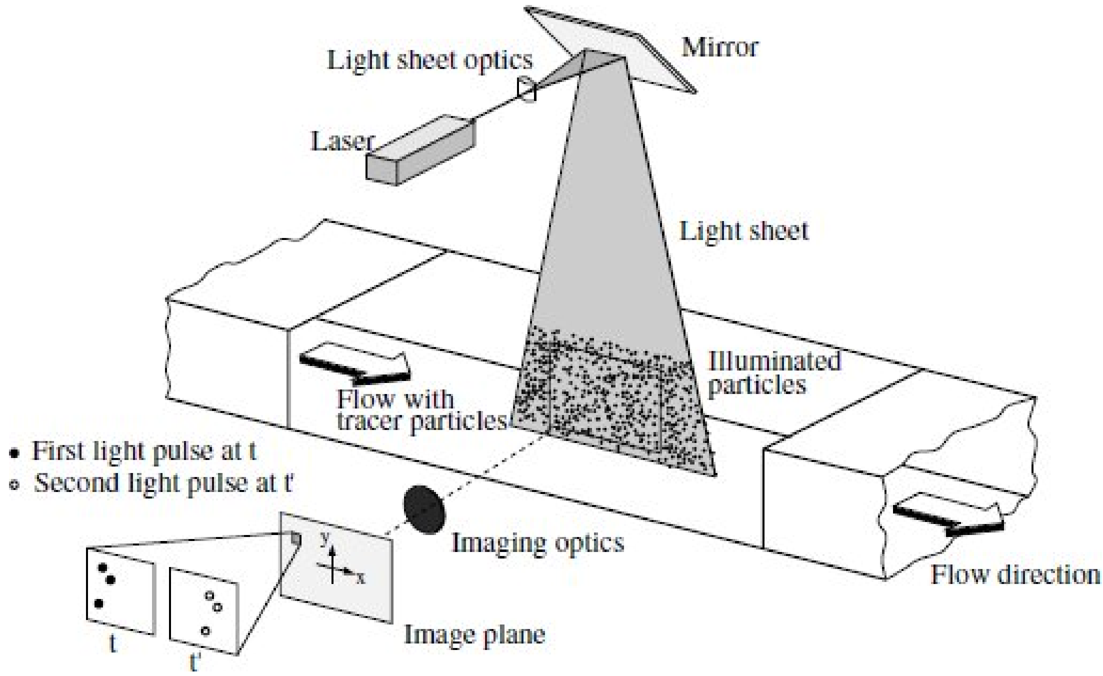

Figure 3.1: Experimental arrangement for particle image velocimetry in a wind tunnel [21].

3.2 LIF-PIV

The common light source for PIV is an Nd:YAG laser with a wavelength of $\lambda = 532\,nm$ which is observed as a green light. When "ideal" if visible particles are illuminated by a green light sheet they will back scatter light of the same color.

There are other fluorescent particles available which scatters orange light (e.g. PMMA Rhodamine B) when they are illuminated by green laser light [29]. This is called laser-induced fluorescence (LIF) and in connection with PIV it is also called wavelength discrimination (also called LIF-PIV). In order to achieve fluorescence the seeding particles are colored with Rhodamine. To get the benefit with PIV from LIF it is necessary to employ optical filters with the cameras.

In Figure 3.2 is a schematic representation of wavelength discrimination shown. Two filters are commonly used, a band-pass filter ($\lambda = 532\,nm$) for the green scattered light and a low-pass filter ($\lambda > 532nm$) for the orange scattered light, see figure 3.2(a).

It is possible to employ band-pass filters for standard PIV measurements, since the ambient light on the recorded images will be reduced. When measurements with LIF are performed and the camera is equipped with the low pass filter, only the orange scattered light is recorded. Since all unwanted reflections from walls or windows are in green light, they cannot pass the filter and therefore not obstruct the recorded image. This is a very efficient method used to increase the signal-to-noise ratio.

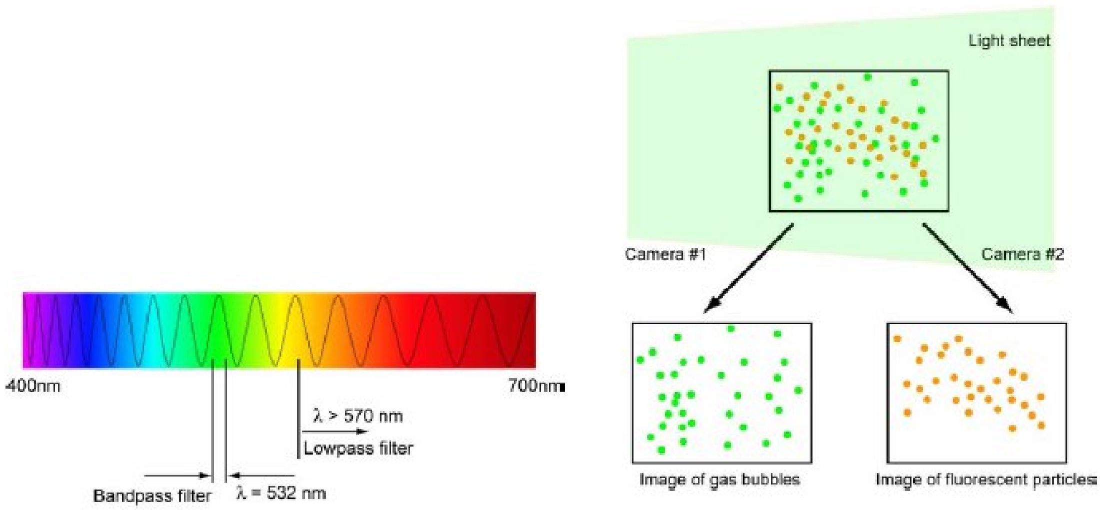

(a) (b)

Figure 3.2: Wavelength discrimination provides simultaneous gas-bubbles and liquid velocity results [29].

3.3 Optical system

Figure 3.3, shows a schematic representation of the light sheet and the optical system for imaging tracer particles in a planar cross of the flow. The system consists of an aberration free thin circular lens with a focal length f and a diameter D [28]. The lens law can be written as

$$\frac{1}{z_0} + \frac{1}{Z_0} = \frac{1}{f} \tag{3.1}$$

with z_0 as image distance and Z_0 as object distance. The image magnification factor is defined as

$$M = \frac{z_0}{Z_0}. \tag{3.2}$$

As we described in the previous section, the seeding particles in the object plane are illuminated with a coherent thin light sheet with the thickness as ΔZ_0 and with wavelength λ usually $532\,nm$. According to Adrian (1991), all trace particles observed in object plane are in focus if the following condition is satisfied:

$$\delta Z = 4\left(1 + \frac{1}{M^2}\right)^2 \frac{f^2\lambda}{D^2}. \tag{3.3}$$

Where δZ is the object focal depth. In order to avoid unfocused particle images, the object focal depth of the image should always be greater than the thickness of the light sheet.

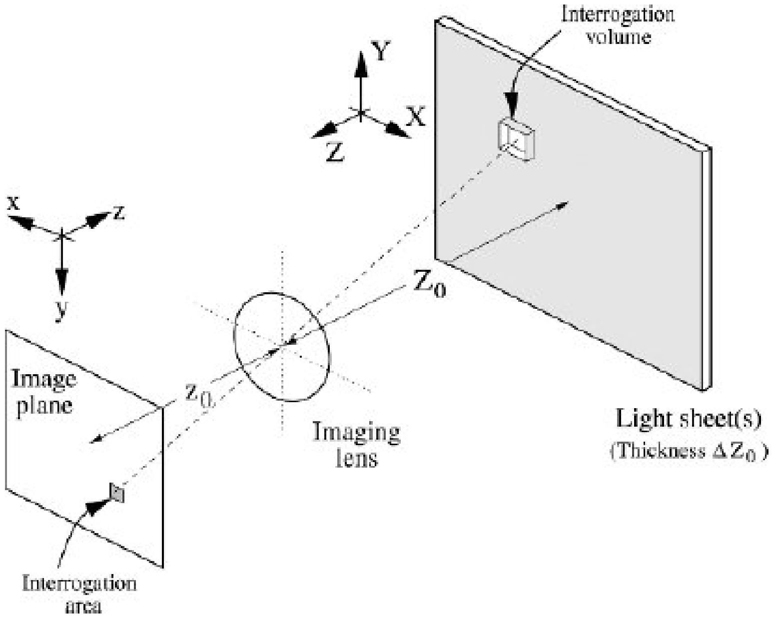

Figure 3.3: Schematic representation of geometric imaging [21].

3.3.1 Particle image diameter

The image size of a seeding particle which is recorded by means of a camera is affected by diffraction on the aperture of the lenses and can therefore not be directly calculated with the magnification-formula given in Eq (3.1). The image of a distant point source does not appear as a point on the image plane but forms a Fraunhofer diffraction pattern. Determination of particle image diameter d_t of a small circular object with diameter d_p is given by

$$d_t = \sqrt{M^2 d_p^2 + d_{\text{diff}}^2} \tag{3.4}$$

where d_{diff} is the diffraction (diameter of Airy disk) limited minimum image diameter, can be obtained from

$$d_{\text{diff}} = 2.44 f_{\#}(M+1)\lambda. \tag{3.5}$$

with f-number defined as:

$$f_{\#} = \frac{f}{D}. \tag{3.6}$$

The Airy function can mathematically be represented by square of the first order Bessel function and represents the impulse response, the so called point spread function of an aberration free lens. As seen from figure 3.4 the intensity pattern of a point source in the image plane. With decreasing aperture diameter which means increasing the lens stop numbers, the diameter of the Airy pattern increases. In practice the point spread function is often approximated by normalized Gaussian curve, shown in the figure 3.5 and defined by:

$$\frac{I(x)}{I_{\max}} = \exp\left(-\frac{x}{2\sigma^2}\right). \tag{3.7}$$

Where $I(x)$ is a light intensity in the image. And σ is the parameter equal to $f_{\#}(1+M)\lambda\frac{\sqrt{2}}{\pi}$, in order to approximate diffraction limited imaging. The normalized intensity distribution of the Airy function and its approximation by a Gaussian bell curve is shown in the figure 3.5. This approximation is useful due that it allows a considerable simplification of the mathematic derivation encountered in the derivation of modulation transfer function[21].

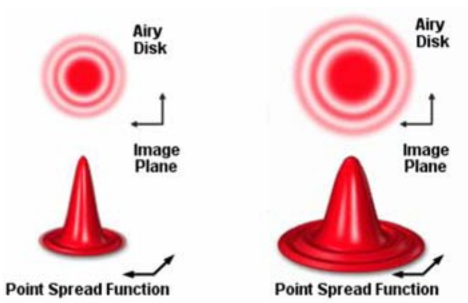

Figure 3.4: Airy patterns for a large (left) and a smaller aperture diameter (right) [1].

In practical situation the adjustment of f-number is the simplest way to change the particle image diameter d_t, as seen from Eq (3.4) and Eq (3.5). As see from the Eq (3.3),

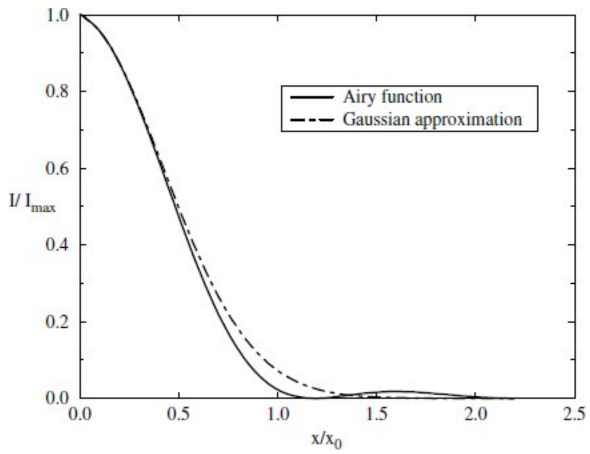

Figure 3.5: Intensity distribution of Airy pattern and its approximation by Gaussian bell curve [21].

the focal depth of the field δZ is effected by f-number through Eq (3.6). It can be seen that a large aperture diameter is needed to get sufficient light from each individual object within the light sheet, and to get sharp particle image. But the disadvantage of large aperture diameter yields a small focal depth which is significant problem when imaging small traces object. The effect of focal depth δZ and particle image diameter with respect to f-number is illustrated in table 3.1 for small particle with diameter of $10\,\mu m$ and magnification factor $M = 0.25$ and a light sheet with a wavelength of $\lambda = 532\,nm$.

Table 3.1: Theoretical values for diffraction limited imaging of small particles [21].

$f_{\#} = f/D$	$d_t\,[\mu m]$	$\delta Z\,[mm]$
2.8	4.7	0.5
4.0	6.6	1.1
5.6	9.1	2.0
8.0	13.0	4.2
11	17.8	7.8
16	26.0	16.6
22	35.7	31.4

3.3.2 Optimization of particle image diameter

As we described, the particle image diameter in a PIV system can be adjusted by the particle size, magnification factor and diffraction. The particle image diameter is important for evaluation of correct CC between the two images. As shown in figure 3.6 for CC between two images the optimal particle image diameter is slightly more than 2 pixels. According to Westerweel [27] if the particle image diameter d_t is larger than 2 pixel the RMS-Uncertainty error increases proportional to the particle image diameter. But when $d_t < 2$ pixel, the RMS-Uncertainty error increases rapidly, due to the fact that the shape of the correlation peak is no longer Gaussian, and thus the interpolation with Eq (3.7) is not a suitable choice as approximation of Airy function. Figure 3.6 show also the effect of interrogation window size for CC. For window size of $64 \times 64\,\text{pixels}^2$, the error is much smaller compared to the smaller window size, e.g. $16 \times 16\,\text{pixels}^2$. This is partly because, for a smaller interrogation area, the number of seeding particles would decrease as the window size decrease.

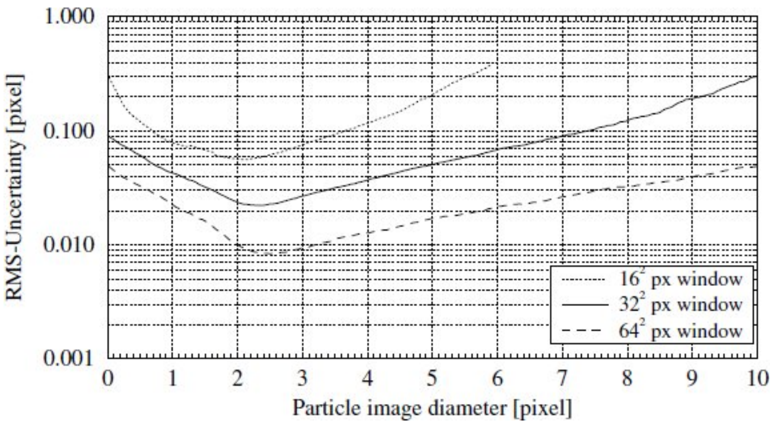

Figure 3.6: Measurement uncertainty in digital cross-correlation PIV evaluation with respect to varying particle image diameter taken for single exposure/double frame PIV imaging [21].

Another problem that may occur for too smaller particle images is the displacement tend to be biased towards the integral values. The effect increases as the particle image diameter is reduced, see figure 3.7. This bias error is caused by a "peak locking" effect. For vector fields the presence of this peak locking effect can be detected by plotting a displacement histogram, which serves as a good indicator that the systematic error are larger than the random noise in the estimated displacements. The peak locking effect depends on the size of the particle images, the size of the interrogation window and the density of particles. When the particle images are larger (compare figure 3.6, particle image diameter larger than 2 pixel), the achievable measurement uncertainty increases. The noise level of the correlation data remains constant with reference to the particle image size. Another factor for an accurate PIV evaluation is that small particle images are essential in order to obtain a high particle image intensity $I_{\max}$, since at constant light energy scattered by the tracer particle, the light energy per unit area increases quadratically with the decreasing image area ($I_{\max} \sim 1/d_t^2$). This fact also explains why increasing the particle diameter does not always compensate for insufficient laser power.

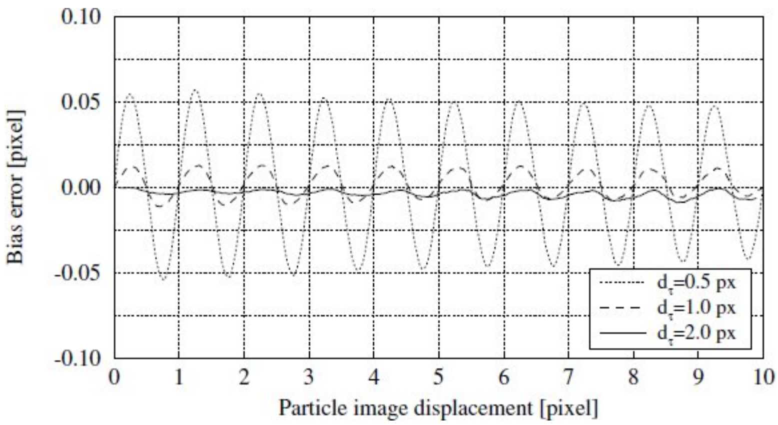

Figure 3.7: “Peak locking” is introduced when the particle image diameter is too small [21].

3.4 PIV Evaluation method

In this section we are treating the technique for recording PIV evaluation. In spite of the fact that the most realizations of PIV systems are quite similar. In nearly every case they are based on digital performed Fourier algorithms (FFT). As described in section 3.1 there are different methods in order to illuminate the seeding particles in the flow. The PIV recording modes can be classified into two main categories:

- methods which capture the illuminated flow on to a single frame and
- methods which provide a single illuminated image for each illumination pulse.

These branches are referred to as single frame/multi-exposure PIV and multi-frame/single exposure PIV, respectively.

In our experiment we performed only illumination technique based on the second case, therefore we will limit us to the multi-frame/single exposure.

3.4.1 Cross-correlation

For cross-correlation (CC) a fast double shuttered CCD camera is typically used in order to record images with “double frame/double exposure”. Two subsequent images of the flow, separated by a short time delay, Δt, are divided into small interrogation areas (IA’s) see figure 3.8. The volume-averaged displacement, $d(\vec{x}, t)$, of the particle images between the IA in the first image and the IA area in the second image is determined by means of a cross-correlation analysis. When the interrogation areas contain a sufficient number of particle images (at last 10) the CC consists of a dominant correlation peak embedded in a background of noise peaks. The location of the tall peak is referred to as the displacement-correlation peak, or velocity:

$$\vec{u}(\vec{x}, t) = \frac{\vec{d}(\vec{x}, t)}{M \Delta t} \tag{3.8}$$

provided that Δt is sufficiently small, and M is the magnification factor describe in section 3.3. Each correlation operates only on the intensities inside the IA’s. The CC from one IA results in one velocity vector as shown in figure 3.8. The CC can be interpreted as finding which relative displacement of the IA’s resulting in the best pattern match. This displacement should be proportional to the average velocity in the IA’s.

The size of IA is typically $2^n \times 2^n$ pixels^2, with $n = 2, 4, 8, \ldots$. For example in our experiment we use 32×32 pixels^2. The IA should not be too small, partly because small IA's will lead to a high number of displacement vectors. Since the velocity vector in an IA is a local average, it is recommended that the velocity variation within flow field that is mapped by IA is less than $5 - 10\,\%$ to avoid zero-velocity biasing [3].

There are different methods to calculate the CC function. A method to direct compute an unbiased sample CC function $R_{II'}(x, y)$ is defined by:

$$R_{II'}(x,y) = \begin{cases} \frac{1}{(M-|x|)(N-|y|)} \sum_{m=1}^{M-x} \sum_{n=1}^{N-y} I(m,n)\, I'(m+x, n+y) & x, y \geq 0 \\ \frac{1}{(M-|x|)(N-|y|)} \sum_{m=1}^{M+x} \sum_{n=1}^{N-y} I(m-x,n)\, I'(m, n+y) & x < 0,\, y \geq 0 \\ \frac{1}{(M-|x|)(N-|y|)} \sum_{m=1}^{M-x} \sum_{n=1}^{N+y} I(m,n-y)\, I'(m+x, n) & x \geq 0,\, y < 0 \\ \frac{1}{(M-|x|)(N-|y|)} \sum_{m=1}^{M+x} \sum_{n=1}^{N+y} I(m-x,n-y)\, I'(m, n) & x, y < 0. \end{cases} \tag{3.9}$$

The variables I and I' are the samples (e.g. intensity values) as extracted from the images where I' is the larger than the template I. Essentially the template I is linearly "shifted" around the sample I' without extending over edges of I'. For each choice of sample shift (x, y), the sum of the products of all overlapping pixel intensities produces one CC value $R_{II'}(x, y)$. By applying this operation for a range of shifts ($|x| \leq M$, $|y| \leq N$) a correlation plane the size of $(2M + 1) \times (2N + 1)$ is formed. For shift values at which the samples particle images align with each other, the sum of the products of pixel intensities will be larger than elsewhere, resulting in a high CC value $R_{II'}(x, y)$ at this position, see figure 3.8. Essentially the CC function statistically measures the degree of match between the two samples for a given shift. The highest value in the correlation plane can then be used as a direct estimate of the particle image displacement.

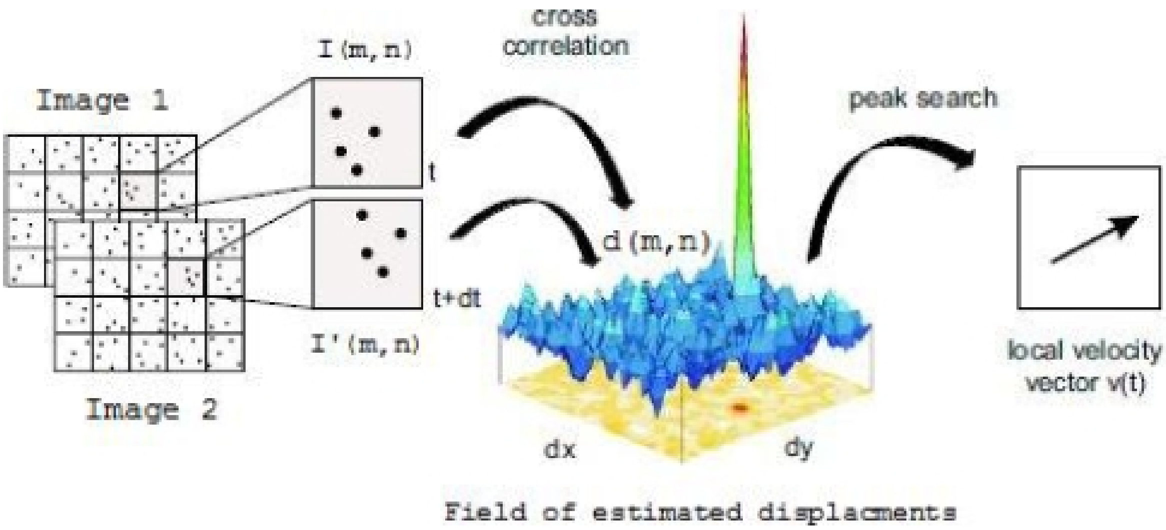

Figure 3.8: Evaluation of PIV recordings using cross-correlation [4].

3.4.2 Cross-correlation function via finite Fourier transforms

A more convenient way to estimate the CC functions (see figure 3.9) is use fast Fourier transforms (FFTs). Partly because, the direct implementation of the CC function from Eq (3.9) would be inefficiently for large data-sets. The FFT's algorithm reduces the computation from order of N^4 operations to order of $N^2 \log_2 N$ operations for the case of a two-dimensional correlation.

When Fourier transform are used, one take the advantage of the correlation theorem which state that the CC of two functions is equivalent to a complex conjugate multiplication of their Fourier transforms:

$$R_{II'} \Leftrightarrow \widehat{I} \cdot \widehat{I'}^{*} \tag{3.10}$$

Where $\widehat{I}$ and $\widehat{I'}$ are the Fourier transforms of the functions I and I', respectively and $\widehat{I'}^{*}$ represents the complex conjugate of $\widehat{I'}$. The FFTs computational efficiency is mainly derived by recursively implementing a symmetry property between the even and odd coefficients of the discrete Fourier transform.

Using FFT's means treating the data as if it is periodic. The periodicity can rise to aliasing if the particles have moved a distance larger than half the size of the IA. The solution to aliasing problems is to either increase the IA size or to reduce the time delay between pulses Δt. A more serious problem with the FFT's is that bias errors occurs if these are not taken in account. In fact the finite size of the overlap of the images becomes smaller with an increasing displacement. This bias results in an underestimation of the peak magnitude for all displacements other than zero. To avoid this bias, a weighting functions can be applied to the CC function. This weighting function is founded by convoluting the samples weighing functions [26].

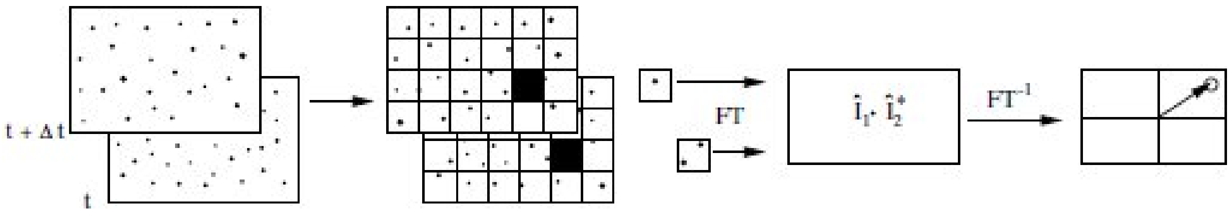

Figure 3.9: Evaluation of cross-correlation by means of FTT's [21].

3.4.3 Peak detection and subpixel interpolation

After CC has been performed a magnitude of the displacement is found by detecting the location of the highest correlation peak. Only detecting the peak will result in an uncertainty of $\pm 1/2$ pixel in the peak location.

By implementing a method, which is based on curve fitting and interpolation of the correlation data to some functions, the accuracy of the location of the highest correlation can be sufficiently increased. This may sound like "inventing" some new information which has not been measured before. But the procedure can be defended with the argument that the correlation is based on the images of several particles. If, for example, an IA pair contains ten particle images and eight particles has a displacement of 3 pixels and two particles has a displacement of 2 pixels, the maximum correlation peak would be located at 3 pixels but a subpixel interpolation can predict the correct displacement of 2.8 pixels, since the correlation at two pixels will be higher than the correlation at four pixels.

One approach is to increase the accuracy of the location of the highest correlation peak, is to use three adjoining values only, in order to estimate a component of displacement. The three-point estimators works typically best for rather narrow correlation peaks formed from particle images in the range of $2-3$ pixel diameters. The most common frequently implemented so called three point estimators is the Gaussian peak fit. The reasonable explanation for this is that the particle images themselves, if properly focused, describe Airy intensity functions which are approximated very well by a Gaussian intensity distribution, see section 3.3.1. When the maximum peak has been detected at $[m,n]$, the neighboring values are used to fit a function to the peak. In the case of a Gaussian peak fit, the peak is assumed to have the shape

$$f(x) = C \exp\left[\frac{-\left(x_0 - x\right)^2}{k}\right]$$

the displacements are found by:

$$\begin{aligned} x_0 &= m + \frac{\ln R_{(m-1,n)} - \ln R_{(m+1,n)}}{2\,\ln R_{(m-1,n)} - 4\,\ln R_{(m,n)} + 2\,\ln R_{(m+1,n)}} \\ y_0 &= n + \frac{\ln R_{(m,n-1)} - \ln R_{(m,n+1)}}{2\,\ln R_{(m,n-1)} - 4\,\ln R_{(m,m)} + 2\,\ln R_{(m,n+1)}} \end{aligned}$$

Other ways to interpolate at the subpixel level are parabolic peak fit and peak centroid.

3.4.4 Window overlap

The overlap defines the overlap among neighboring interrogation windows. The bigger the specified overlap, the closer is the net of the computed velocity vectors. The number of pixels for each interrogation window are not affected. The interrogation window size and the window overlap determine the grid size of a vector field. This is, the spacing between two neighboring vectors in the vector field. e.g a window size of 32×32 pixels (see figure 3.10) and an overlap of 0% results in a grid size of 32 pixels. A window size of 32×32 pixels and an overlap of 50% results in a grid size of 16 pixels. The position of the first vector at the top left corner of a vector field is determined by the grid size only. The convention is that the pixel position (x/y) is determined by half the grid size, i.e. If the grid size is 32 pixels the top left vector is located at the position of (16/16) and if the grid size is 16 pixels the vector is located at the position of (8/8). This convention allows vector arithmetic on vector fields that have been calculated with different interrogation window sizes, but with the same grid size [4].

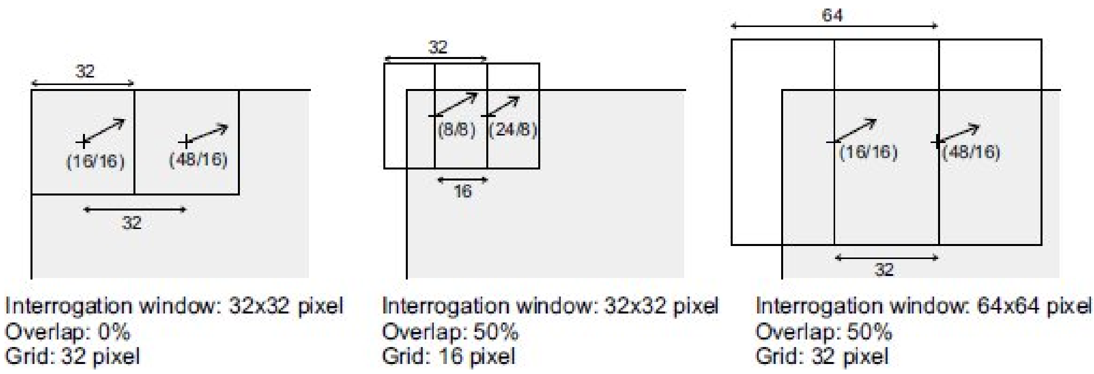

Figure 3.10: Vector position depending on interrogation window size and overlap [4].

3.4.5 Adaptive multipass

The adaptive multipass algorithm calculate first a reference vector field for each processed record. The algoritm uses the computed vector field information as a reference vector field for the next pass. The interrogation windows are shifted in the new pass according to reference vector field values, in order to match the right particles for the correlation. The PIV recording can be evaluated several times with the same interrogation window size, or the interrogation window size can be halved for the next pass. In the adaptive multipass method with a decreasing window size, the cell shift is adaptively improved in order to compute the vectors. In the following steps, more accurately and more reliably ensures that the same particles are correlated with each other, even if small interrogation windows are used. It is possible to use a much smaller final interrogation window size than what would be possible without an adaptive window shifting. This improves the spatial resolution of the vector field and produces less erroneous vectors. For example, if a final interrogation window size of 32×32 pixels is used, then with a fixed window shift of 0 pixels it is only possible to calculate vectors with a ± 16 pixels displacement at most, (in practice only ± 8 pixels). In a flow field with large fluctuations, larger vectors can still be computed by using the adaptive multipass algorithm, since the cell shift is locally adapted to the mean local flow.

In this study one use an initial 64×64 pixels cell size, even large vectors are calculated with good reliability. These vectors are then used as a window shift for the final $32 \times 32\, px^2$ calculation.

3.5 Responce time of tracer particles

The response time of a particle or droplet to changes the in flow velocity are important in establishing non-dimensional parameters to characterize the flow. In fact, this is very important for PIV measurements, because the PIV technique measure the fluid velocity, (continuous phase or disperse phase) with respect to tracer particles. Therefore, fluid mechanical properties of the tracers particles have to be checked.

The equation of the motion for a spherical particle in fluid is given by Eq (2.6), with drag force in Eq (2.8) and pressure force in Eq (2.22) and with gravity force gives

$$\frac{d\vec{u}_p}{dt} = \frac{18\mu_f}{(\rho_p - \rho_f)d_p^2}\frac{C_D Re_p}{24}(\vec{u}_f - \vec{u}_p) \tag{3.11}$$

where Re_p is defined in Eq (2.11). For limits of low Reynolds number (Stokes flow, see Stokes law), the factor $C_D Re_p/24$ approaches unity. The step response of $\vec{u}_p$ is typically following an exponentially law:

$$\vec{u}_p(t) = \vec{u}_f(1 - \exp^{-t/\tau_v}) \qquad \tau_v = \frac{(\rho_p - \rho_f)d_p^2}{18\mu_f} \tag{3.12}$$

where τ_v defines the momentum response time. Thus the momentum response time is the time required for a particle released for the rest to achieve 63 % ($\frac{e-e}{e}$) of the free stream velocity. If the fluid acceleration is not constant or Stokes drag does not apply, the solution to particle motion is no longer exponential decay of the velocity.

As one can see, the momentum response time is most sensitive to the particle size illustrated in figure 3.11.

One important parameter of specifying the ratio of momentum response time and continuous phase time (characteristic time of the flow, (τ_c)) scale is Stokes number:

$$St = \frac{\tau_v}{\tau_c} \tag{3.13}$$

As we see, if the particle size is sufficiently large i.e. $\tau_v >> \tau_c$ which means ($St >> 1$), the particle will have no time to respond the fluid changes. But if $\tau_v << \tau_c$ then the particle follow the continuous phase, which means that the velocity of the particle and continuous phase are almost the same.

When applying PIV to liquid flows, the problems of finding particles with matching densities are usually not severe, and solid particles with adequate fluid mechanical properties can often be found [21].

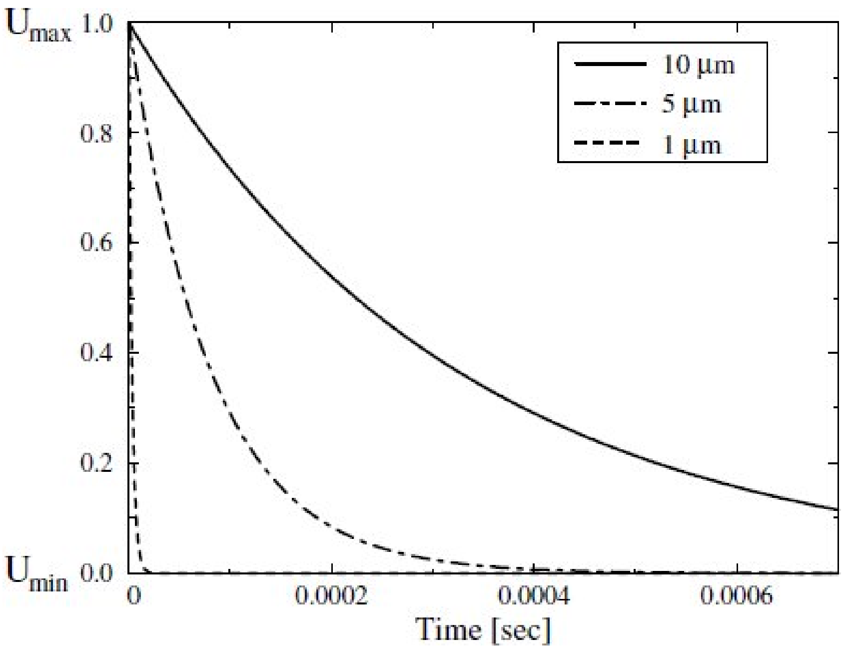

Figure 3.11: Time response of oil particles with different diameters in decelerating air flow [21].

4 Available Multiphase PIV Methods

The use of laser-based measurement techniques have a lot of potential which can be seen from the number of publications where Laser-Induced Fluorescence (LIF-PIV), Particle Image Velocimetry (PIV), Planar Fluorescence For Bubble Imaging (PFBI), Particle Tracking Velocimetry (PTV)[2] or a non-intrusive optical technique like shadow photography (ST) for planar diagnostic of two-phase flows, have been developed to provide experimental information of two individual phases in multiphase flows.

Depending on the flow structure which are considered one should decide to process the images with PTV or PIV techniques. Due to fact that there can be a wide range of particle concentrations (i.e. the concentration of tracer particles), bubble gas concentration (void fraction) differing from one interrogation area to another. This choices is not so easy, as illustrated in figure 4.1 from Niels et al. [11]. A close-up of a PIV recording and the IA's can be seen. In IA $D3$ there are only tracer particles present, while the entire IA $C1$ is filled with bubbles. In each IA only the velocity of one phase can be determined. Obvious, the choice of the most accurate kind of measured techniques is not an easy task.

According to Adrian [5], there are various possibilities for optical velocimetry. By listing the leading candidates for various types of illuminations, types of coding, types of particles, types of image recording and types of interrogation, given about $3-5$ different candidates for each of these categories, there were several hundred combinations that might have produced potentially viable systems.

In this section we will the describe advantage and disadvantage of some of available LIF-PIV/PTV measurement techniques which is most used in literature. For example Hassan et al. [13], Reese et al. [23] and Lin et al. [18] all used PTV for both disperse-phase (gas bubbles) and the continuum-phase (liquid phase, measured with tracer particles). Hassan et al. [13] performed measurements of both the gas and the liquid phase in a system of single bubbles rising in a heavy mineral oil. In order to be able to detect the particle images, the bubbles needed to be overexposed. The bubble images consisted of overexposed round spots. A threshold function was used to determine the position of the edges of the bubble. Then both the tracer particles and the bubbles were tracked.

An example of the wavelength discrimination technique described in the theory section 3.2 is Pedersen in [22] who made comprehensive measurements in a plexiglas pump with this technique. Another approach for wavelength discrimination technique is the measurement of two-phase flows, for example air/water or cavitation/water, see Sommerfeld et al. and Honkanen et al. in [9, 14]. They used two CCD cameras for measuring the velocity field in a two-phase flow. Velocity of the continuum-phase is recorded with the first camera, which is equipped with the low-pass filter in order to detect the orange particles, while the second camera with the band-pass filter will detect the cavitation or disperse-phase, see figure 3.2.

A number of non-intrusive optical techniques for planar diagnostic of two-phase flows have been developed in order to provide experimental information which were previously inaccessible. For example Bongiovanni et al. [8] used the ST technique, extensively to measure the location and shapes of bubbles in the flow with a relatively low void fraction (less than $1-2\,\%$). This technique can easily be combined with the LIF-PIV technique by using appropriative optical filters for light sources with different wavelengths.

The use of one or two (in our experiment we will use one camera only) cameras in the ST together with the LIF-PIV allows the bubble dynamics and their interaction with

[2]PTV is a special case of PIV, i.e when the average distance between the particles is much larger than the mean displacement. Since the seeding density in PTV is much lower than in PIV, a much lower spatial resolution can be obtained

continuum-phase to be studied in details, e.g. Lindken et al. [19]. In Particular Sommerfeld et al. [9] studied the bubble-induced turbulence in a two-phase column flow for void fraction up to 19 %. By using two cameras, they estimated simultaneously the instantaneous velocity fields of the continuum-phase and disperse-phase with wavelength discrimination (LIF-PIV) and PTV approaches. But one of the main problem faced in the ST is overlapping of the bubble images, which occurs when the void fraction is too high.

The most recent advanced image-processing methods, which effectively analyze experimental data images of dense two-phase flows with irregularly shaped particles of dispersed-phase, were introduced by Sommerfeld et al. [25], and Honkanen et al. [16]. These procedures extended the range of ST applicability to a higher degree. However, to determine the bubble position relative to the camera focus plane, it is necessary to exploit an additional camera, usually oriented 90 degrees to the main camera. But when the void fraction is too high, it is quite difficult to identify the same bubble with the two different cameras and to determine the bubble position in the 3D space.

A relatively new method described in Dehaeck et al. [12] is based on determining the glare points at the surface of a bubble located inside a laser plane. This method allows the spatial distribution of bubble velocity and sizes to be obtained with high accuracy, using a single laser sheet and one camera. To further increase the accuracy of this method two light sources allows refractive index of bubbles to be recorded. But unfortunately this approach, (interferometric technique) result in a relatively bad prediction for low void fraction (less than 1 %) and small sizes of rounded bubbles or droplets.

Recently Yerbol et al. [6] applied a method based on laser-induced fluorescence, Planar Fluorescence for Bubble Imaging (PFBI), which represent a convenient tool to identify round bubbles located within and very close to the laser sheet. One of the advantage of this technique is that the bubbles located far from the measurement plane becomes rapidly defocused and experimental information in a certain rectangular measurement volume with a low thickness can be retrieved. But this method is restricted to a relatively low bubbly flow with void fraction up to 6 % and small sizes of round bubbles.

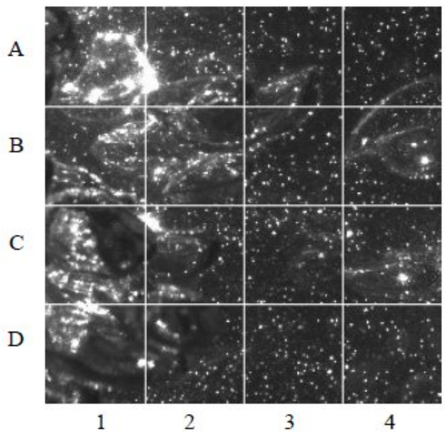

Figure 4.1: Close-up of a PIV recording of the gas liquid flow in a bubble column, showing 16 interrogation areas of 64 × 64 pixel^2 [11].

5 Experimental setup and Method

The measurement was carried out around a single modelled gear wheel within a modelled gearbox. Essentially the measurement should be carried out with the $BOT402$ oil which is the same oil used in lubrication of gears. PIV measurements in liquid requires the fluid to be transparent, but the $BOT402$ oil is almost black/dark red. We have spent a lot of time in order to find a transparent oil with the same properties as the $BOT402$. It was important that the oil should have same kinematic viscosity as well as density, and besides that it should be transparent. After several suitable candidates, we finally mange to find several oils which could match the $BOT402$ oil. One of the candidates was silicon oil, but the disadvantage of this kind of oil is the very high price. Figure 5.1 shows the suitable candidates to replace the $BOT402$ oil. Among them, only two oils could be selected; $T9$ and $NYFLEX2014B$ oil. As one can see the $NYFLEX2014B$ could match $BOT402$ at room temperature $T \sim 25\,°C$, therefore the $NYFLEX2014B$ was selected and the PIV experiment was carried out of "BOT402" at $T \sim 70\,°C$. According to NYNAS oil the density of the $NYFLEX2014B$ is $\sim 878\,kg/m^3$ at $15\,°C$ and refractive index approximately 1.478 at $20\,°C$ and the oil is clear and bright at $15\,°C$.

A schematic view of PIV components in the experiment are illustrated in figure 5.5. A test rig was built representing a simplified model of a gearbox. The rig is specially designed for using PIV which means the optical access to the flow is maximized. The gearbox size is $0.82 \times 0.52 \times 0.32\,m^3$ (see figure 5.2) and two different wheel models in SLS, with a diameter of $224\,mm$ and thickness of $28\,mm$, one of them have a smooth surface and the other one have teeth (spur, 67 teeth), are considered in the measurement, see figure 5.4 and figure 5.3. The spur gears or straight cut gears are the simplest type of gears. They consists of cylinder or disks, with the teeth projecting radially, and although the shape does not consists of straight smooth sides. The edge of each tooth is straight and aligned parallel to the axis of rotation.

Figure 5.4 and 5.3 shows the illumination of laser plane with respect to the wheel symmetry plane which means that the measurement of a single gear was carried out at the midpoint of the wheel thickness. Also the wheel model is made interchangeable and the wheel rotation speed can be varied to investigate different operational conditions. The PIV system for planar velocity field measurements consists of one 2048×2048 pixel resolution CCD camera (LaVision Imager pro $X\ 4M$) with $7.4\mu m \times 7.4\mu m$ pixel and a 400 mJ/pulse double-pulsed Nd-YAG laser, illuminated at $532\,nm$ (Spectra-Physics) parallel to the flow. The flow was seeded with fluorescent particles (PMMA Rhodamine B) with a diameter of $1 - 20\,\mu m$ and density of $1.5\,kg/m^3$. During illumination of laser this fluorescent particles will emit orange light, which can be separated by a low-pass filter connected to a CCD camera.

The thickness of the light sheet was approximately $5\,mm$. The exposure time-delay is $640\,\mu s$ at $50rpm$. The optical axis of the camera was normal to the plane of the light sheet. The area of the recorded light sheet that was $50 \times 50\,mm^2$ in the smaller field of view and $250 \times 250\,mm^2$ in the larger field of view. For larger filed of view, the focal length was $28\,mm$ and $105\,mm$ in smaller field of view. As we described in section 1.2, it was not possible to measure the whole flow filed around the wheel simultaneously. But since we could ran the wheel in two different directions, this issue was solved by running the experiments in two modes; reverse and forward directions. In this way we could perform postprocessing of both measurement areas and build this two measurements together to obtain a velocity field around the gear wheel. As shown in table 5.1 and table 5.2 the measurement parameters are the same for reverse as well as for forward rotational direction under the condition of the flow with respect to wheel symmetry plane is symmetric.

Table 5.1 and table 5.2 shows also the experimental parameters of the small as well as large recordings. In particular the repetition rate of the trigger signal per wheel rotation (TR) is determined by

$$f = \frac{1}{T} \tag{5.1}$$

$$T = \frac{S}{U} \qquad S = \pi D \qquad U = \frac{\omega}{60}\pi D \tag{5.2}$$

Where D is the wheel diameter and U is the wheel tip speed. The maximum frequency of trigger was $20Hz$ at rotation rate (RR) of $1200rpm$. At most the number of recordings was 100 frames with two recording sets. For higher RR above $400rpm$, too many bubbles and droplet of different sizes and shapes was generated as the wheel rotated. Also foam will be created above the oil level. This phenomena will influence the PIV measurements by means of the particle images to be too blurry and the optical access will be limited. To counteract this effect we simply perform the measurements of higher rotational speed in a "transient" mode. For example in case of a rotational speed of $400rpm$, we determined the time needed to perform the measurement without that the particle images in the recordings are too blurry. As seen from tables, for rotational speed of $400rpm$, the number of recording frames was decreased. Instead we increased the number of recording sets to 3 times larger than $50rpm$. This procedure was going on until the next measurement, of course for the next measurement we needed to wait at least 20 minutes, so that the created bubbles and foam could be able to dissipate.

Due to a strong temperature dependency of viscosity, we needed to measure and control the temperature in the oil inside the gearbox. The monitoring was done by installing a thermometer which was not influencing the flow field. Initially the rig was equipped with a large number of thermocouples installed below the surface of the box, which could monitor the temperature. But unfortunately the needles connected to the bottom wall of the box, affected the flow filed. Therefore we removed the thermocouples and installed a single thermometer far from the flow and recordings area to insure that the thermometer could not influence the measurement results. The measurements were performed at room temperature, $\sim 25 \pm 1\,°C$. With $0.1\,°C$ in change of the temperature inside the gear box, could result in approximative 1% of change in the kinematic viscosity. Before each measurement we have performed a warm-up and adjusted the temperature of the oil by running the rig at very high rotational speed in several minutes. In fact, to increase the temperate by $3\,°C$ it was necessary to run the wheel up to 20 minutes with a rotational speed of $1200rpm$.

As seen from the table values, the experiment was carried out at four different rotational speeds ω. The lowest speed was $50rpm$ and the highest was $1200rpm$. In order to "freeze"[3] the wheel during the measurement a referencee time must be determined. As seen from tables this time is dependent of the rotational direction. The referencee time can be determined by

$$t_{\text{referencee}} = C_{\text{correction}} \frac{T}{n_{\text{teeth}}}. \tag{5.3}$$

Where n_{teeth} is the number of teeth for the case of spur gear wheel, the correction term is determined after some trial and error procedures, for a speed of $50rpm$, this is determined to $\simeq 0.28$. A vertical line was drawn (from midpoint to the edge of the wheel) at the wheel before the measurement. As the wheel rotated and images were taken, a suitable choice of the referencee time showed that the line did not move at all. In that case the wheel is said to be "frozen" during the measurements, otherwise the wheel would rotate during the recording which could complicate the visualization of the flow field around the wheel. The synchronization of reference time was govern by an external trigger connected to the PIV processor, which also controlled all the signals from the CCD camera and Nd-Yag laser, see figure 5.5. In order to find appropriative power of the laser pulses before the PIV recording a lot of time was spent in order to find suitable values of laser pulses. The power of the laser pulses could partly be changed manually or via a computer connected to the PIV processor. A problem that we noticed, when we found the appropriative pulse values, suddenly after some time, the power of pulses was changed. But this problem could be solved, partly because we noticed the measurement must be performed immediately, otherwise the laser would be to cold. The time delay Δt between the laser pulses are shown in table 5.1 as well as in table 5.2, for different levels rotational speed. This parameter is very important for predicting a good PIV result. The time between the pulses is dependent of the flow field time scale which is in our case, complicated to evaluate, partly because when we are performing simultaneously measurements of the flow field above as well as below the oil level. Besides that the interface between oil and air with the rotating wheel would create different flow field time scales. By analyzing the movement and distribution of particles from PIV images, we could decide whether the time was a good choice or not. As seen from tables the time delay is proportional to rotational speed and decreases as the rotational speed increases. The explanations to this is for lower rotational speed the motion of the flow inside the gearbox is slower hence the particles moves slower, which means that the particles needs more time to move during the exposure of laser light.

[3] In that way one can synchronise transient measurements and also obtain the mean velocity information between teeth.

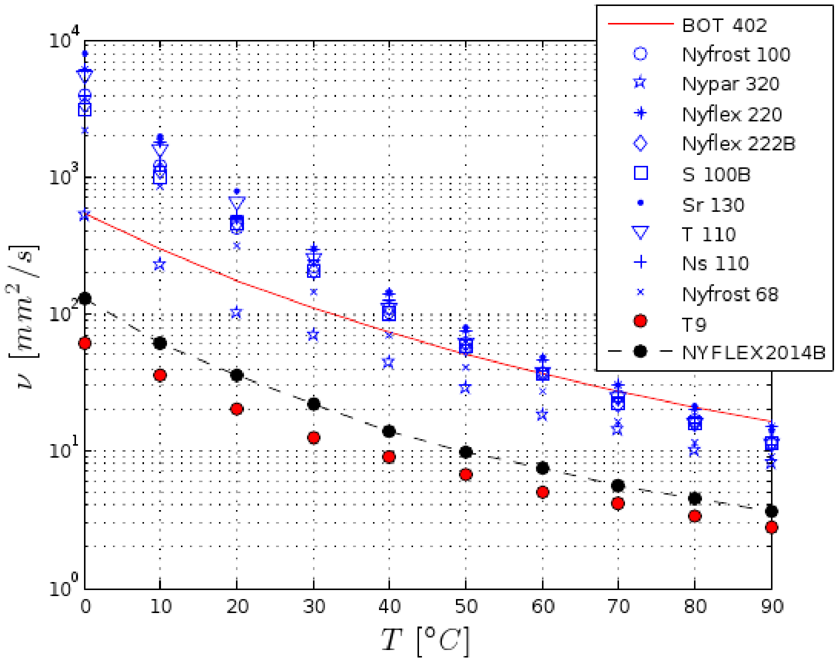

Figure 5.1: Kinematic viscosity of selected transparent oils compared to BOT402.

Table 5.1: Experimental value of PIV measurement parameters of smooth gear and spur gear wheel.

Rotational direction: forward and reverse
Power of two laser pulses A/B: 100/65 %
Oil temperature: $\sim$ 25 $°C$
Field of view camera: $50 \times 50\, mm^2$

ω $[RPM]$	U $[m/s]$	Δt $[\mu s]$	$t^{reverse}_{referencee}$ $[ms]$	$t^{forward}_{referencee}$ $[ms]$	TR $[Hz]$	# of frames	# of recording
50	0.586	640	5	4.2	0.833	100	1
100	1.17	320	2.5	2.1	1.667	100	1
200	2.35	160	1.25	1.05	3.333	100	2
"Transient" measurement							
ω $[RPM]$	U $[m/s]$	Δt $[\mu s]$	$t^{reverse}_{referencee}$ $[ms]$	$t^{forward}_{referencee}$ $[ms]$	TR $[Hz]$	# of frames	# of recording
400	4.69	80	0.625	0.525	6.667	50	3
1200	14.1	27	0.21	0.175	20	15	3

Table 5.2: Experimental value of PIV measurement parameters of smooth gear and spur gear wheel.

Rotational direction: forward and reverse
Power of two laser pulses A/B: 100/73 %
Oil temperature: $\sim 25\,°C$
Field of view camera: $250 \times 250\,mm^2$

ω $[RPM]$	U $[m/s]$	Δt $[\mu s]$	$t^{\text{reverse}}_{\text{referencee}}$ $[ms]$	$t^{\text{forward}}_{\text{referencee}}$ $[ms]$	TR $[Hz]$	# of frames	# of recording
50	0.586	3200	5	4.2	0.833	100	1
100	1.17	1600	2.5	2.1	1.667	100	1
200	2.35	800	1.25	1.05	3.333	100	2
"Transient" measurement							
ω $[RPM]$	U $[m/s]$	Δt $[\mu s]$	$t^{\text{reverse}}_{\text{referencee}}$ $[ms]$	$t^{\text{forward}}_{\text{referencee}}$ $[ms]$	TR $[Hz]$	# of frames	# of recording
400	4.69	400	0.625	0.525	6.667	50	3
1200	14.1	133	0.21	0.175	20	15	3

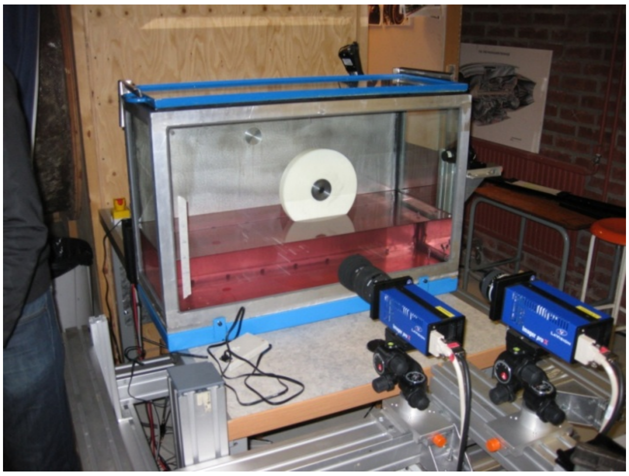

Figure 5.2: Modelled gearbox and gear wheel. Showing the experimental configuration and direction of the CCD camera.

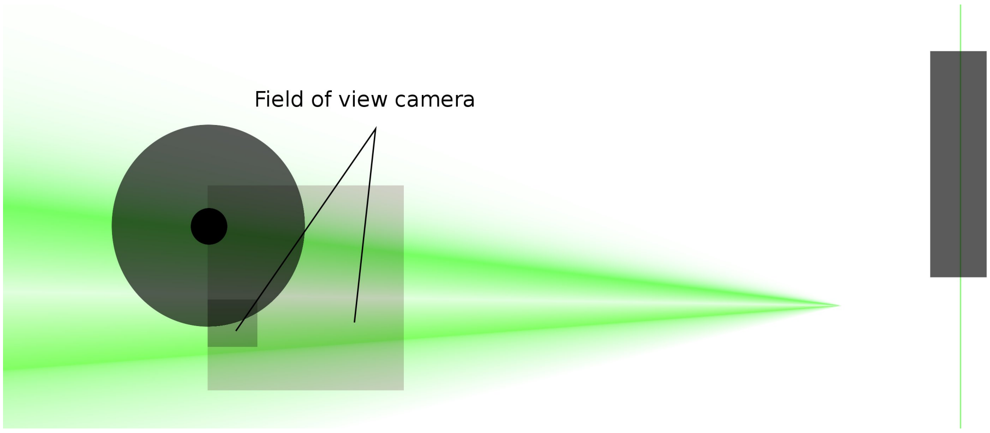

Figure 5.3: The relative position of the laser sheet and two recording areas, $50 \times 50\,mm^2$ and $250 \times 250\,mm^2$. The laser sheet is located at the center plane of the wheel thickness (right).

Figure 5.4: Modelled spur gear wheel [2]. The laser plane is located at wheel symmetry plane (midpoint of face width). The wheel has same dimension as smooth gear and consists of 67 spur teeth.

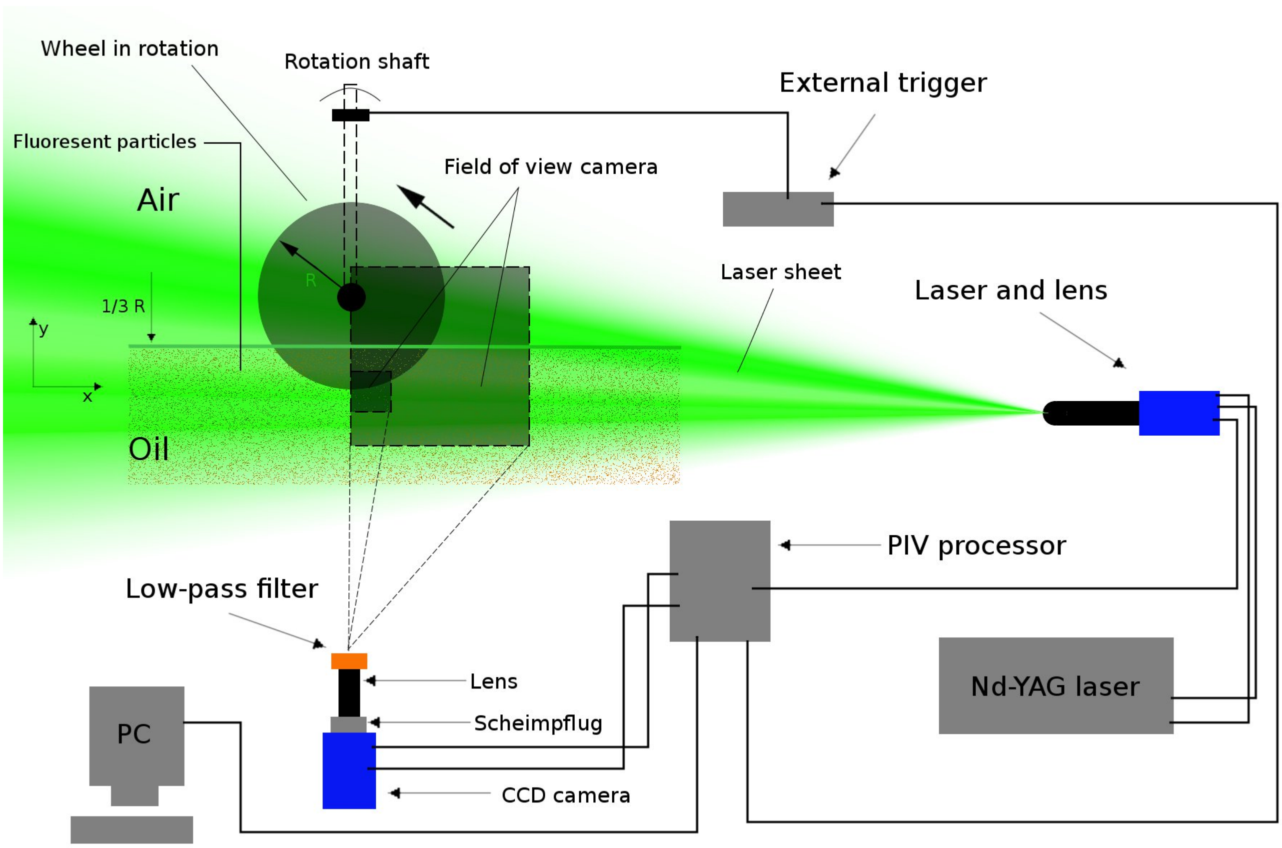

Figure 5.5: Schematic view of experimental components. The figure show three main components in PIV measurements of planar velocity field around rotating modeled gear wheel; the CCD camera (LaVision Imager pro $X\ 4M$), a 400 mJ/pulse double-pulsed Nd-YAG laser, operating at 532 nm (Spectra-Physics) and a PIV processor. The flow is seeded by fluorescent particles (PMMA Rhodamine B) with diameter of $1-20\,\mu m$ and density of $1.5\,kg/m^3$. The recording area (FOV) consists of two field; $50\times50\,mm^2$ and $250\times250\,mm^2$ in the larger fields.

6 Results of PIV measurements for Smooth wheel

In fact there was no data nor literature (actually we spend a lot time to find some kind of literature in order to guide us), available about this kinds of measurements. Therefore it was not possible for us to compare the PIV results. Like mentioned before, this project was an initial step and qualitative as well as quantities studies are indeed to study this kind of multiphase flow. As we will se in figures from further sections, when the wheel started to rotate, bubbles will be generated and specially for the spur teeth wheel, air bubbles will stay still in between the teeth. This effect was until now unknown as far as we know when we discussed with CFD groups from SAAB Fluid mechanics. The question for them was now how to model and which kind of multiphase model one can use between the spur teeth. However this questions are not considered in this study, we just want to point out the importance of qualitative studies. In the next section the results of qualitative studies of our observation are considered by means of raw PIV images. First we will show the images of smooth modelled gear wheel, which is in rotation during the illumination of tracer particles. Note that the tracer particles can be seen as white spots in the figures.

6.1 Raw images of Large Field of View Camera

This images where acquired with help with PIV Lavision program. The measurements and images in larger view of camera was taken at two different rotational modes, independently in reverse and forward direction. Due to that we have interface between oil and air, the laser light intensity naturally varied in this regions. In fact the intensity varied in such a way that bubbles reflect the laser light and created a local variation of laser intensity in the recording area (this is the reason why we sometimes show two raw images of same RR). As a consequence of increasing RR, effects would be significant and of course this will lead to larger disturbance which can effect the PIV results in a negative way.

6.1.1 Reverse direction

Figures 6.1, 6.2 and 6.3 show the raw images of smooth gear in the large field of view with varied rotational speed. As the wheel rotated in reverse direction (CCW), bubbles were generated, and raised in the opposite direction of the wheel direction. In fact, bubbles will be created due to streams that will be created on the left hand side of the wheel. Also one can see that concentration of bubbles is quite small for 50rpm compare to 400rpm and 1200rpm. So one can conclude the bubble concentration to be proportional to rotational speed. As one can observe, some bubbles are out of focus during the laser illumination (see figures, 6.1(c) and 6.3(a)), partly because the bubbles are behind/in front of the laser plane. This effect will not influence the PIV results. We could see that some bubbles blocked the laser light (streaks were created behind the bubbles), which is not a desired effect, partly because for good PIV measurements the laser light should be uniform. The amount of background noise increased as these bubbles increased in numbers, hence in those regions, numbers of spurious vectors may be increased as well. However, for lower rotational speed this is not a significant factor. At 50rpm, no bubbles are generated during rotation. Only a small stream is created and this stream will grow until 200rpm and one could observe that large bubbles are created, as this stream “hits” the surface of the oil, which generates random sizes of air bubble structures below the oil level as well as oil droplets above the oil level (air). Very close to the wheel, which is a very important region of measurements, it seems that bubbles are created and they have shapes like hydrofoils. These air structures are created due to motion and interaction between the air that follows with large streams when they breaks up into smaller streams. When the rotational speed increases above 200prm the stream will eventually collapse. At this stage the flow is fully turbulent and chaotic with huge oil drops and splash above the oil level. The effect of the splashing is very clear in RR of 1200. As seen in figure 6.2, large oil drops "hits" the surface which also generates large air bubbles. This is one of the reasons why it is difficult to measure fluid flow fields at higher rotational speed. The bubbles simply block the laser light which is crucial for getting a good PIV result. One interesting thing that we can see from higher RR is bubbles below the oil level and below the wheel which are quite uniform in the size. In that regions the disperse phase velocity is small and as a consequence the bubbles will accumulate in regions which increases the void fraction.

As we will see in mean field and vector field velocity profiles, the streams will generate quite large eddy structures and local vortices in some regions. Specially at 100rpm, we observe that when the coherent stream ran into the oil (see figure 6.1(b)) it produced local vortices quite far from the wheel.

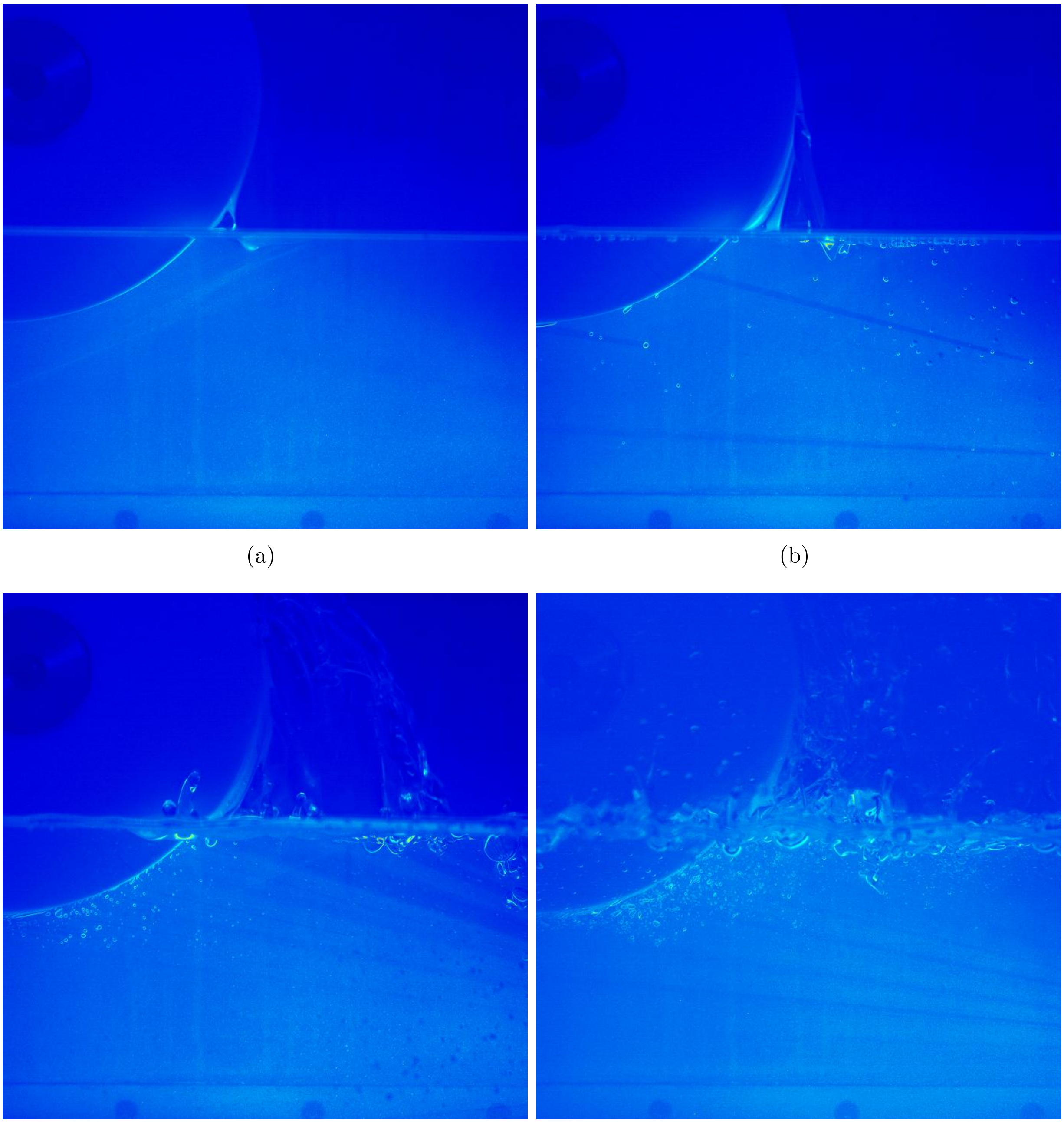

(a)

(b)

(c)

(d)

Figure 6.1: Raw image, reverse direction, large field, (a): 50 rpm, (b): 100 rpm ,(c): 200 rpm, (d): 400 rpm.

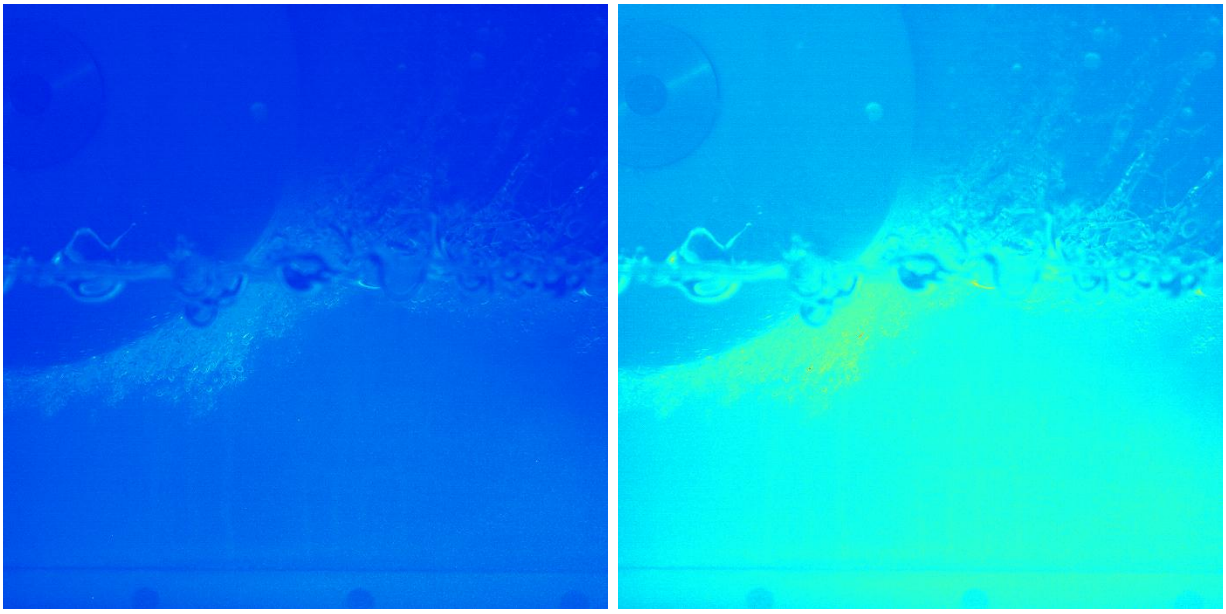

(a) (b)

Figure 6.2: Raw image, reverse direction, large field of 1200 rpm at different image brightness scalings.

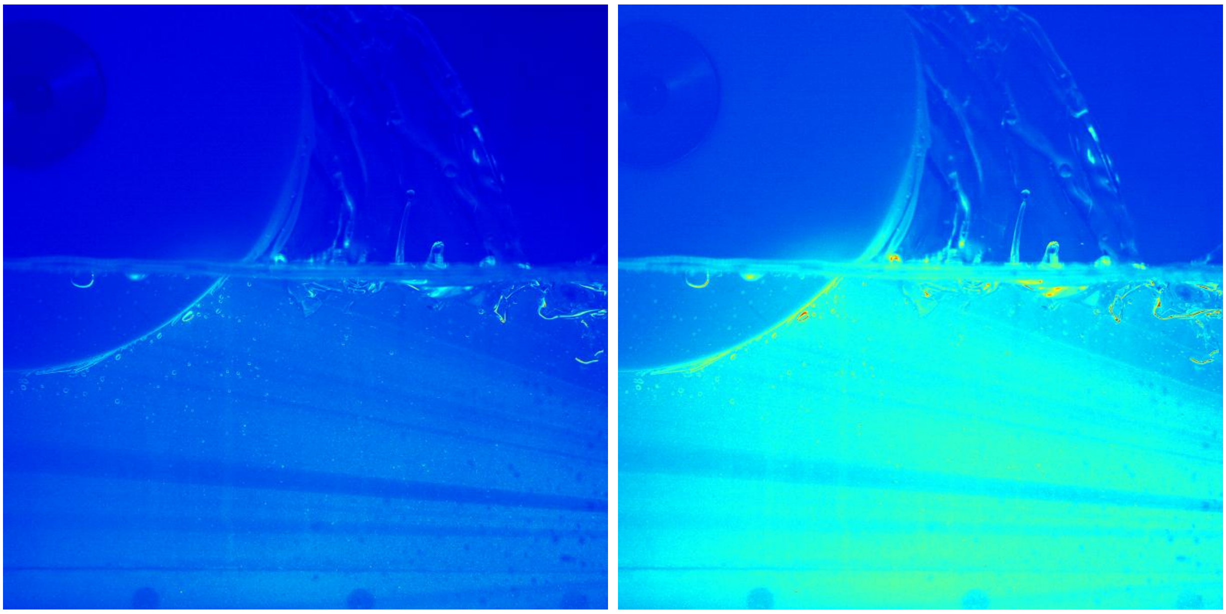

(a) (b)

Figure 6.3: Raw image, reverse direction, large field of 200 rpm at different image brightness scalings.

6.1.2 Forward direction

By comparing the rotational direction in forward versus reverse from previous discussion, one can conclude that the number and the amount of bubbles are quite small, even at $1200rpm$, see figures 6.4 and 6.5. But the shapes and the sizes of the bubbles are not the same in the forward as in the reverse direction. Specially at $100rpm$ the bubble shapes are like hydrofoils and they exists as several separated single bubbles close to the wheel. Another interesting thing, we have only streams above the oil level at $200rpm$, in fact there are no streams at all at low rotational speed. The effect of oil drops can earliest be seen as the RR increases to $400rpm$. At RR's of $400rpm$ the streams seems to be fully collapsed, (to be compared with the reverse direction where the streams are still present at RR's of $400rpm$). As RR increases we can see the same phenomena below the oil level. In particular below the oil level under the wheel where the void fraction is quite high and the bubble boundary thickness is somehow uniform in the shape and follows the wheel. The bubble eventually increases, and far from the wheel they will finally vanish. From figures 6.4(a) and 6.4(b), it can be seen that the modelled gear wheel reflect the laser light and this effect results in overexposure to the bubbles. This is not a desired property, (the ideal case would be if the modelled gear wheel were transparent). In fact the bubbles will increase the noise level in the evaluation of the PIV measurements, partly because of the existence of local variations of laser and overexposed as well as underexposed tracer particle can cause the increase of the error of the image of the tracer particle diameter. But note, when using laser discrimination method, bubbles “can” be seen as tracer particles, because the scattered light from the trace particles can light up the bubbles and hence will be shown in the PIV images. They can increase the noise level as well as spurious velocity vectors. More about spurious vectors and the elimination of them will be discussed in detail in further sections.

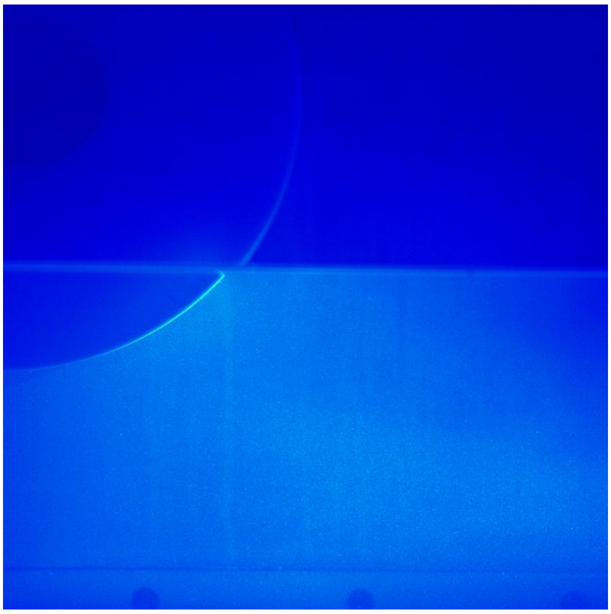

(a)

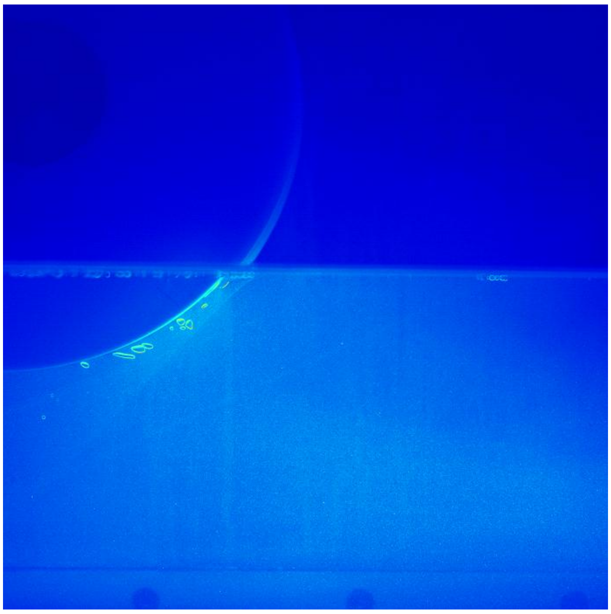

(b)

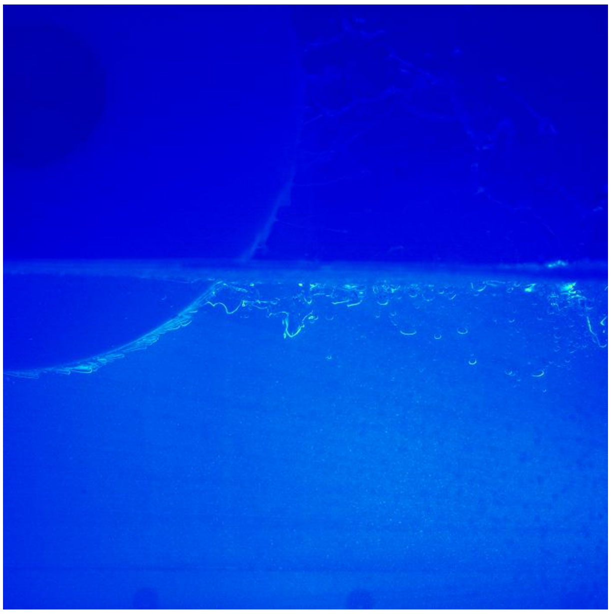

(c)

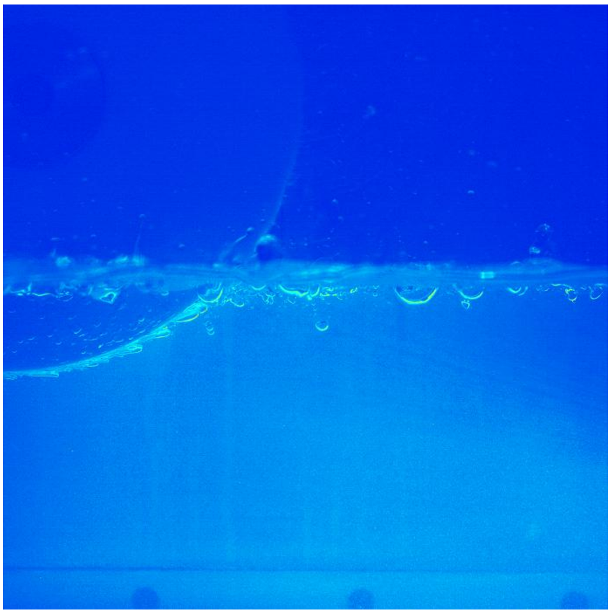

(d)

Figure 6.4: Raw image, forward direction, large field,(a): 50 rpm, (b): 100 rpm ,(c): 200 rpm, (d): 400 rpm.

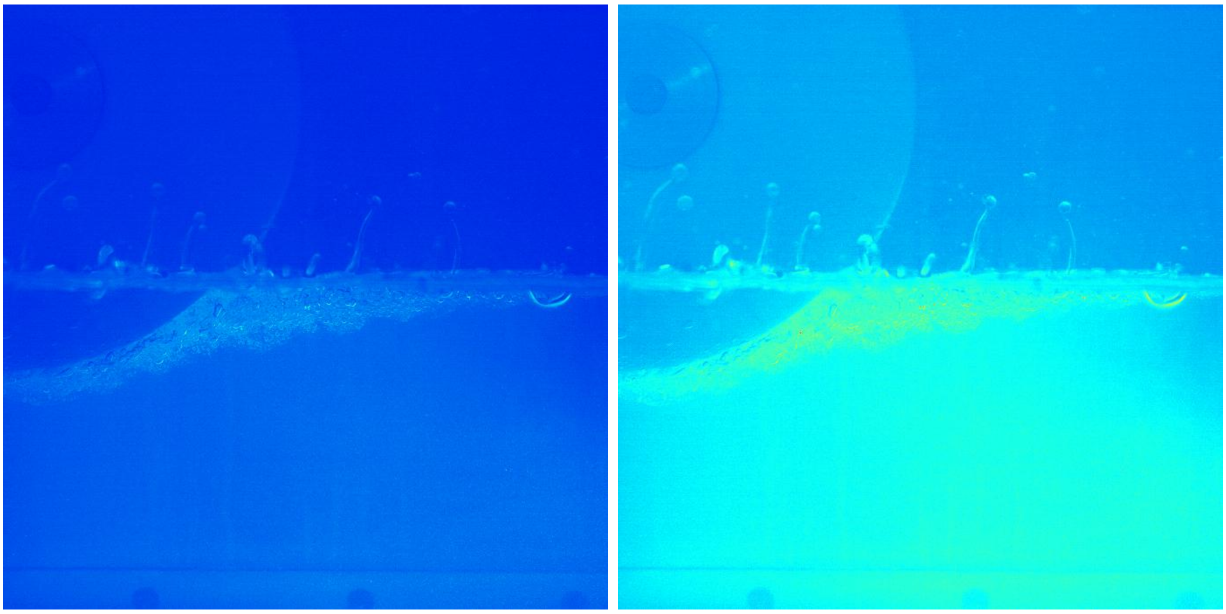

(a) (b)

Figure 6.5: 1200 rpm at different image brightness scalings.

6.2 PIV images of small Field of View Camera

Raw PIV images are shown in figures 6.6, 6.7, 6.8 and in figure 6.9 for rotational motion of forward as well as reverse direction. The measurements are in the region below the wheel, i.e. a small recording area. In the small recording area the bubble shape can bee seen in more details. Like in the previous discussion, bubble concentration increases when RR increases. Also by comparing the images from reverse and forward direction we see how the reverse direction generate more bubbles. Figure 6.7 shows the RR of 1200rpm where the bubble concentration is high, and hence, may result in bubbles blocking the laser light. Basically in forward direction one can see bubbles attaching to the wheel surface and builds up layer of bubbles, see figures 6.6(c,d) and 6.8(c,d).

6.2.1 Reverse direction

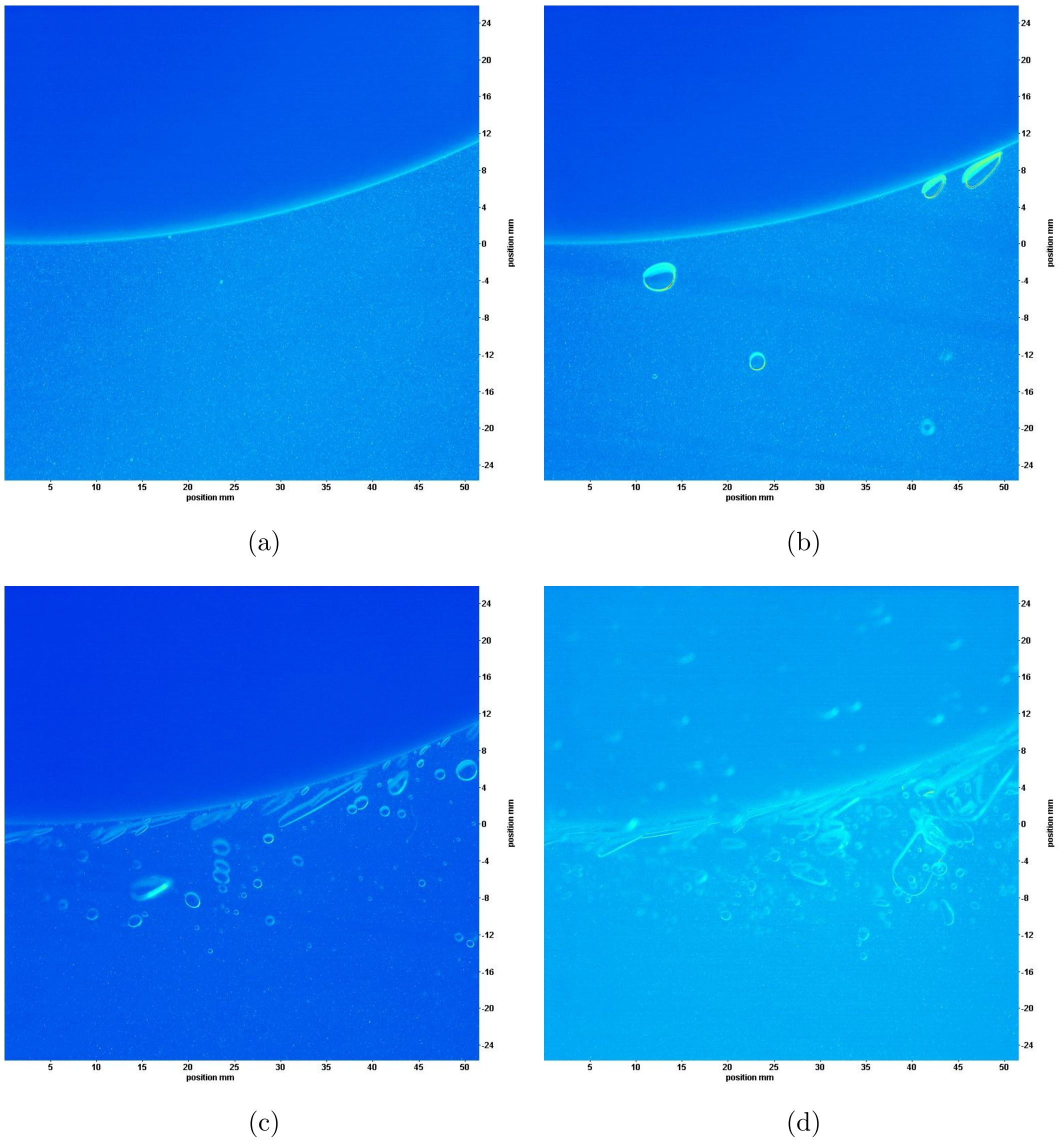

Figure 6.6: Raw image, reverse direction, small field,(a): 50 rpm, (b): 100 rpm ,(c): 200 rpm, (d): 400 rpm.

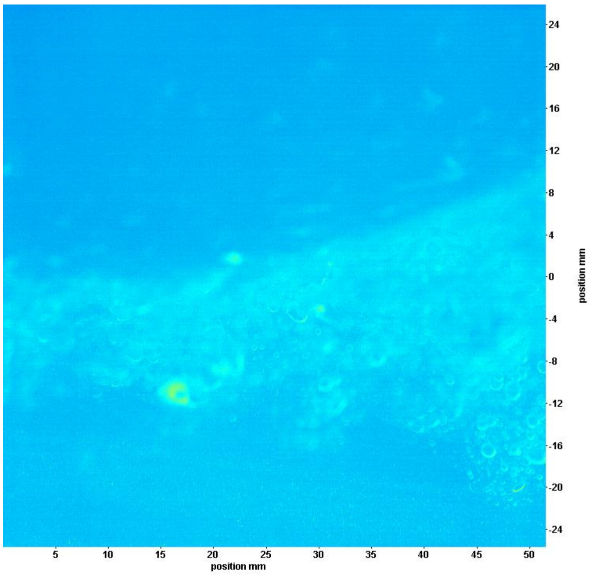

(a)

Figure 6.7: 1200 rpm

6.2.2 Forward direction

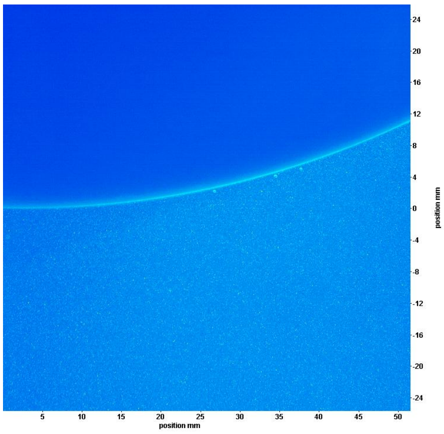

(a)

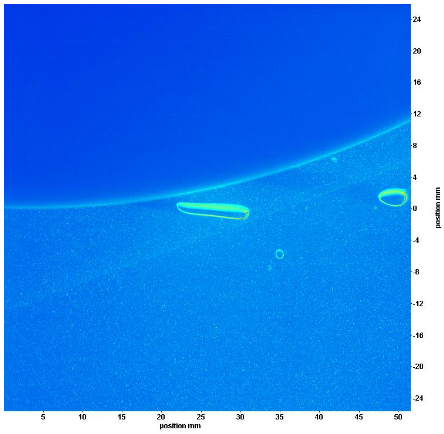

(b)

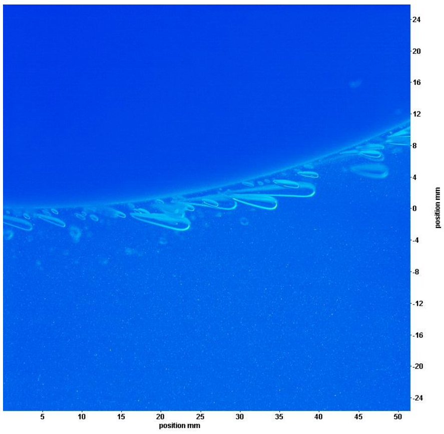

(c)

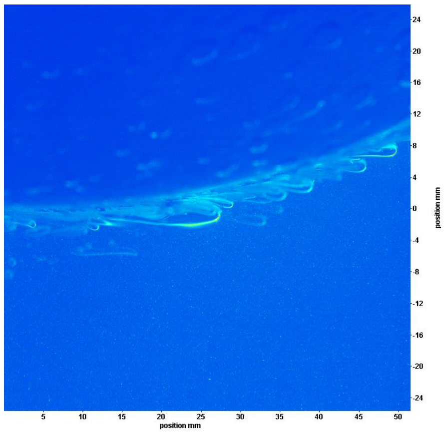

(d)

Figure 6.8: Raw image, forward direction, small field,(a): 50 rpm, (b): 100 rpm ,(c): 200 rpm, (d): 400 rpm.

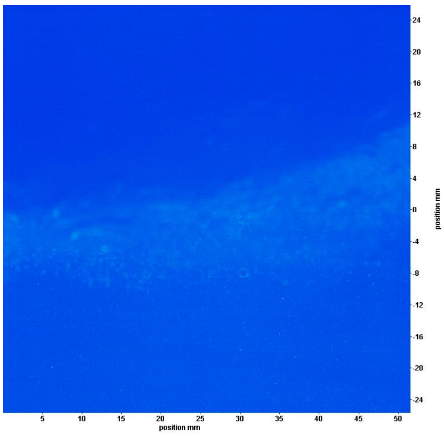

(a)

Figure 6.9: 1200 rpm

6.3 Mean Velocity Fields

As describe previous, the PIV measurement was carried out in two rotational directions, reverse and forward direction. In order to get a flow field profile over the whole wheel, we simply build this two measurement cases together. In fact, we also mask the wheel after evaluation of velocity vectors. Such a way is more suitable in order to see the flow field around the wheel. Via statistical validation the spurious vectors as well as too slow bubbles (large bubbles that does not follow the liquid) could be removed from the PIV images. Figure 6.10 and figure 6.11 shows the overlapped image and instantaneous velocity of 200rpm in reverse direction in a smaller recordings area of two different time intervals. The figures show how small bubbles follow the fluid and large bubbles moves very slow (in fact via rms-criteria velocity vectors of slow moving bubbles are removed). The velocity magnitude variation is in the range of 0 to 2 m/s. In some regions we can not see any velocities of the liquid been recorded. This can be explained by that the laser light was probably not uniform during the illumination, as a consequence of existence of bubbles in the liquid. In evaluation of the instantaneous field we uses RMS of velocity fluctuation (σ) as a statistical criteria (standard deviation). In order to remove spurious vectors and slow bubbles we used (3σ) as a statistical criteria.

Figure 6.12 and figure 6.13 shows the result of PIV measurements of mean field velocity profiles. Both rotational directions are build together and the result of the mean fields are after averaging of a certain number of frames. The number of frames are different for different speeds (see table 5.2 and 5.1). The Digital evaluation of these profiles are performed both in MATLAB and LAVISION program FlowMaster. The 2048×2048 px^2 image was processed by a multipass algorithm starting with IA of 64×64 with a 50% window overlap and with final pass of 16×16. The mean velocities are scaled with maximum RR which allow us to compare the results in a more simple way. Basically we can see that the maximum velocity is located at the wheel surface. At RR's of 50rpm the flow seems to be laminar. Suddenly at 100rpm we have a transition of laminar flow to turbulent flow and at 200rpm the flow seems to be fully turbulent. As discussed earlier at 50rpm the flow pattern of the stream that ran into the oil can be seen very clearly. High velocity when reached the surface level and continue to decrease far from the oil depth (y-direction). An interesting observation is how the flow around the wheel are dominated at the top of the right hand side of the wheel until 100rpm and suddenly switches to the left hand side of the wheel at higher RR. To see the velocity pattern in more details on can see a small recording area illustrated in figure 6.13. This figures shows clearly what we have discussed earlier. As expected, the velocity is highest at the surface of the wheel and decreases in the y-direction. One thing we can note at RR's of 100rpm, in the region of ($-25 < x < -40$,$-10 < y < 0$) the flow suddenly decelerates which is a consequence of the coherent stream created when the wheel were rotating at 100rpm. Also the liquid seems to stand still in some region specially for lower RR.

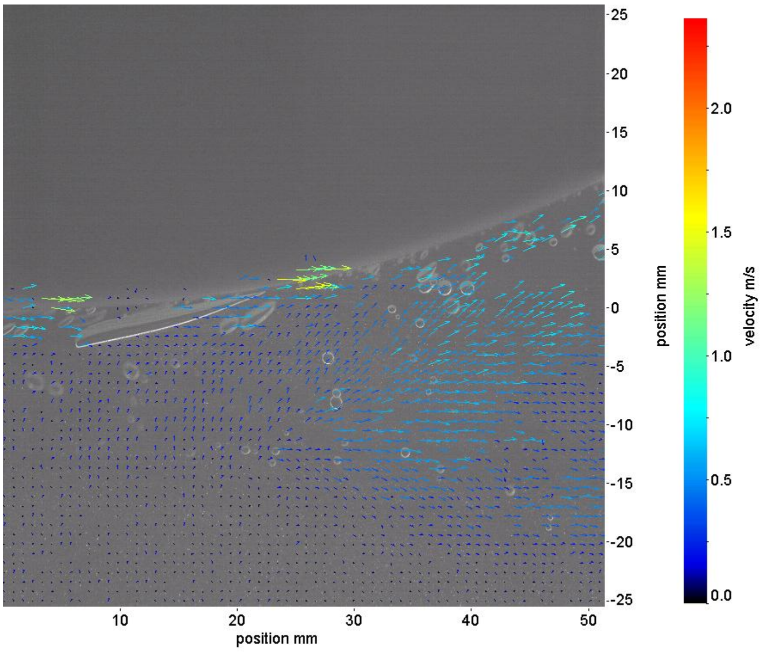

Figure 6.10: Vector field and raw image at time 3 ms

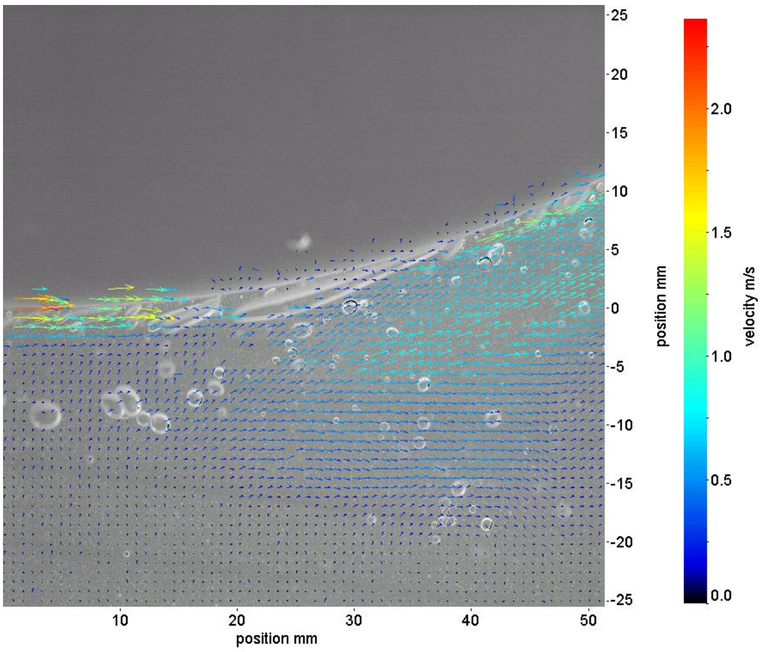

Figure 6.11: Vector field and raw image at time 156 ms

6.3.1 Large Field of View Camera

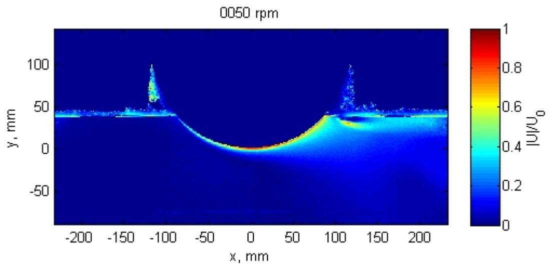

(a)

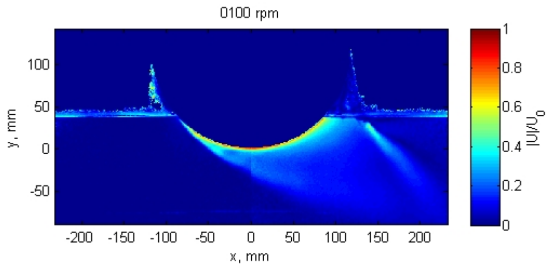

(b)

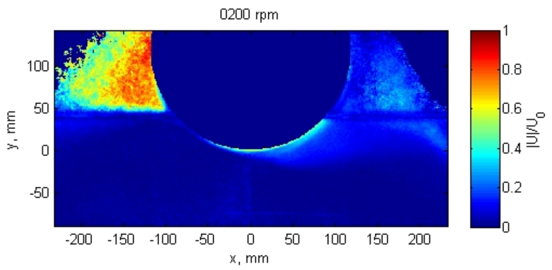

(c)

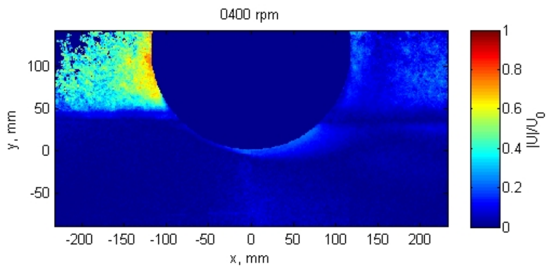

(d)

Figure 6.12: Mean field, large field,(a): 50 rpm, (b): 100 rpm ,(c): 200 rpm, (d): 400 rpm.

6.3.2 Small Field of View Camera

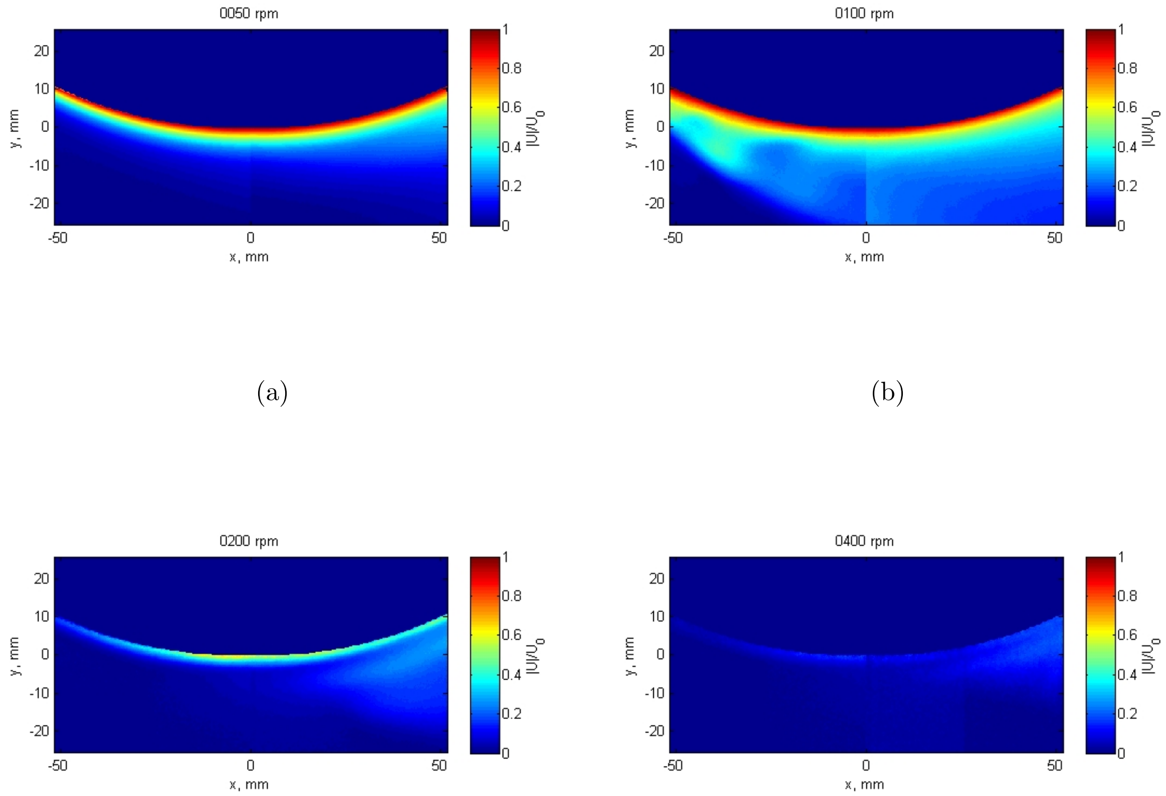

(a) (b) (c) (d)

Figure 6.13: Mean field, small field,(a): 50 rpm, (b): 100 rpm ,(c): 200 rpm, (d): 400 rpm.

6.4 Vector Fields as Velocity Fields

Figures 6.14 and figures 6.15 illustrates the mean fields of the velocity vectors. At RR's of 200rpm, the flow dominates around the wheel and the velocity profile look like ballistic motion. In fact due to that reason we have 1/3 of the wheel radius in the oil level and results for maximum velocities can be reached. In this configuration the maximum splash and hence the maximum lubrication of wheel components in the gear system can be reached. Basically everything discussed in previous sections can be interpreted here. We can also see some random velocity vectors above the surface as well as on the oil level, as a consequence of the chaotic flow occurring in these regions.

6.4.1 Large Field of View Camera

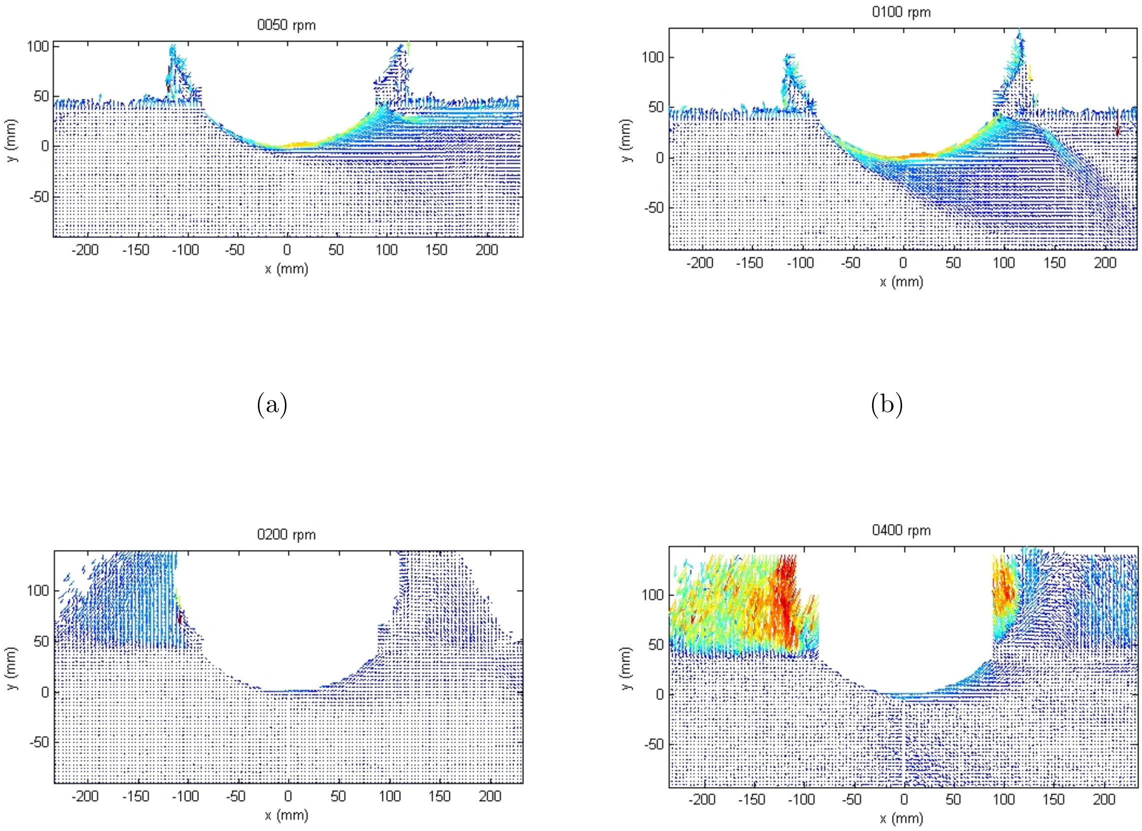

(a) (b) (c) (d)

Figure 6.14: Vector field, large field,(a): 50 rpm, (b): 100 rpm ,(c): 200 rpm, (d): 400 rpm.

6.4.2 Small Field of View Camera

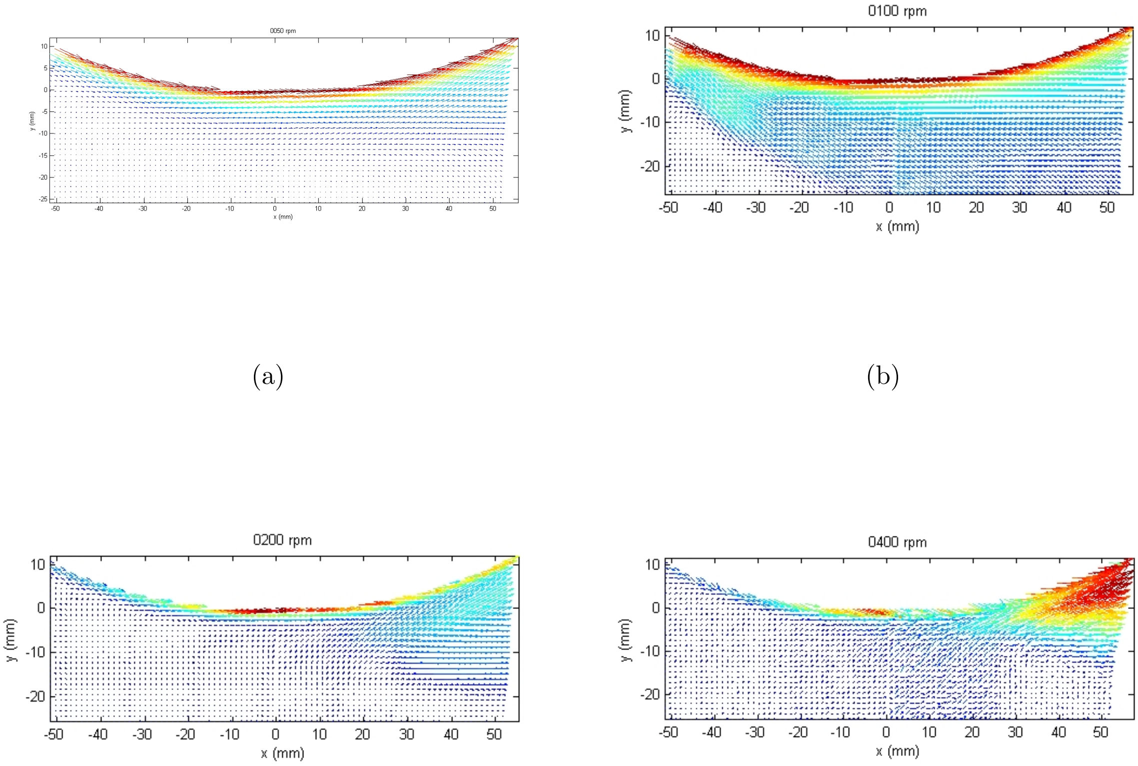

(a) (b)

(c) (d)

Figure 6.15: Vector field, small field,(a): 50 rpm, (b): 100 rpm ,(c): 200 rpm, (d): 400 rpm.

7 Results of PIV measurements for Spur Gear wheel

Raw PIV images in the recording area (large field view of camera) of reverse as well as forward rotational directions are shown in figures 7.1, 7.2, 7.3 and 7.4. Basically like for smooth gear wheel, the reverse direction generates more bubbles, oil drops and splash compared to the forward direction. We can see that for spur gear wheel, even at RR's of 50rpm, a small formation of stream creates, as the wheel starts to rotate in the backward direction only. In the forward direction, the earliest streams can be seen at RR's of 200rpm (see figures 7.3(c,d)). In fact above the wheel and in the end of each toot one small stream is formed which we could not see at all for the smooth wheel (not true in forward direction of spur gear). But in the reverse direction at RR's of 100rpm the flow around the spur gear wheel looks like the RR's at 200rpm for the smooth gear wheel, (see figure 7.1(b)and 6.1(c)). The teeth wheel seemed to generate more chaotic flow with splash and oil drops inside the modelled gearbox independent of rotational direction, which is naturally and also expected. By comparing the flow fields around the wheel for smooth and spur gears in the forward direction, one can immediately see there is no much difference of oil distribution around each wheel (see figures 7.3, 7.4, 6.4 and 6.5). Also during the experiments, we observed the flow pattern to be more “aggressive” in general and overall everywhere inside the modelled gearbox. Specially at RR's of 1200rpm, huge oil drops together with splash contaminated the gearbox window, which could cause optical refraction and disturbance for PIV measurements. In next section we will discuss more in detail the flow and bubble distribution between the teeth.

7.1 Raw PIV images of Large Field of View Camera

7.1.1 Reverse direction

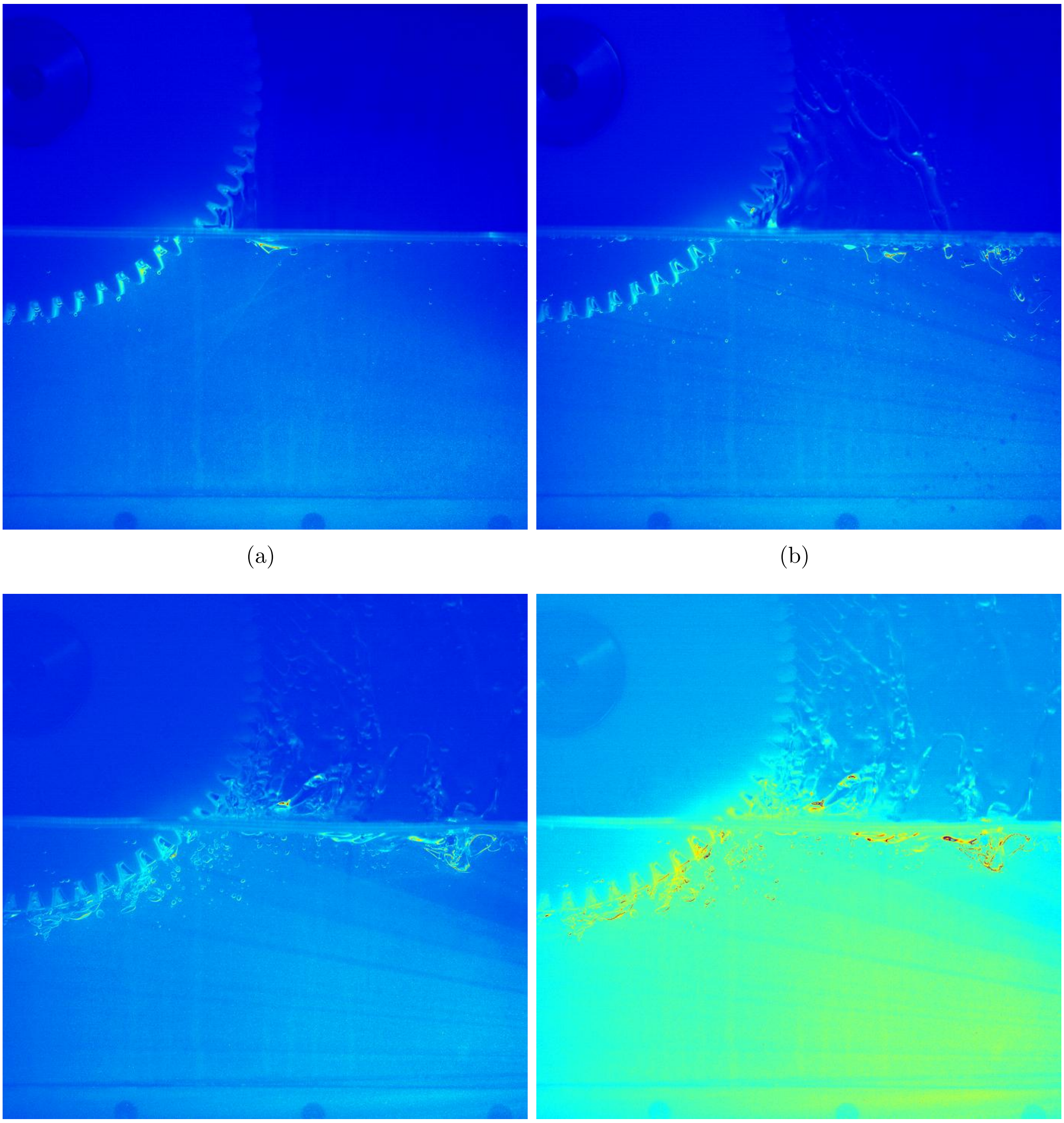

(a) (b) (c) (d)

Figure 7.1: (a): 50 rpm, (b): 100 rpm ,(c): 200 rpm, (d): 200 rpm at different brightness level.

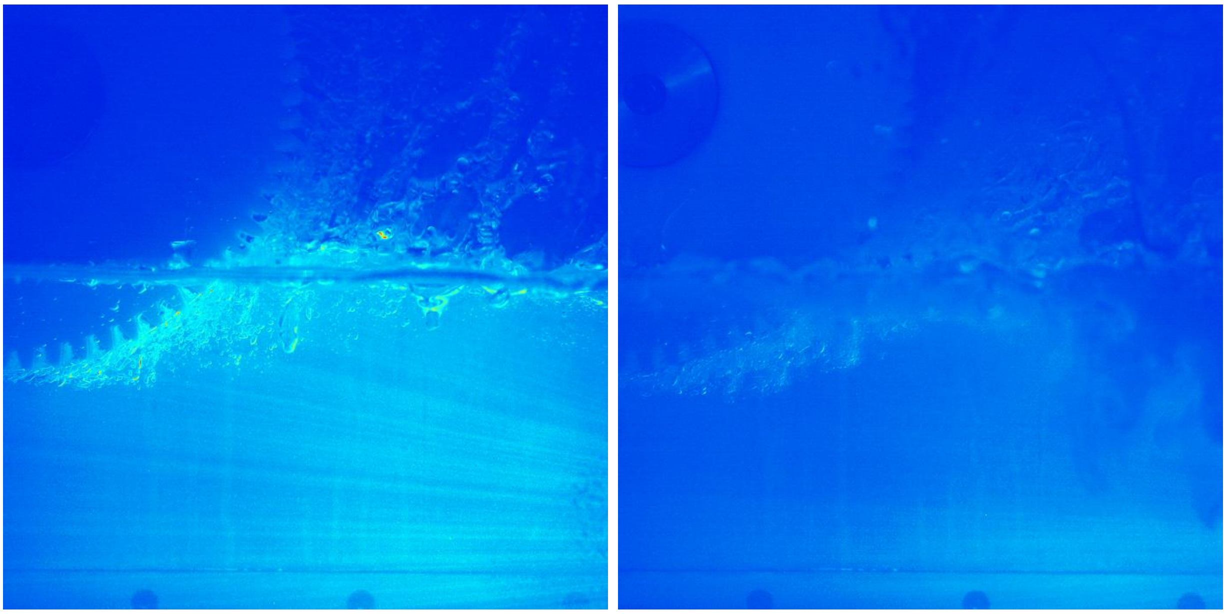

(a) (b)

Figure 7.2: (a): 400 rpm, (b): 1200 rpm.

7.1.2 Forward direction

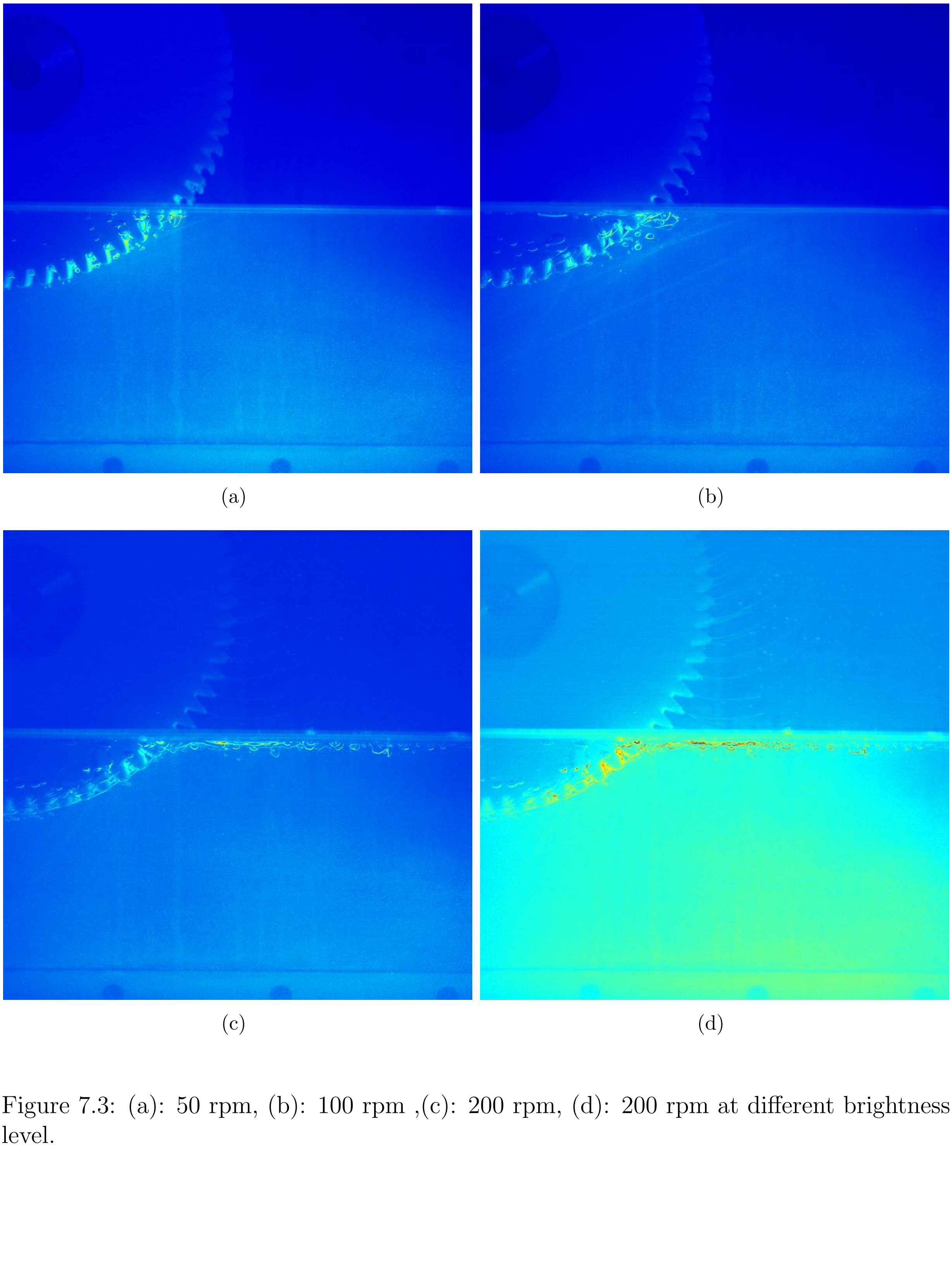

Figure 7.3: (a): 50 rpm, (b): 100 rpm ,(c): 200 rpm, (d): 200 rpm at different brightness level.

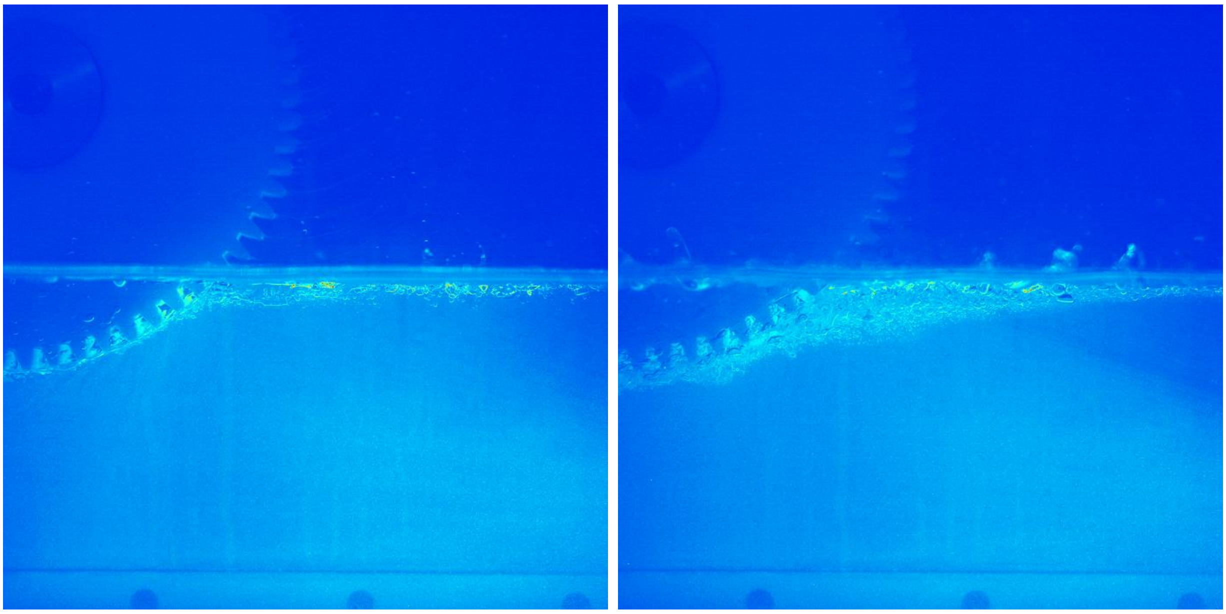

(a) (b)

Figure 7.4: (a): 400 rpm, (b): 1200 rpm.

7.2 PIV images of small Field of View Camera

As mentioned earlier, measurements in the smaller recording area was important in order to get some view of the flow between each tooth. This is illustrated by means of raw PIV images in both rotational direction in figures; 7.5, 7.6, 7.7, 7.8, 7.8, 7.9, 7.9, 7.10, 7.11, 7.12, 7.13 and 7.14. For every rotational direction and of every RR, images are extracted at four different time periods. At RR's of 50rpm, basically air bubbles fills up the half of the "space" between each tooth. From figures, we can see that the smallest bubbles simply move in between the tooth. Immediately when the wheel starts to rotate one large single bubble seems to be first created between the first and the second tooth (count from the left side of the wheel). As the gear wheel rotates, small bubbles will occupy the "space" between each tooth, but the single largest air bubble remains still during the rotation. This large air bubble continue to grow as illustrated in figures 7.6. At RR's of 200rpm, the air bubble completely fills up the space between each tooth, see figures 7.7. At this stage the flow pattern around the spur gear wheel looks almost like the flow pattern of the smooth gear wheel at RR's of 200rpm, see figures 6.6(b,c). At higher RR's than 200rpm, the bubble distribution around the spur gear wheel looks more or less like the flow distribution of the smooth gear wheel, see figures 6.6(d), 6.7, 7.8 and 7.9. As expected, the bubble boundary continue to grow even for the spur gear wheel. In forward direction, the same phenomena can be observed as for the reverse direction until 400rmp, but at RR's of 1200prm, we observed how the large bubble occupying the space between each tooth suddenly breaks up into smaller bubbles, see figures 7.14.

In the next section we will discuss the mean fields velocity profiles for different cases of RR's.

7.2.1 Reverse direction

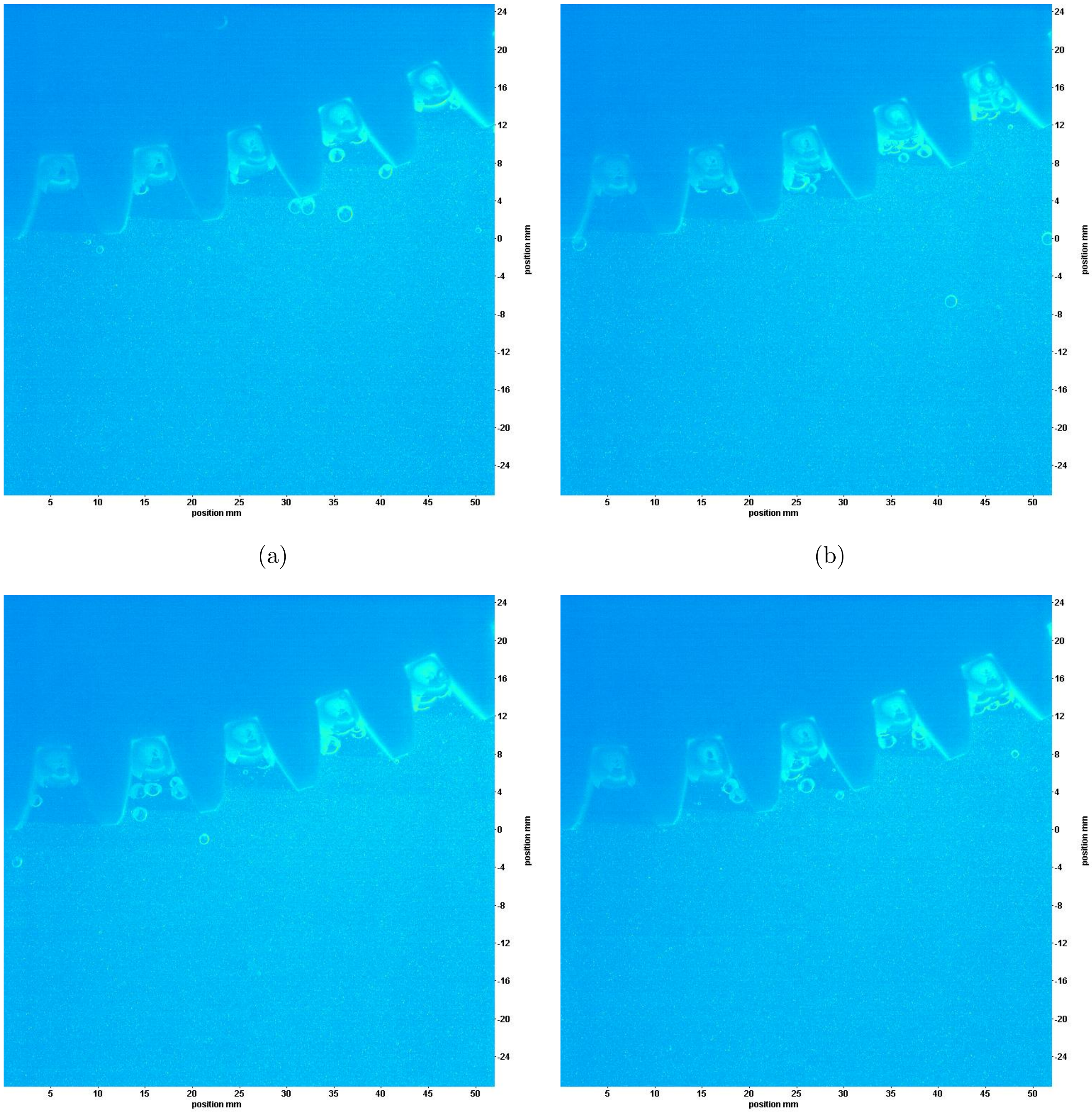

(a) (b) (c) (d)

Figure 7.5: 50 rpm at different time. (a): 12 ms, (b): 24 ms ,(c): 36 ms, (d): 48 ms.

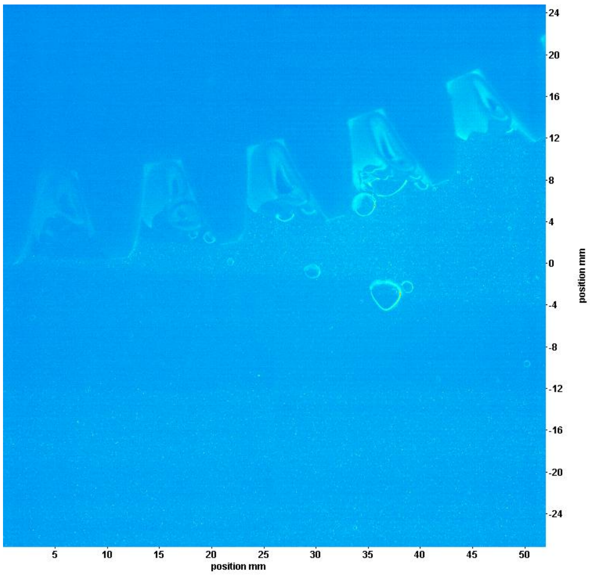

(a)

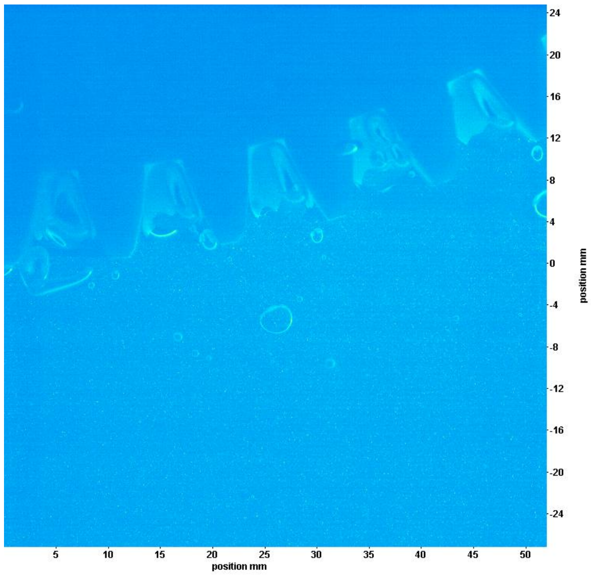

(b)

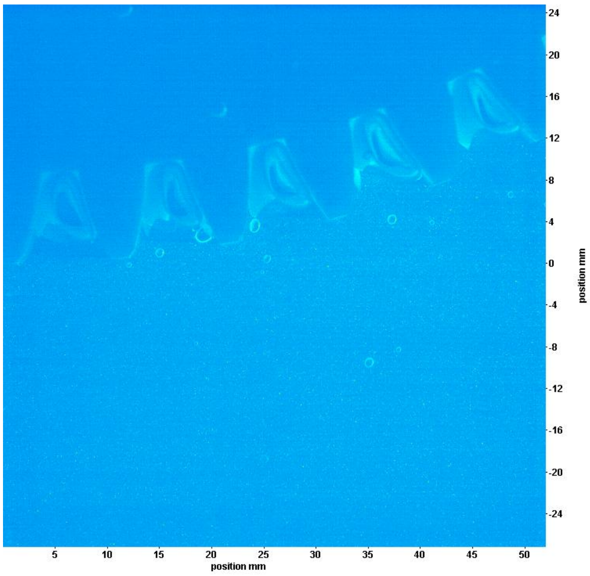

(c)

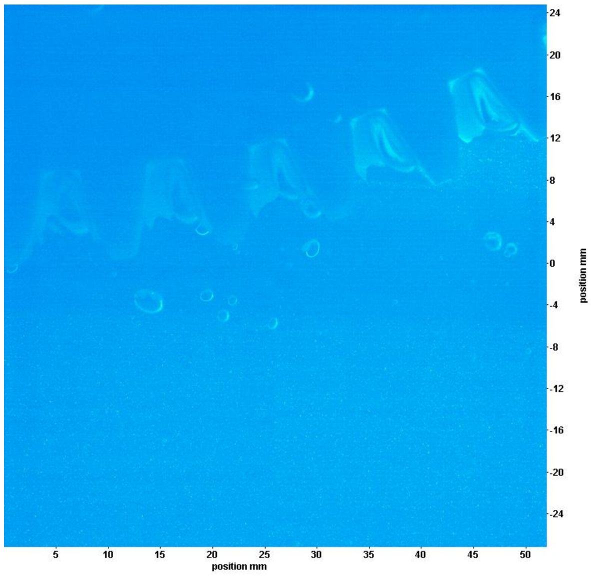

(d)

Figure 7.6: 100 rpm at different time. (a): 6 ms, (b): 12 ms ,(c): 24 ms, (d): 36 ms.

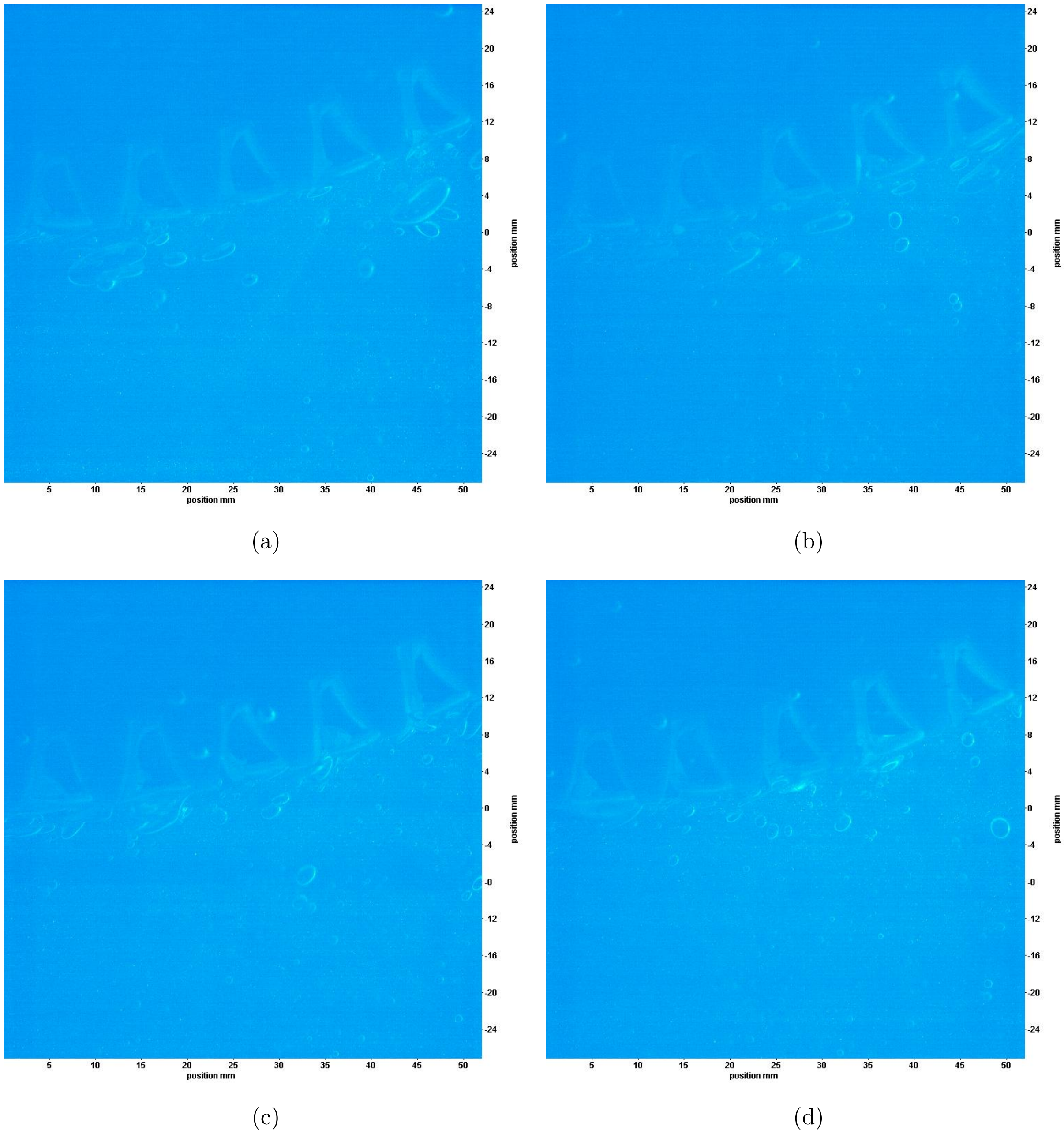

Figure 7.7: 200 rpm at different time. (a): 3 ms, (b): 6 ms ,(c): 9 ms, (d): 12 ms.

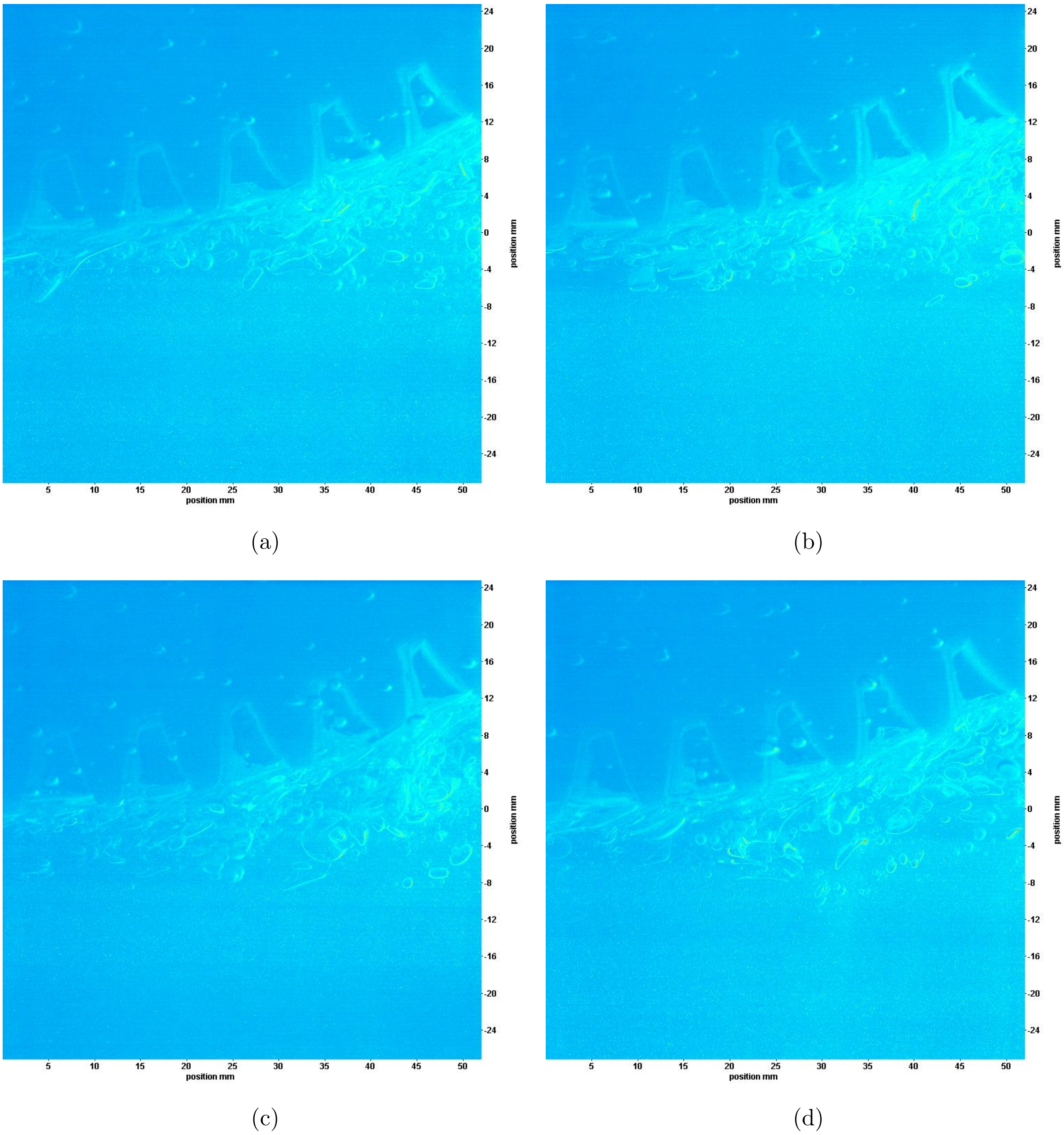

Figure 7.8: 400 rpm at different time. (a): 3 ms, (b): 6 ms ,(c): 9 ms, (d): 12 ms.

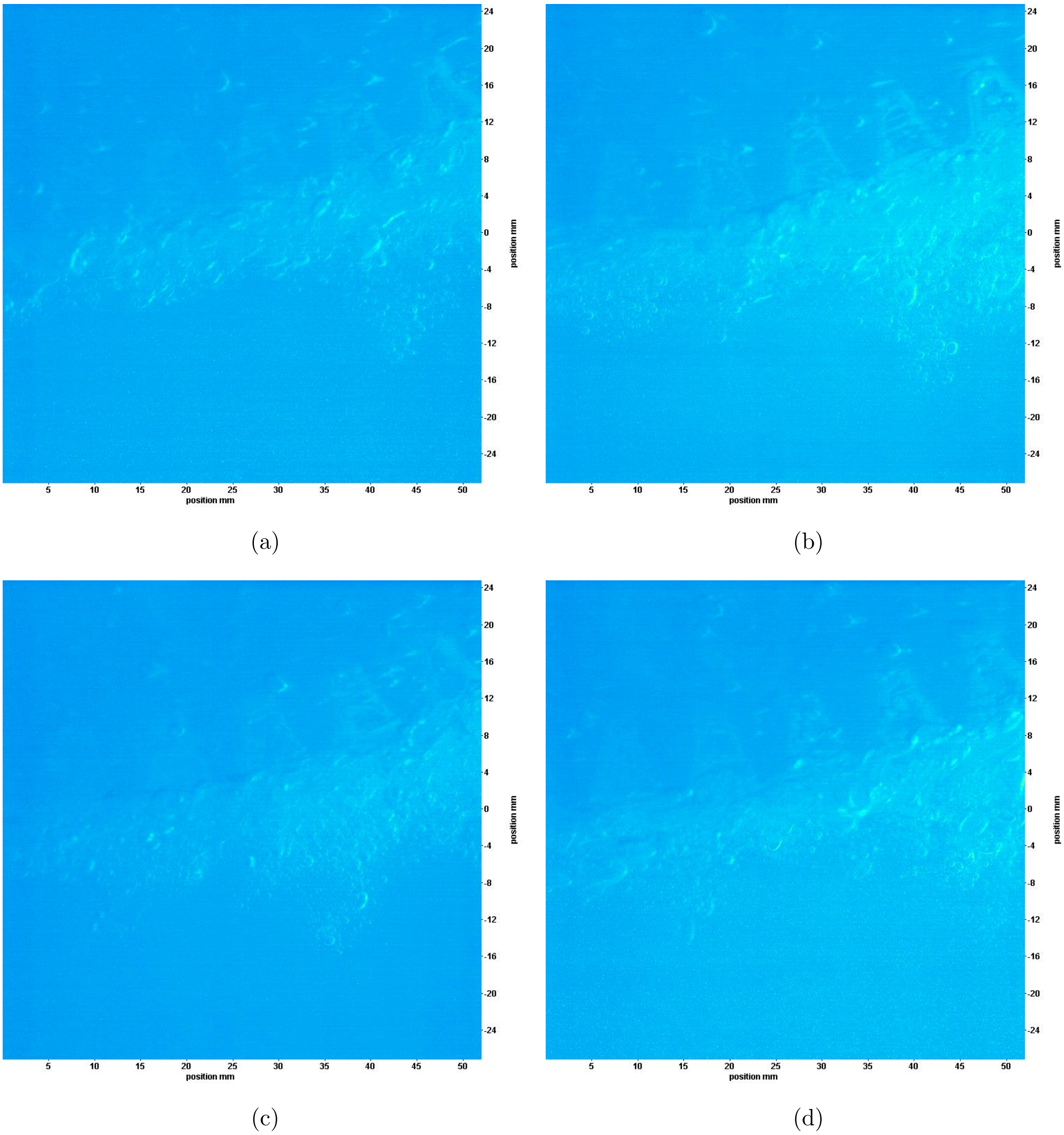

Figure 7.9: 1200 rpm at different time. (a): 3.3 ms, (b): 6.7 ms ,(c): 10 ms, (d): 13.2 ms.

7.2.2 Forward direction

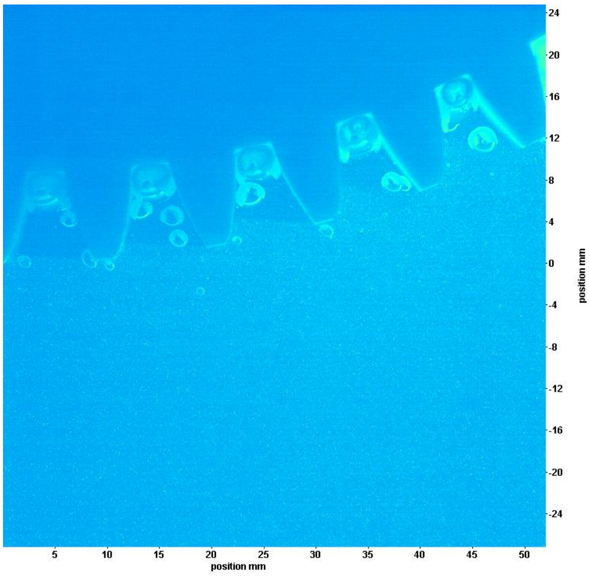

(a)

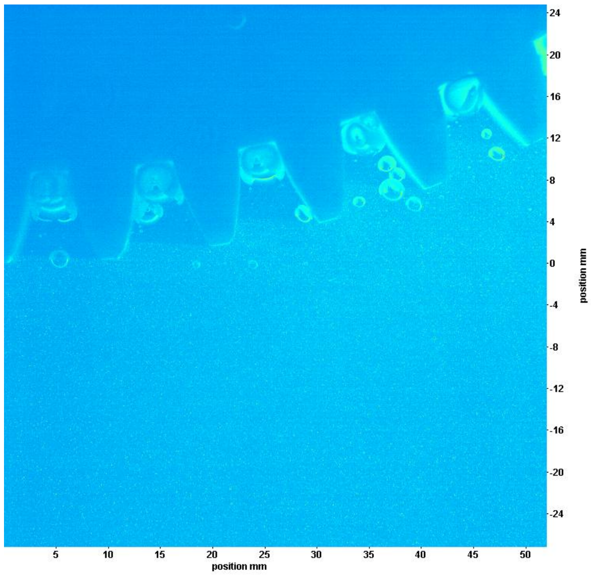

(b)

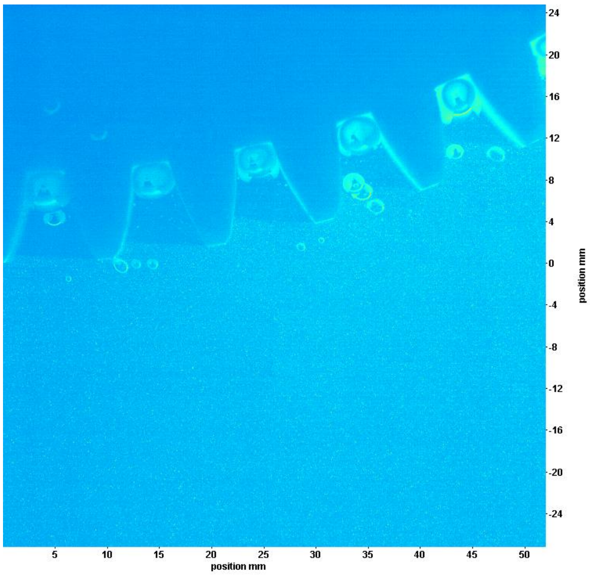

(c)

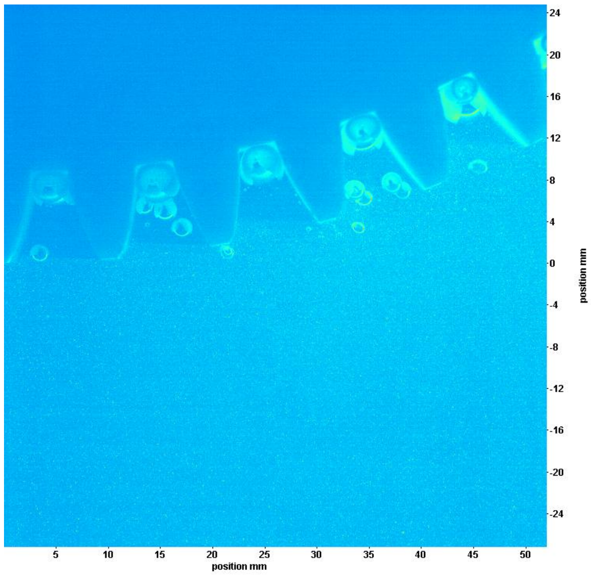

(d)

Figure 7.10: 50 rpm at different time. (a): 12 ms, (b): 24 ms ,(c): 36 ms, (d): 48 ms.

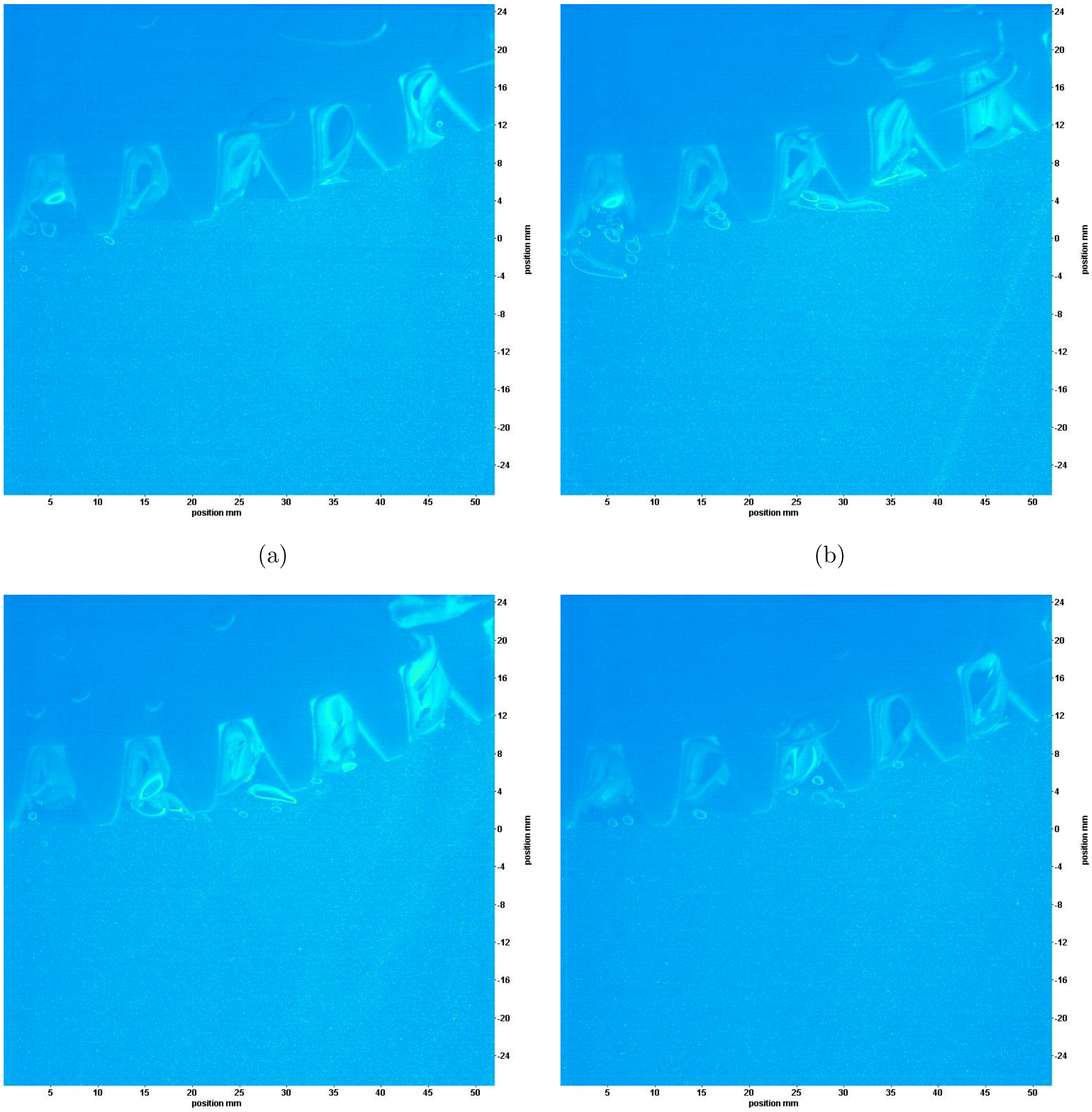

(a) (b) (c) (d)

Figure 7.11: 100 rpm at different time. (a): 6 ms, (b): 12 ms ,(c): 24 ms, (d): 36 ms.

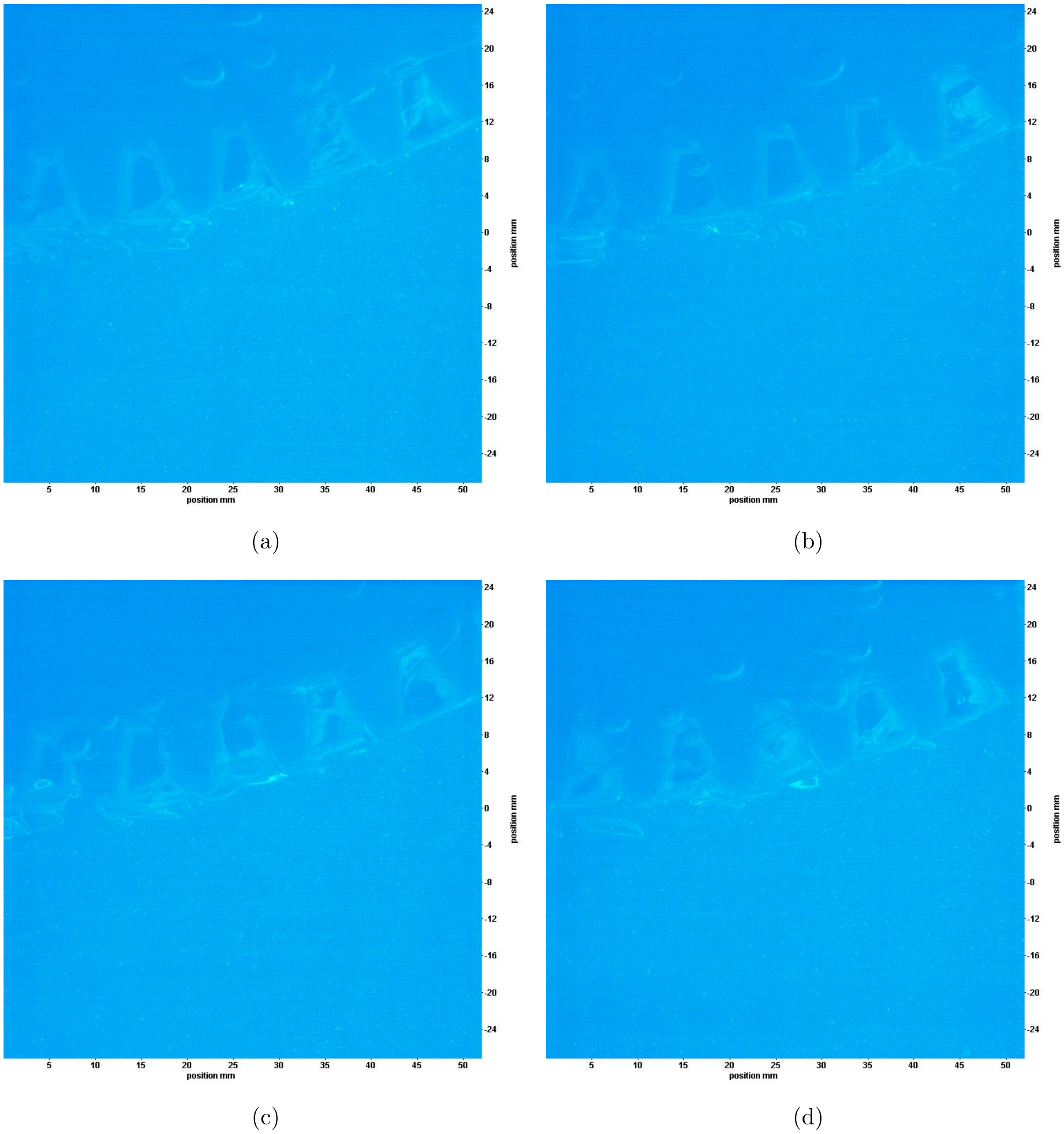

Figure 7.12: 200 rpm at different time. (a): 3 ms, (b): 6 ms ,(c): 9 ms, (d): 12 ms.

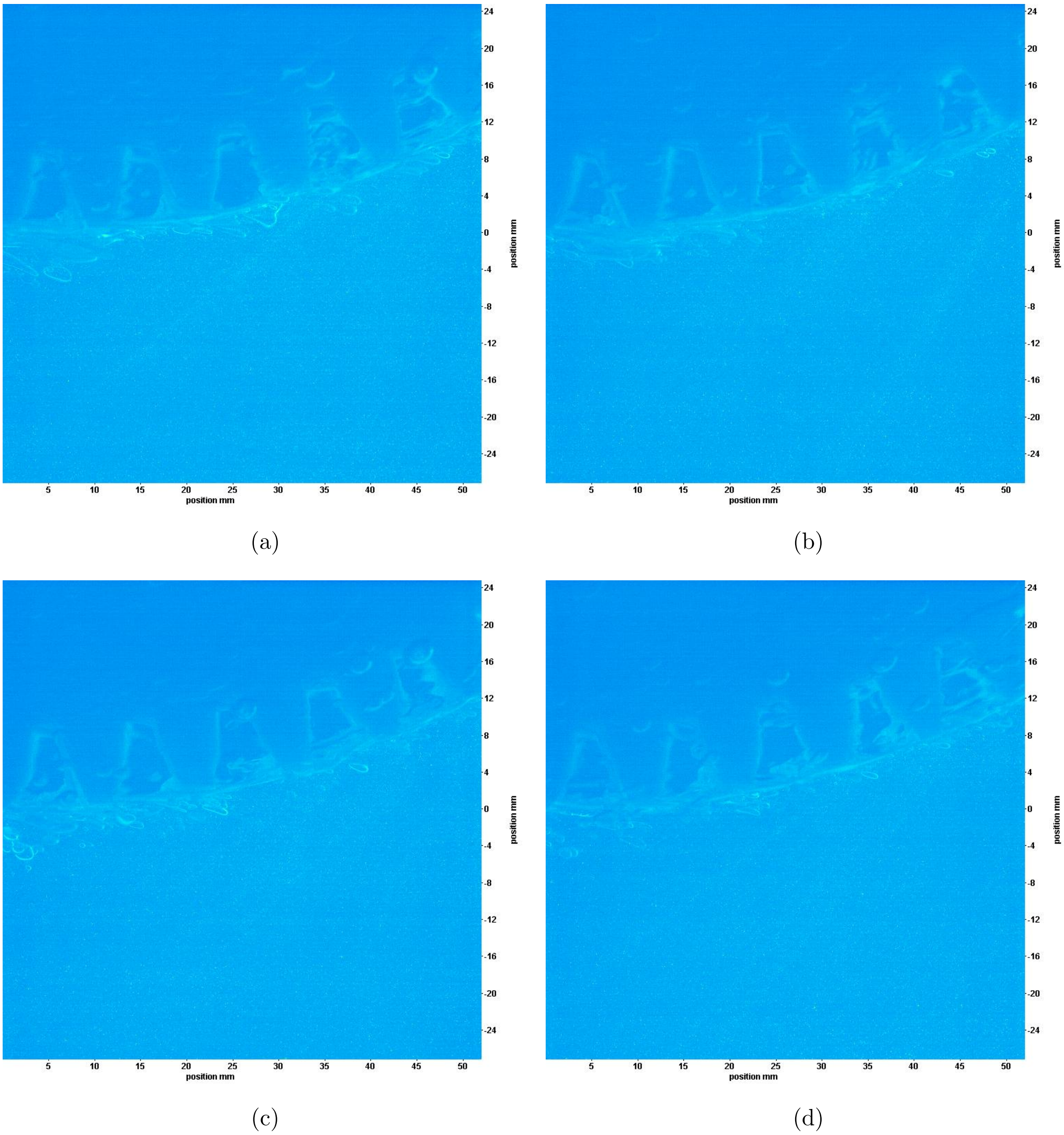

Figure 7.13: 400 rpm at different time. (a): 3 ms, (b): 6 ms ,(c): 9 ms, (d): 12 ms.

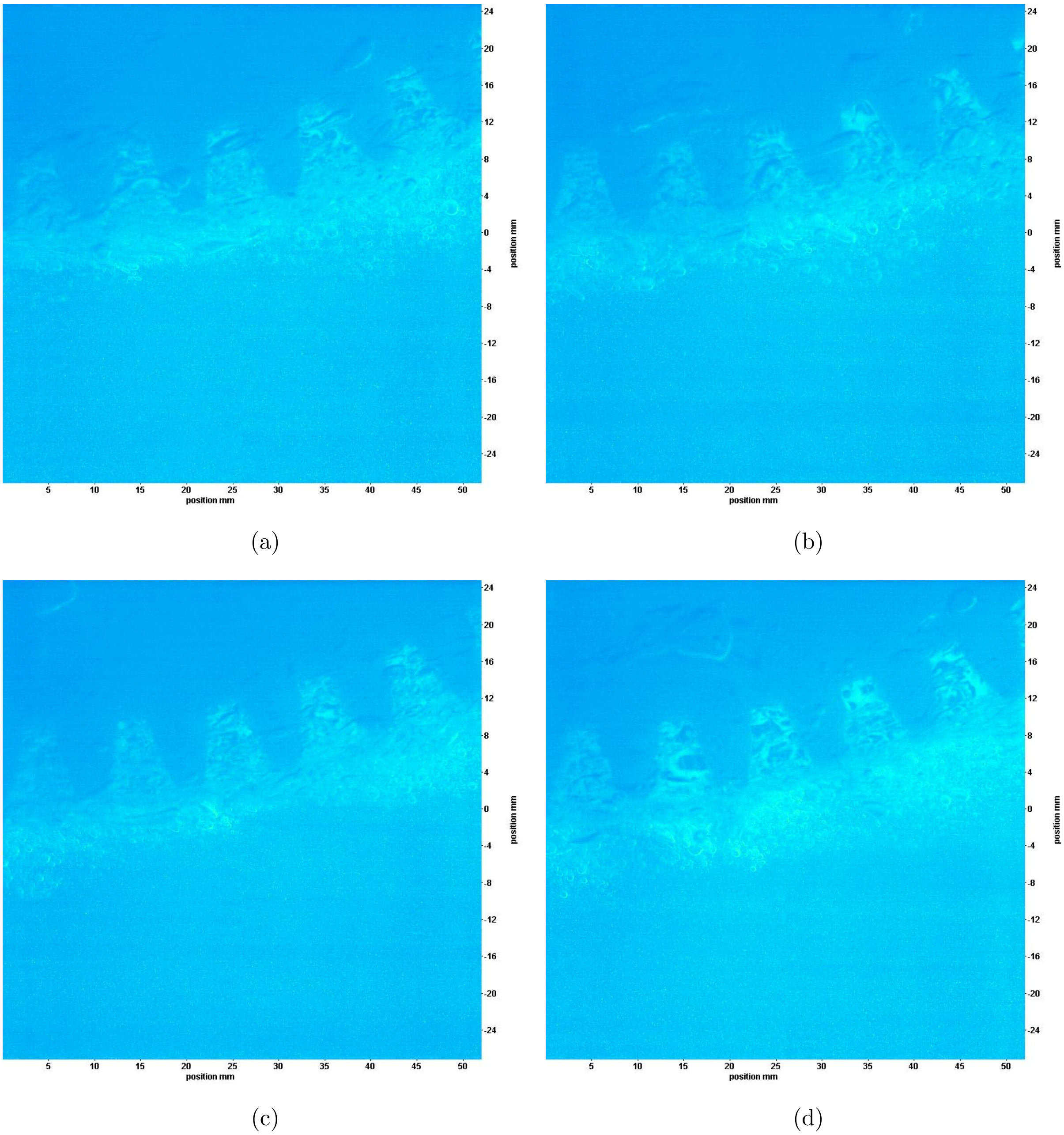

Figure 7.14: 1200 rpm at different time. (a): 3.3 ms, (b): 6.7 ms ,(c): 10 ms, (d): 13.2 ms.

7.3 Mean Field Velocity

In order to evaluate the mean fields, we use the same approach as for the smooth wheel. The velocity vectors was first averaged over the fields with respect to a certain number of points in the plane. And via a statistical method we remove the spurious vectors as well as too slow bubbles. To get the mean fields, a certain number (number of sample are dependent of the cases) of measurement sample was averaged. The results are illustrated in figures 7.15 and 7.16. In this case we also mask the wheel and the spur teeth. At low RR's, the flow is laminar (figure 7.15(a)). As expected, the maximum velocity can be observed at the teeth, specially at the right hand side of the wheel where the velocity reaches its maximum level and decelerates in the negative y-direction, (compare with the smooth gear in figure 6.12(a)). We can note that the laminar boundary layer is already large at RR's of $50rpm$ and we can see some kind of transition. The teeth of spur gear seems to promote turbulence which is illustrated in figure 7.15(b), where the flow is fully turbulent already at $100rpm$, (compare to the smooth wheel which is fully turbulent at $200rpm$). Above RR's of $200rpm$ the flow passes, from to be dominated on the right hand side of wheel and below the oil surface, to be dominated both in left hand side and above the oil surface. At rotational speed of $200rpm$ (figure 7.15(c)), one can also see the individual streams that forms from each tooth. And at RR's of $400rpm$ the wheel velocity is so fast that a jet is created, and is dominated on the right hand side of the wheel. At higher RR's, it was not possible to get accurate results, partly because it is too much optical refraction and disturbance creating bubbles, huge oil drops and splash besides the contamination of the gearbox window, which complicates the registration of the PIV displacement for each individual tracer particles, in every PIV frame. In particular at RR's of $1200rpm$, the numbers of measurements samples was also limited due to the problem we described above, because at $1200rpm$ we needed to perform very quick measurements before the tracer particle images were blocked by bubbles. However, to see more in detail below the wheel, measurement was done in a smaller recording area illustrated in figures . As seen, the flow field velocity reaches its maximum between the teeth. This can be explained by the discussion in the previous section. Until $100rpm$, it is possible for laser sheet to penetrate into bubbles and light up most of the space between every tooth. The fact that when air bubbles completely occupy the space between each tooth for higher RR, the spur wheel "behaves" and looks like the smooth gear wheel which means that the bubbles between the teeth rotates in the same velocity as the wheel. Because they don't move at all, they obtain the same velocity as the wheel. But why can we not see the maximum velocity between the teeth at higher RR's? The answer is simply that the bubbles occupie the space between the teeth and make the PIV measurements impossible.

7.3.1 Large Field of View Camera

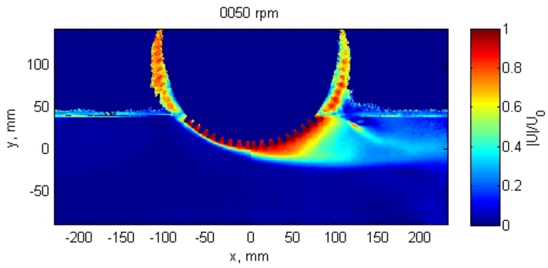

(a)

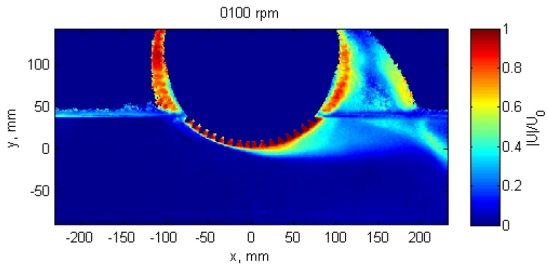

(b)

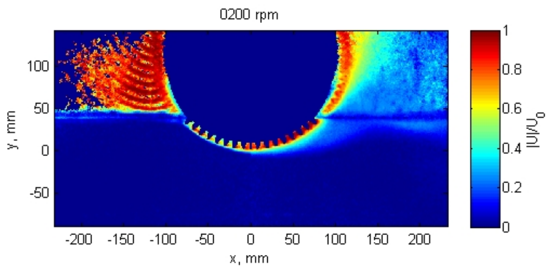

(c)

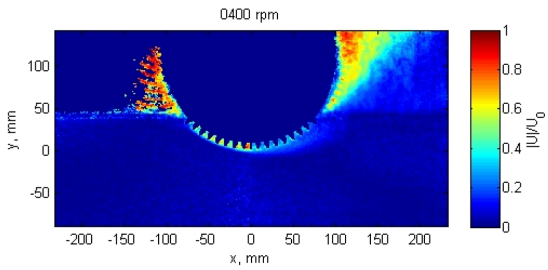

(d)

Figure 7.15:

7.3.2 Small Field of View Camera

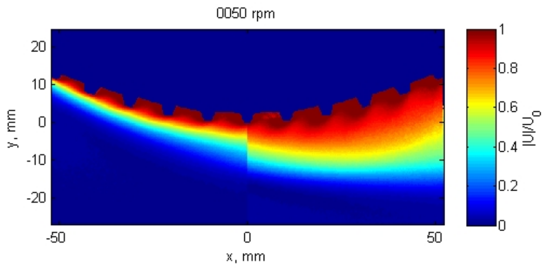

(a)

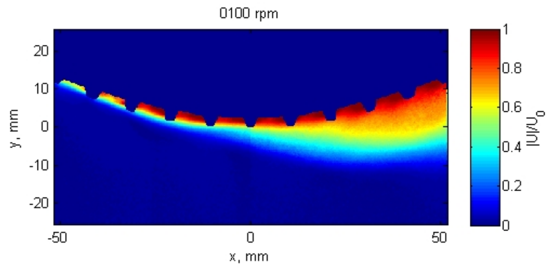

(b)

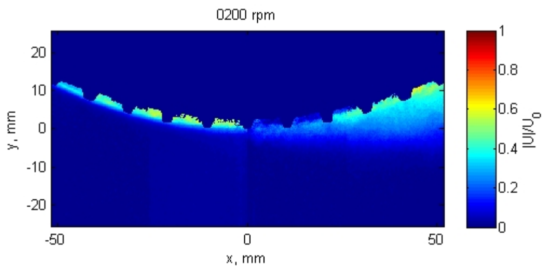

(c)

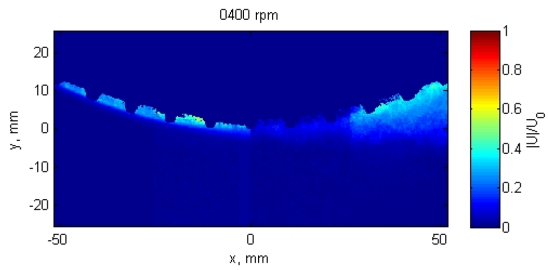

(d)

Figure 7.16:

7.4 Vector Fields as Velocity Fields

The results of velocity vectors are shown in figures 7.17 and 7.18. Compared to the smooth gear wheel, the flow pattern looks more ballistic, specifically at $100rpm$. Basically same discussions that we had in previous section can be applied here as well. The velocity vectors are colored in the same color map as for the mean velocity field. As one can see the velocity differences varus in different regions around the wheel. For low RR's, the flow moves very fast close to wheel and decelerates far from the wheel. Above the oil surface, around the wheel the flow motion is dominated by splash and oil drops which is shown as random velocity vectors.

In the next section we will compare the results of mean velocities and turbulence intensity in cylindrical coordinates in 5 different positions for both modelled smooth and spur gear wheel.

7.4.1 Large Field of View Camera

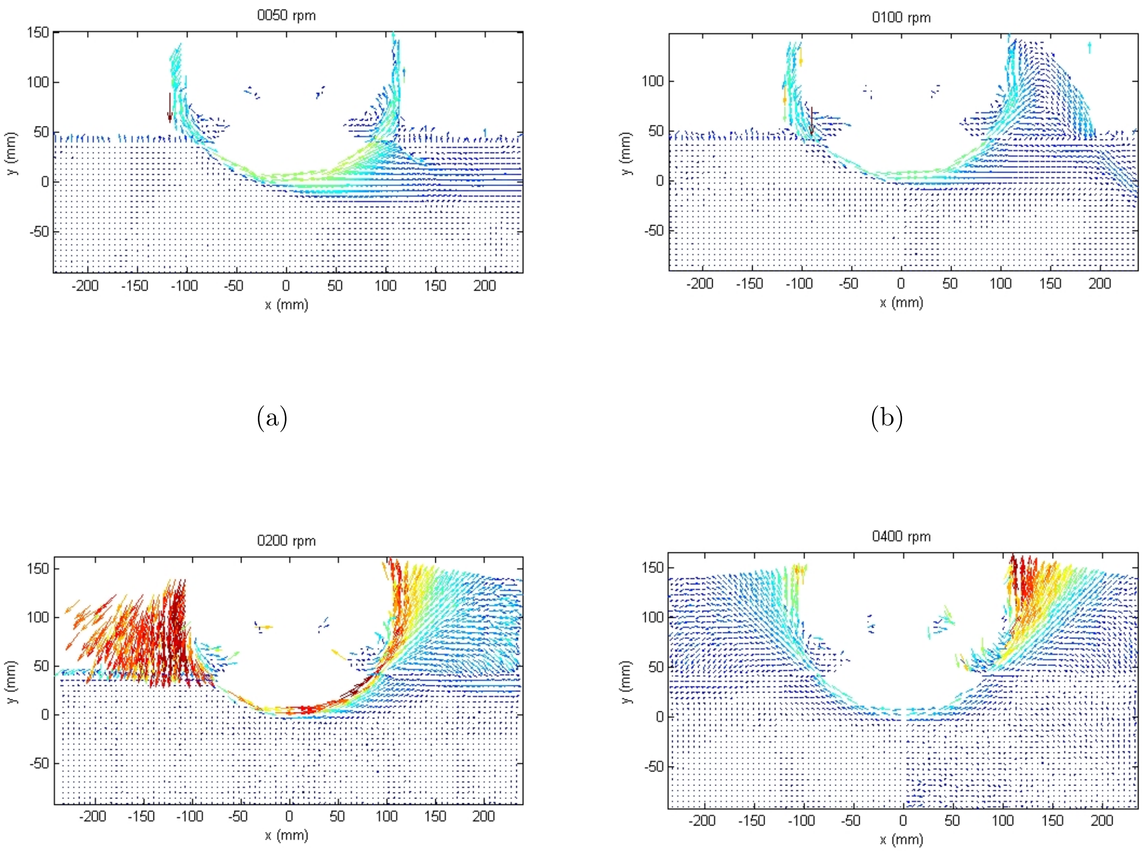

(a) (b) (c) (d)

Figure 7.17:

7.4.2 Small Field of View Camera

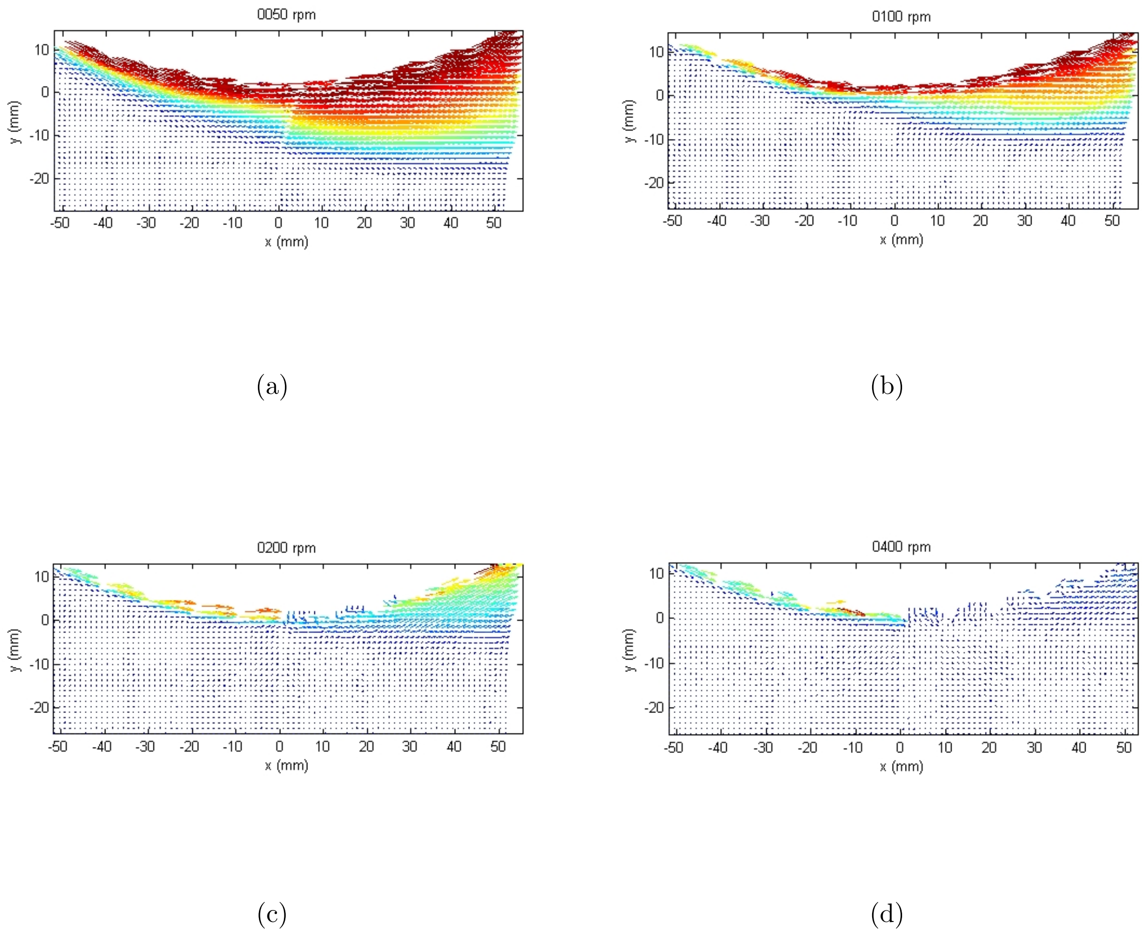

(a) (b) (c) (d)

Figure 7.18:

8 Boundary layer profiles

In order to further analyze the results for smooth and spur gear wheel, we compared the mean velocity and turbulence intensity for a small recording area in five different regions. Figure 8.1 show the positions of these regions. The first line represents the first pictures in figure 8.2(a,b,c,d) and the fifth line represent the fifth pictures in figure 8.2(a,b,c,d). The velocity profiles are evaluated in a cylindrical coordinate system, where R_0 represent the radius of the wheel. At $50rpm$ for the smooth wheel, the flow is laminar, and this laminar boundary layer continue to grow around the wheel. As the wheel rotate faster ($100rpm$), the boundary layer continue to grow and we see more liquid motion even far from the wheel. At this stage the flow is fully laminar. As the wheel rotates faster, we can see some transition and at $200rpm$ the liquid flow around the wheel is fully turbulent. The maximum scaled velocity ($|U|/U_0$) profile reach up to 0.5. At RR of 400 we can see some kind of fluctuation in the velocity in some regions, which can be a consequence of too low numbers of measurements samples. In fact, it was not possible to increase the sample rate. Too many bubbles disturbs the liquid. However, at $400rpm$, the liquid velocity continue to decrease which is caused by the creation of large bubbles and they moves very slow compared to the liquid. Of course at this stage, this bubbles are contaminated with tracer particles, so it might be possible that we measure on the bubbles as well. In some regions, same velocity profile can be seen as for the spur gear wheel. But at $50rpm$, in region ($x \sim 0$, $R \sim R_0$) suddenly the velocity reaches the maximum level and decreases linearly close to the wheel until $R \sim 15\,mm$. Suddenly we see no flow motion at all far from the wheel. And In some regions the velocity profile seems to decrease linearly proportional to R (see last figure in 8.2(a)). One thing we can notice is the transition to turbulence flow which starts much earlier, i.e., at 100 for spur gear. At this RR, the maximum velocity scale are below 0.6 in some regions, except at the right hand side of the wheel. Due to that, a coherent stream is always present in those regions and the liquid velocity is always highest there, independently of the RR and choice of the wheel (see fifth figure in 8.2(a,b,c,d) of all RR's).

The turbulence intensity of the flow around the wheel are evaluated for smooth as well as for spur gear wheel in same regions as shown in figure 8.1. The turbulence intensity can be computed from

$$I = \frac{U_{\text{rms}}}{U_0} \qquad U_0 = \frac{\omega}{60}\pi D \tag{8.1}$$

where U_{rms} represent the root mean square of velocity fluctuations and reads,

$$U_{\text{rms}} = \sqrt{\overline{u_x'^2} + \overline{u_y'^2}}. \tag{8.2}$$

As can be seen from figure 8.3, the turbulence intensity various as lowest 1% and as maximum up to 35% in different flow regions around the wheel. In most of the regions above $100rpm$, where the flow is fully turbulent the intensity is highest near the moving wall (wheel) and is then decaying. This was expected since the stresses and fluctuations are largest near the wall and it is in that region where most of the dissipation of the kinetic energy is taking place and naturally most of the turbulence is produced. The very smallest energy scales (Kolmogorov scales) of motion is in this case located in the moving wall region and it is here the dissipation occurs. The dissipation takes out the kinetic energy from the turbulence and transfers it further on to the internal energy. However at RR of 50 the turbulence intensity is quite low for smooth wheel. For spur gear, we can already see the transition from laminar to turbulence in some regions. The largest difference can be observe ia located at the right hand side of the wheel. As RR (100) increase, the flow gets dominated by the turbulence. At this stage the turbulent intensity is quite high $\sim 20\,\%$, but for smooth wheel, we can see an increase in intensity in some regions. At most, in the right hand side of the wheel (see first and second figures in figure 8.3(b). In this regions turbulence is quite uniform distributed up to $R \sim 20$. Above $100rpm$ the intensity increases very quickly, specially near the moving wall. For smooth gear wheel, the intensity is almost 35% in some regions, specially in the right hand side of the wheel. At $400rpm$, basically the intensity profile for both smooth and spur gear wheels agrees with each other in all regions. The explanation to this is that all the flow profiles at this stage are almost similar, which were showed and discussed in section 6, and in section7.

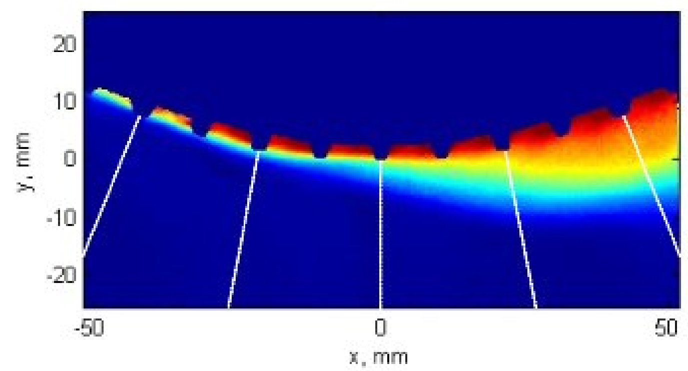

Figure 8.1: Position of boundary layer profile showing for small field of view.

8.1 Mean Velocity

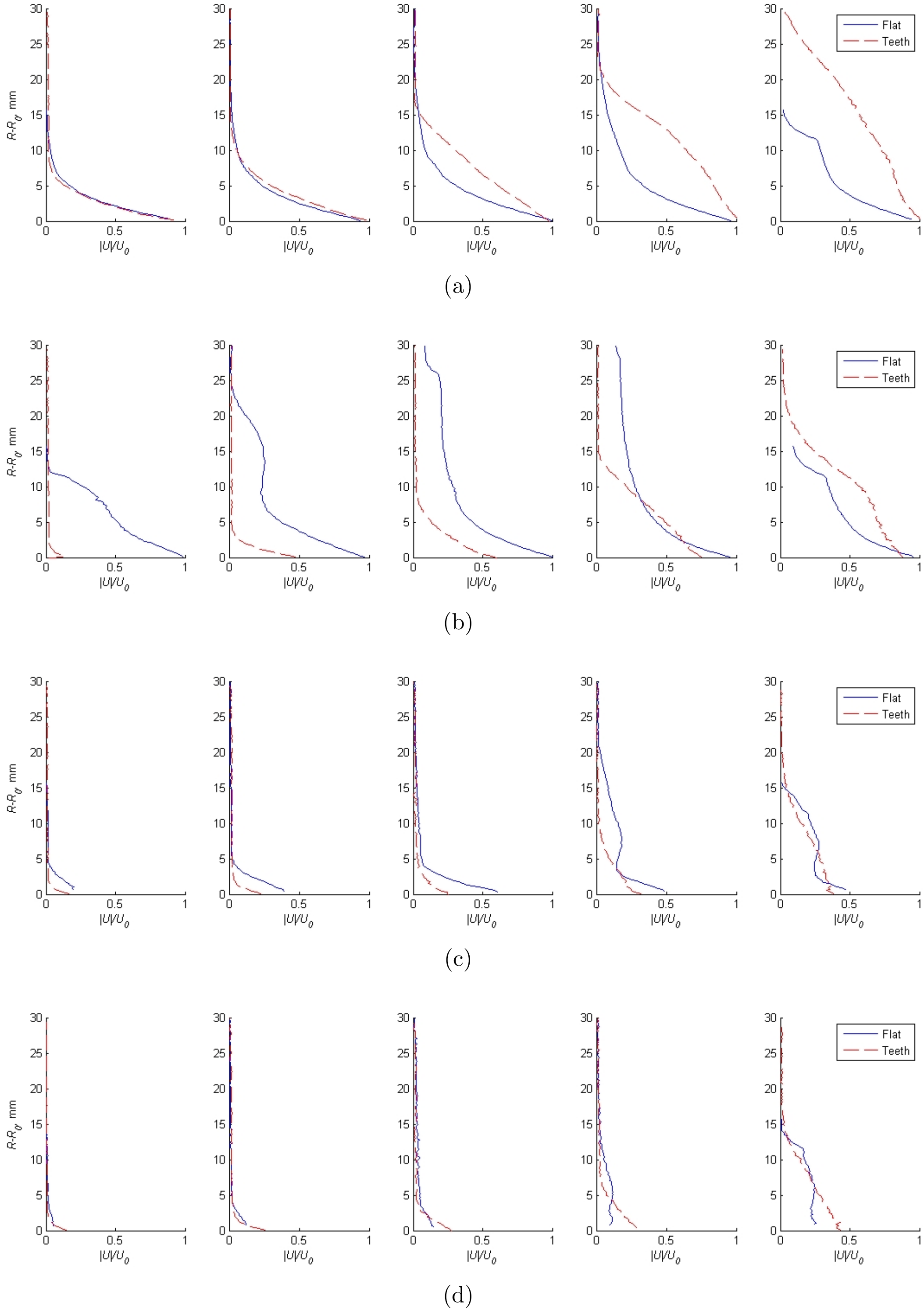

Figure 8.2: Boundary layer profiles of mean velocity at five different regions in small recording area for smooth and spur gear wheel. (a): 50 rpm, (b): 100 rpm ,(c): 200 rpm, (d): 400 rpm.

8.2 Rms Velocity

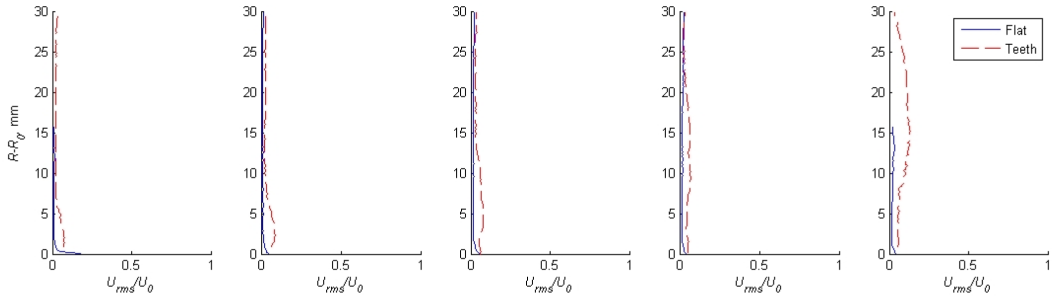

(a)

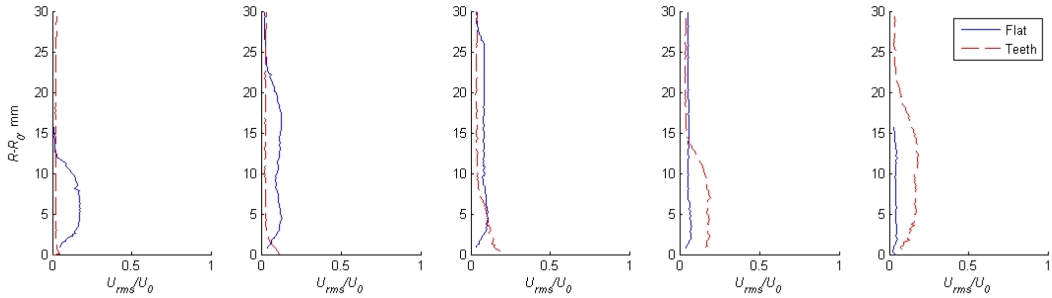

(b)

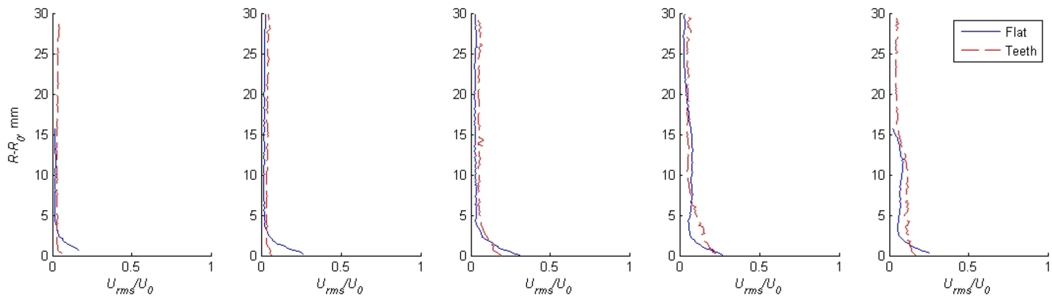

(c)

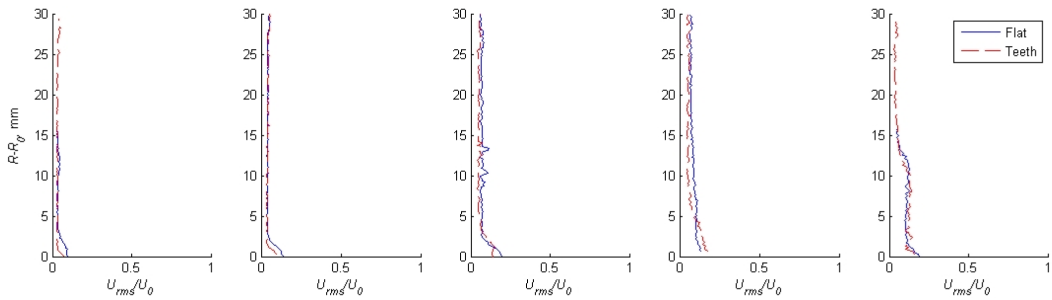

(d)

Figure 8.3: Boundary layer profiles of turbulent intensity (RMS) at five different regions in small recording area for smooth and spur gear wheel. (a): 50 rpm, (b): 100 rpm ,(c): 200 rpm, (d): 400 rpm.

9 Conclusions

Laser-Induced Fluoresce (LIF) combined with Particle Image Velocimetry (PIV) measurements were successfully performed around a modelled single rotating wheel within a modelled SAAB gearbox. Two-component velocity measurements were performed with rotation rates up to 400rpm in both forward and reverse direction. The measurements were performed for the modelled smooth and spur gear wheel, (in some cases were rotation rates up to 1200rpm possible to perform, i.e., forward direction). In this project we faced many problems and difficulties, for example finding the transparent oil, which was very important in PIV measurements. Initially when we started this project, we were only told to perform PIV measurements for a modelled gearbox. Soon we realized that the flow around the wheel both below and above the oil level was a very complex two-phase flow with splash. And besides that, contamination of the gearbox window made the PIV measurements even more difficult. Fortunately we solved most of the problems. Mean field as well as turbulence intensity could be extracted from the measurements, which showed the variation of velocity and turbulence close to the moving wheel. There is a clear difference in flow patterns between this two wheels, specially at rotation rates below 100rpm. At rotation rates above 200rpm, the flow profile seems to be almost identical for both the wheels. Also with increased wheel rotation speed the flow induced by the wheel in the oil become more and more confined to the region very close to the wheel since inertial forces are getting larger and more dominating over the viscous forces. But above the oil level the amount of oil splashed by the wheel is increasing with the increased rotation rate.

10 Recommendations

For further investigations for future work we recommend to perform the same PIV technique, i.e., Laser-Induced Fluorescence combined with PIV and modify the modelled gear box, e.g., a gearbox completely made in plexiglas and in a smaller dimension. This could reduce the optical disturbance even more. In order to measure the flow in details between each tooth, one can try to locate the laser beam from the bottom of the gearbox, if the bottom part of the gearbox is made in a transparent material. In order to further improve presision for the velocity of continuous-phase at high rotation rates it is necessary to first mask the disperse-phase (bubbles) and exclude it prior the cross-correlation evaluation. It is also of interest to obtain quantitative information about the disperse phase. To do so, one need to identify and track by using PTV every single bubble of all the different kinds of shapes and sizes that exists in the flow. At this moment it requires a very advanced program in order to be able to perform this. At the moment no program, as far as we know can track bubble shapes like hydrofoils of various shapes. Also the local as well as the global void fraction and bubble size distribution can be determined, partly because this information is very important when modelling the flow in multiphase CFD. For future work one can also investigate:

- Perform PIV in stereo setup in order to obtain three components of velocity.
- Perform measurements in different plains.
- Obtain more detailed information of one of the cases, we recommend $200rpm$ e.g. at several different planes.
- Perform measurement with several interacting wheels, if possible.
- Change the wheel dimension, if possible to a smaller diameter.

References

[1] Viewed 04 May, 2010, http://www.olympusmicro.com/.

[2] Viewed 12 May, 2010, http://en.wikipedia.org/wiki/Gear.

[3] Flowmap. Particle Image Velocimetry instrumentation. 5th ed., August 2000, Skovlunde, Denmark, 2000.

[4] Product-manual for davis 7.2, 2007.

[5] R. J. Adrian. Twenty years of particle image velocimetry. *12th International Symposium on Applications of Laser Techniques to Fluid Mechanics*, 2004.

[6] Yerbol K. Akmetbekov, Sergey V. Alekseenko, Vladimir M. Dulin, Dmitriy M. Markovich, and Konstantin S. Pervunin. Planar fluorescence for round bubble imaging and its application for the study of an axisymmertric two-phase jet. *Experiments in Fluids*, 2009.

[7] B. Andersson, R. Andersson, L. Hakansson, M. Mortensen, R. Sudiyo, and B. Van Wachem. *Computational Fluid Dynamics for Chemical Engineers Fourth Edition.* March 2008.

[8] C. Bongiovanni, J. Ph Chevaillier, and J. Fabre. Sizing of bubbles by incoherent imaging: defocus bias. *Experiments in Fluids*, 1997.

[9] D. Bröder and M. Sommerfeld. An advanced LIF-PIV system for analusing the hydrodynamics in a laboratory bubble column at higher void fractins. *Experiments in Fluids*, 33:826–837, 2002.

[10] C. Crowe, M. Sommerfeld, and Y. Tusji. *Multiphase Flows with droplets and particles.* CRC Press LLC, 1998.

[11] Niels G. Deen, Björn H. Hjertager, and Tron Solberg. Comparison of piv and lda measurement methods applied to the gas-liquid flow in a bubble column. *10th Int. Symp. on Appl. of Laser Techniques to Fluid Mech., Lisbon, Portugal, July 10-13*, 2000.

[12] S. Dehaeck, JPAJ. van Beeck, and MI. Riethmuller. Extended glare points velocimetry and sizing for bubbly flows. *Experiments in Fluids*, 39:407–419, 2005.

[13] Blanchat T.K. Seeley Jr. C.H. Hassan, Y.A. and R.E. Canaan. Simultaneous velocity measurements of both components of a two-phase flow using particle image velocimetry. *Int. J. Multiphase Flow*, 18:371–395, 1992.

[14] M. Honkanen. Turbulent multiphase flow measurements with digital particle image velocimetry: Application to bubbly flows. Master of science thesis, Tampere University of Technology, 2002.

[15] M. Honkanen, H. Eloranta, and P. Saarenrinne. Ddigital imaging measurement of dense multiphase flows in industrial processes. *Flow Measurement and Instrumentation*, 2009.

[16] M. Honkanen and K. Marjanen. Analysis of the overlapping images of irregularity-shaped particles, bubbles and dropplets. *International Conference on Multiphase Flow, Germany 9-13 July*, 2007.

[17] L. Li, H. K. Versteeg, G. K. Hargrave, T. Potter, and C. Halse. Numerical Investigation on Fluid Flow of Gear Lubrication. *SAE international*, 2008.

[18] Reese J. Hong T. Lin, T.-J. and L.-S. Fan. Quantitative analysis and computation of two-dimensional bubble columns. *AIChE J*, 42:301–318, 1996.

[19] R. Lindken and W. Merzkirch. A novel PIV technique for measurment in multiphase flows and its application to bubbly flows. *Experiments in Fluids*, 33:814–825, 2002.

[20] T. Moshammer, F. Mayr, K. Kargl, and C. Honeger. Simulation of oil flow in gear Box Housing. *SAE international*, 2006.

[21] M.Raffel, C. Willert, and J. Kompenhans. *Particle Image Velocimetry A practical Guide*. Springer, 1998.

[22] Pedersen N. *Experimental Investigation of Flow Structures in a Centrifugal Pump Impeller using Particle Image Velocimetry*. Technical University of Denmark, Lyngby, 2000.

[23] R.F. Lee D.J. Reese J., Mudde and L.-S. Fan. Analysis of multiphase systems through particle image velocimetry. *AIChE Symp*, 92:161–167, 1996.

[24] S. Sasic. Lecture notes form course in multiphase flows, 2010.

[25] M. Sommerfeld and D. Bröder. Planar shadow image velocimetry for the analysis of the hydrodynamics in bubbly flows. *Meas Sci Technol*, 18:2513–2528, 2007.

[26] Olle Törnblom. Introduction Course in Particle Image Velocimetry, 2004.

[27] J. Westerweel. Theoretical analysis of the measurement precision and reliability in piv. *roceedings of the Third International Workshop on PIV*, 16.

[28] J. Westerweel. *Digital Particle Image Velocimetry - Theory and Application*. PhD thesis, Delft University Press, 1993.

[29] Deltev L. Wulff. PIV Measurment in Pumps. Technical report, TU Braunschweig Institut für Strömungsmaschinen Langer Kamp 6 D-38106 Braunschweig GERMANY, 2006.

[30] G. Heng Yeoh and J. Tu. *Computational Techniques for multi-phase flow*. Elsevier Ltd., 2010.